Experimental studies of the D2 line of 87 Rb vapour at 1.5 Tesla

MARSHALL, VIRGINIA,ROSE

Experimental studies of the D_2 line of ^{87}Rb vapour at 1.5 Tesla

Virginia Marshall

Abstract

An investigation into the temperature evolution of transmission and absorption coefficient spectra of Rubidium atoms in the hyperfine Paschen-Back regime was successfully undertaken for a continuous laser detuning of approximately 150 GHz. All experiments were undertaken using a 1 mm long cell of isotopically enhanced ^{87}Rb. The magnet used had a peak field of 1.54 T. The forms of both the S_0 and S_1 Stokes Parameters showed excellent agreement with the theory from ElecSus at temperatures ranging from 56 °C to 160 °C, with the S_0 parameter also agreeing in narrow-band spectra of up to 20 GHz.

The absorption coefficient ratio of strong transitions, expected to be equal to 3.00, was measured to be within their uncertainty of this value when a possible temperature fluctuation of < 1 K was taken into account. Both the strong and weak transitions were measured and compared to the theory from ElecSus, which was found to successfully predict the behaviour of ^{87}Rb atoms in the hyperfine Paschen-Back regime. Areas of expansion and improvement of the ElecSus program were identified.

The power evolution of the D2 line of Rubidium was also investigated for a narrow beam of $w < 0.4$ mm in both no external magnetic field and the hyperfine Paschen-Back regime. The inhomogeneous shape of the power evolution was found to not fit the data, while the χ^2 analysis showed that the homogeneous shape was better.

The Weak Probe regime was found to be reached at values of I/I_{sat} up to 2 orders of magnitude higher than the 10^{-3} found previously. This provides possibilities for applications such that the SNR can be increased when measuring transmission or absorption coefficients. It is unclear whether the use of a magnetic field significantly changes the intensity required to reach the Weak Probe regime. This should be investigated using a wider beam, with a different experimental cell.

Experimental studies of the D_2 line of ^{87}Rb vapour at 1.5 Tesla

Virginia Marshall

A thesis submitted in partial fulfilment
of the requirements for the degree of
Master Of Science By Research

Department of Physics
Durham University

November 23, 2017

Contents

Declaration

I confirm that no part of the material offered has previously been submitted by myself for a degree in this or any other University. Where material has been generated through joint work, the work of others has been indicated.

Virginia Marshall
Durham, November 23, 2017

Chapter 1

Introduction

1.1 Motivation

1.1.1 Light-Matter Interactions

Light's far-ranging uses and applications mean it has previously been called 'the great unifier across science' [1]. From biology, where all life on earth is dependent on photosynthesis; to physics, where solar energy has been of interest since Bequerel discovered the photoelectric effect in 1839: [2] the potential of understanding the effect light has on matter is hard to overstate.

The laws which govern these interaction are called quantum electrodynamics. However, we only need a semi-classical approximation to understand most of the physics. To this day, our knowledge of these interactions forms the basis of many modern technologies. As recently as 2014, the Nobel prize in physics was awarded for the invention of the blue LED [3].

Atomic physics is a rich, practical field in which light-matter interactions can be studied. Applications within this community include laser cooling [4], optical waveguides [5] and atomic clocks [6], and potentially quantum computing [7].

During this thesis, we experimentally investigate a specific light-matter interaction: Rubidium vapour interacting with near-infrared laser light. The main focus is the Zeeman Effect, which describes the splitting of atomic energy states under the influence of an external magnetic field. Specifically,

this effect at very high magnetic fields, known as the hyperfine Paschen-Back regime.

1.1.2 Quantum Computing

Quantum computing, first envisioned by Feynman in 1982 [8], may be the best answer to the question of simulating quantum physics. As Feynamn said in his original 1982 article and speech, "let the computer itself by built of quantum mechanical elements which obey quantum mechanical laws". Quantum bits, or qubits, can be in $|0\rangle$, $|1\rangle$ and a linear superposition of the two, unlike the binary 0,1 system used in classic computing [9].

Atomic and optical systems are a strong contender for qubits, as they offer some unique advantages [7]: the foundations of quantum mechanics in these systems have been extensively studied in the lab. The success of atom- and ion-based atomic clocks as quantum coherent devices help provide motivation for the use of atom and ion based quantum computers.

For approximately 20 years, atoms have been of particular interest [10] as atoms couple weakly to the environment they are in, whereas ions interact strongly with their environment, which leads to 'decoherence' channels from technical noise sources. Moreover, atoms have a very short interaction range so large ensembles of atoms can be used without perturbing each other, which is the main advantage of atoms over ions.

1.1.3 Alkali Metals

Alkali metals are in Group I of the periodic table. Although hydrogen is not technically an alkali metal, its structure is similar due to its single valence electron.

This simple structure, amongst other things, means that it is much easier to calculate state wavefunctions and energy levels of the atom, and hence the atom-light interactions. This valence electron can be pumped by a laser into an excited state, and then decay back into the ground state. The absorption of light by the atom can be observed with the use of a photodiode, and so this atomic system allows a quantative understanding of light-matter interactions.

Specifically, alkali metal atoms would be of particular use in quantum computers, as [7] their nuclear spin leads to hyperfine splitting in the ground state, which have a long lifetime, and are potentially ideal qubits.

1.1.4 Ultra-Cold Atoms versus Thermal Vapours

First concepted in 1975 [11], laser cooling has driven a revolution in the research of atomic physics. Work done in the experimental realisation of the technique won the 1997 Nobel Prize [4, 12, 13]. In 1985, Chu [14] developed a technique for cooling atoms below the Doppler limit. Since then, much of atomic physics research has been dominated by ultra-cold alkali metals, for example work in Bose-Einstein condensates won the 2001 Nobel Prize in Physics [15, 16]

These systems generally have intricate setups, including Magneto-Optical Traps (MOTs) [17], complex laser locking systems [18], and vacuum chambers [19]. Therefore, although useful to study, the use of ultra-cold atoms in a quantum computer seems challenging. Simplifying the setup may therefore be cheaper, more scalable and be easier to setup as multiple years of experience of laser locking, vacuum chambers and MOTs would not be required. For example, it has been shown that arrays of microscopic thermal vapor cells of alkali atoms can be used as a 'scalable single-photon source' [20]. This means that by using thermal vapours instead of ultra-cold atoms, another route for a quantum computer can be established.

Thermal vapours also have a huge advantage that cold atoms do not: the ability to change the vapour pressure over a logarithmic scale by changing the temperature, and therefore the ability to fine-tune the number density, which the strength of the atom-light interaction depends on. As can be seen in Figure 1.1, the vapour pressure (in atmospheres, atm) of ^{87}Rb depends on the temperature of the vapour (in Kelvin, K) by the equation

$$\log_{10} P_v = \begin{cases} 4.857 - \frac{4215}{T}, & T < T_m, \\ 4.312 - \frac{4040}{T}, & T > T_m, \end{cases} \tag{1.1}$$

where T is temperature (in Kelvin, K), T_m is the melting point $T_m = 312.45$ K $= 39.30$ °C). The ability to fine-tune the strength of the atom-light interaction is extremely useful because that means that the complex

electric susceptibility, χ_e, can be fine-tuned, where the real part, χ_{re}, gives the refractive index of the medium, and the imaginary part, χ_{imag}, gives the absorption of light by the medium. This makes thermal vapours an excellent choice to study as these can be quantitatively measured in the lab.

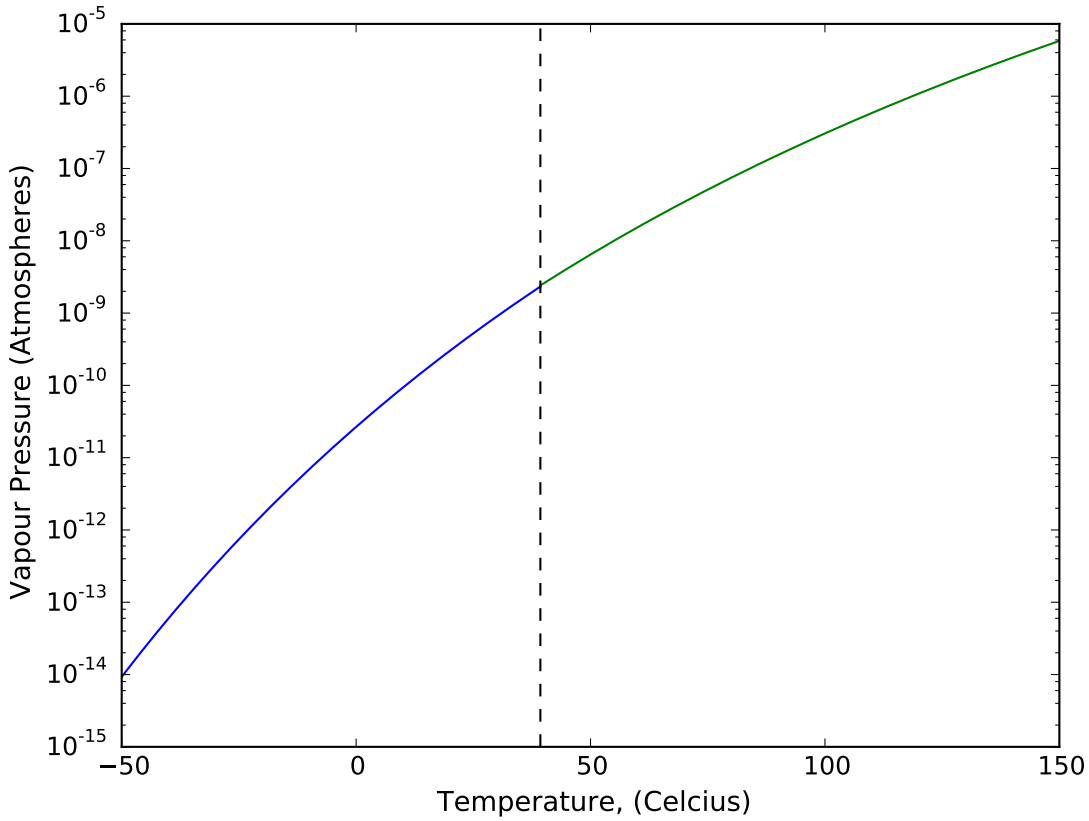

Figure 1.1: Vapour Pressure of ^{87}Rb as a function of temperature in °C, as given by the equations in 1.1. The dashed line shows the melting point, where the green line is the liquid phase ($T > T_m$), and the blue line is the solid phase ($T < T_m$). This model is estimated to have an accuracy of ±5% from 24.85 °C to 276.85 °C [21].

1.1.5 High Magnetic Fields

When a magnetic field is applied to an alkali metal atom, the degeneracy within the ground state of that atom breaks down as the energy levels split apart from one another (the Zeeman Effect [22]). The excited states also

experience splitting, so the optical transition has changed. The optical transition between ground and excited state is what is studied in this thesis. The bulk of the theory behind this effect is discussed in Chapter 2.

Spectroscopy on the alkali metal atom ^{87}Rb, the focus of this thesis, has been undertaken at various magnetic fields. The magnetic fields previously used in conjunction with spectroscopy of alkali metal atoms are rarely in the hyperfine Paschen-Back regime [23–25].

To the best of our knowledge, the strongest magnetic field experimentally studied and compared to theory for ^{87}Rb is $B = 0.6$ T. In this thesis, the magnetic field is more than double 0.6 T, at 1.54 T.

1.2 Recent Work In Area

At Durham University, an extensive theory for the weak-probe spectroscopy of alkali-metals atoms has been published [26]. The program calculates the 'Electric Susceptibilty' χ_e, and is appropriately named 'ElecSus'. It includes the effects of magnetic field, temperature, polarisation of input light, self broadening and additional broadening from buffer gases for the alkali metals. It gives absolute values with real units which can be compared the laboratory measurements for values such as the 'S_0' absorption spectra from χ_{re}, and 'S_1' faraday spectra from χ_{imag}, where 'S_0' and 'S_1' refer to Stokes parameters [27].

'ElecSus' is motivated by not only potential for future technology in quantum computing, but also in more short-term applications. For example, the calculations of Faraday rotation have allowed an optical isolator [24] to be built; a Faraday filter with a noise bandwidth of less than 1 GHz [28] to be created; and a new type of laser [29].These are just some of the possible applications directly using the knowledge gained from the 'ElecSus' program [27].

So far, the 'ElecSus' has been used and tested for (1) ^{87}Rb and ^{85}Rb [30, 31]; (2) other alkali metals such as Cesium and Potassium [32–34]; (3) no magnetic field [26, 35]; (4) up to $B = 0.6$ T [23–26]; (5) at various temperatures [26, 36]; (6) differing cell sizes [34, 35]; and has been shown to have excellent agreement with all experimental data.

1.3 Investigation Themes of this Thesis

One regime in which the accuracy of the 'ElecSus' program has not been tested, however, is for high magnetic fields that are further into the hyperfine Paschen-Back regime than 0.6 T. This regime has previously been studied for other alkali metals, such as Sodium in 1988 with a magnetic field of up to 0.028 T [37], and subsequently Sodium and Lithium in 1992 at magnetic fields of up to 1 T [38]. Although the frequency at which the absorption occurred was compared to theoretical values, no comparison for absorption was undertaken. This is because the spectra were taken via fluorescence measurements and as such have no absolute absorption measurements, and have only arbitrary units.

The 'ElecSus' program works by calculating either the D1 or D2 line, but at high magnetic fields the splitting of the energy levels means that these can start to mix. One of the aims of this thesis is to continue this investigation by determining whether the theory behind the 'ElecSus' program accurately predicts the electric susceptibility, transition strengths and transition frequency at magnetic fields of up to 1.54 T, which hasn't been investigated previously.

This thesis has two primary foci. Firstly, an undertaking of an investigation into the evolution of Rubidium spectroscopy at 1.54 T. Specifically, the evolution of χ_{re} and χ_{imag} as a function of temperature and input-light polarisation. As this is measured with absolute values, rather than arbitrary units, it is possible to directly compare to the theory from 'ElecSus' with residuals.

Secondly, an investigation into the power evolution of Rubidium spectroscopy at 1.54 T is undertaken: specifically whether the power at which one can be sure to be in the weak probe regime changes in the hyperfine Paschen-Back regime [39]. The effect of laser beam widths will also be discussed.

1.4 Thesis structure

This thesis is structured as follows:

- Theory: in which the relevent quantum numbers are defined; the Hamiltonian along with the fine and hyperfine structure of ^{87}Rb is discussed along with the degeneracy of energy states; the coupled and un-coupled basis is explored; the different regimes that the magnitude of magnetic field causes are explained; and the different possible transitions that can be driven are outlined. Different types of lineshapes are their physical origins are discussed and the theory behind the weak probe regime including hyperfine pumping and dark states is explained. The chapter ends with a discussion of the theoretical effect of temperature on the different Stokes Parameters.

- Temperature Evolution: in which the temperature evolution of different Stokes Parameters for ^{87}Rb under the influence of a 1.54 T magnet is investigated. The experimental setup is described and the steps taken to convert raw time domain data into a frequency spectrum are outlined briefly. This is undertaken using two different lasers which allow both wide and narrow frequency detunings to be investigated. The 'strong' and 'weak' transitions are observed separately and the results are compared to the theoretical spectra that the ElecSus program provides.

- Power Evolution: in which the limits of the weak probe regime are discussed and experimentally investigated for a laser beam with a much smaller beam width than has been used in previous work, for ^{87}Rb atoms both with and without the high external magnetic field. The power evolution for different transitions are also compared.

- Conclusion: a brief summary of the investigations into temperature evolution and power evolution for the ^{87}Rb atoms during the course of this thesis is described, and an outlook for the future scientific possibilities that can be achieved with the help of the work undertaken in this thesis.

Chapter 2

Theory

In this chapter, the theory behind light-matter interactions is discussed. The effect that different magnetic field strengths have on atom-light interactions, and the electric susceptibility will be discussed, along with predictions for the temperature dependence of transmission spectra and other Stokes parameters.

2.1 Quantum Numbers and Magnetic Moment

The classical model of the atom has an electron with negative charge orbiting a positively charged nucleus, where the loop of the orbit induces a magnetic moment. In this section, we discuss the quantum mechanics of magnetic moments.

2.1.1 Bohr's Atomic Model

The principal quantum number, n, is used to define the quantised energy level E_n that is occupied by the electron [40, 41]. It has possible values of integers of 1 or above, i.e.: $n = 1, 2, 3...$, where, for hydrogen and helium atoms, $n = 1$ is the ground state and subsequent integers denote the higher energy levels.

The quantum number that defines the orbital angular momentum of the electron, l, is found from the magnitude of the vector $\boldsymbol{l}$. This quantum number can range from $l = 0,\ 1,\ ...,\ (n-2),\ (n-1)$. The values of l are also given by letters: $l = 0 \rightarrow s$, $l = 1 \rightarrow p$, $l = 2 \rightarrow d$, $l = 3 \rightarrow f$, $l = 4 \rightarrow g$, and so on. These letters refer to the 's', 'p', 'd', etc orbitals of the electron. The quantum number l relates to the total orbital angular momentum, L via the equation

$$L^2 = \hbar^2 l(l+1), \tag{2.1}$$

where $\hbar$ is Planck's constant h divided by 2π. The spatial orientation of l is specified by m_l, the corresponding magnetic quantum number, with $2l+1$ possibilities of m_l for each l, assigned by: $m_l = -l, (-l+1), ..., (l-1), l$.

2.1.2 Electron Spin

Like charge and mass, one of the fundamental properties of all particles is spin. All particles have a defined spin of vector $\mathbf{s}$, and the electron is no different. Each individual electron's spin has magnitude $s = \frac{1}{2}$.

As the atoms used in this thesis are alkali metals (group I of the periodic table), so there is one valence electron and therefore the total electron spin is given by $S = \sum_i s_i = \frac{1}{2}$. The direction of the spin is assigned from a secondary or magnetic quantum number m_s, and the possibilities are in this case are $m_s = -\frac{1}{2}, \frac{1}{2}$ [42].

The total electronic angular momentum vector $\boldsymbol{J}$ is defined as the sum of the vectors $\boldsymbol{l}$ and $\boldsymbol{s}$, where the magnitude of $\boldsymbol{J}$ is denoted by J. When $\boldsymbol{l}$, and $\boldsymbol{s}$ couple to one another, using J to label different quantum states is useful. Values of J range from $|L-S|$, to $|L+S|$. There exists a magnetic quantum number m_J, which defines the direction of the vector. m_J has a range of $2J+1$, and takes the values $m_J = -J, (-J+1), ..., (J-1), J$.

The electron's magnetic moment $\boldsymbol{\mu_J}$ also combines the contributions from the orbital and spin contributions, [43] as

$$\boldsymbol{\mu_J} = -g_L \mu_B \boldsymbol{L} - g_s \mu_B \boldsymbol{S}, \tag{2.2}$$

where g_s is the g-factor, or dimensionless magnetic moment, of the electron

spin ($g_s = 2.00231930436153(53)$ [44]), g_L is the corresponding g-factor of L ($g_L = 1$ [44]) and μ_B is the Bohr magneton.

2.1.3 Nuclear Spin

The nucleus also has its own spin $\boldsymbol{I}$, and its own magnetic moment given by

$$\boldsymbol{\mu_I} = g_I \mu_N \boldsymbol{I} = g'_I \mu_B \boldsymbol{I}, \tag{2.3}$$

where g'_I ($= -0.0009951414(10)$ [45] for ^{87}Rb) is the corresponding g-factor, which is several orders of magnitude less than g_s or g_L. μ_N is the nuclear magneton, which is related to the Bohr magneton via the electron-proton mass ratio [40], i.e.:

$$\mu_N = \mu_\mathrm{B} \frac{m_e}{M_p} \simeq \frac{\mu_\mathrm{B}}{1836}. \tag{2.4}$$

When the nuclear spin I couples with J, the total atomic angular momentum quantum number F becomes a more useful quantum number to define the states than J. $\boldsymbol{F}$ is the sum of the vectors $\boldsymbol{I}$ and $\boldsymbol{J}$, with magnitude F, and a corresponding magnetic quantum number, $m_F = |J - I|,...,|J + I|$. The total magnetic moment of the atom is therefore

$$\boldsymbol{\mu} = \boldsymbol{\mu_J} + \boldsymbol{\mu_I} = -\mu_\mathrm{B}(g_L \boldsymbol{L} + g_s \boldsymbol{S} + g'_I \boldsymbol{I}), \tag{2.5}$$

which is dominated by the electron magnetic moment, and is often taken to be $\boldsymbol{\mu} = \boldsymbol{\mu_J}$.

2.2 Hamiltonian of the Atom

The energy states of the atom are described by the eigenvalues of the atomic Hamiltonian $\hat{H}$, given by

$$\hat{H} = \hat{H}_0 + \hat{H}_\mathrm{fs} + \hat{H}_\mathrm{hfs} + \hat{H}_\mathrm{Z}, \tag{2.6}$$

where $\hat{H}_0$ is the the simplest atomic structure given by the quantum number n, $\hat{H}_\mathrm{fs}$ refers to the fine structure, $\hat{H}_\mathrm{hfs}$ to the hyperfine structure, and $\hat{H}_Z$ gives the interaction between the atom and an external magnetic field. In the absence of an external magnetic field, the expectation of each respective operator $\hat{H}_0 \gg \hat{H}_\mathrm{fs} \gg \hat{H}_\mathrm{hfs}$, and the expectation value of the operator $\hat{H}_\mathrm{Z} = 0$ [46].

2.2.1 Fine Structure

First named by Sommerfeld [47] to explain the hydrogen spectrum, fine structure in energy levels arises when there are multiple possible values of J for a single l value. The spin-orbit term in the fine structure Hamiltonian is given by (equation 8.102 in [48])

$$\hat{H}_{\text{fs}} = \frac{\gamma_{\text{fs}}}{\hbar^2}\hat{L}\cdot\hat{S}, \tag{2.7}$$

where γ_{fs} is the spin-orbit constant [40]:

$$\gamma_{\text{fs}} = \frac{\hbar^2}{2{m_e}^2c^2}\frac{e^2}{4\pi\epsilon_0}\frac{1}{(na_0)^3 l(l+\frac{1}{2})(l+1)}. \tag{2.8}$$

The eigenenergy E_{fs} from the expectation value of $\hat{H}_{\text{fs}}$ is

$$E_{\text{fs}} = \frac{\gamma_{\text{fs}}}{2}\Big[J(J+1) - L(L+1) - S(S+1)\Big], \tag{2.9}$$

and therefore if J has multiple possible values, there will be corresponding values of E_{fs} for each J.

For the atom of interest, ^{87}Rb, there is one valence electron and therefore $S = \frac{1}{2}$. For the ground state, (for ^{87}Rb, $n = 5$) $L = 0$ therefore the possible values of J are $J = |0 - \frac{1}{2}|, ..., |0 + \frac{1}{2}| = \frac{1}{2}$. There is only one possible value of J in the ground state, and therefore only one possible E_{fs} value, and so for the ground state there is no fine structure. This one ground state is defined in $n\ ^{2S+1}L_J$ form as $5\ ^2S_{\frac{1}{2}}$.

In the first excited state, the principal quantum number is still $n = 5$, and the angular momentum of the electron $L = 1$. Therefore the possible values of J range from $J = |1 - \frac{1}{2}|, ..., |1 + \frac{1}{2}|$, and hence there are 2 possible values of J: $\frac{1}{2}$ and $\frac{3}{2}$. These two possibilities for the excited state can be defined, in $n\ ^{2S+1}L_J$ form, as $5\ ^2P_{\frac{1}{2}}$ and $5\ ^2P_{\frac{3}{2}}$.

We define the two possible transitions from the ground state to either the $J = \frac{1}{2}$ or $J = \frac{3}{2}$ state as the 'D1' and 'D2' transitions respectively, which are split by approximately 7.1 THz for ^{87}Rb in the absence of an external magnetic field. This thesis looks only at the D2 transition $\left(^2S_{\frac{1}{2}} \rightarrow {}^2P_{\frac{3}{2}}\right)$, shown in figure 2.3.

On the left of diagram 2.1, the L and S are coupled to each other, making J a good quantum number. The magnitude of $\boldsymbol{J}$ is a fixed value in the

absence of external torque [40]. In the coupled basis, the magnitudes of $\boldsymbol{L}$ and $\boldsymbol{S}$ remain constant while their directions change due to the spin-orbit interaction, and hence the vectors precess about $\boldsymbol{J}$, while J precesses around the magnetic field axis as shown in the diagram.

On the right of the diagram, the uncoupled basis in which $\underline{\boldsymbol{L}}$ and $\underline{\boldsymbol{S}}$ independently precess around the magnetic field axis, rather than around $\underline{\boldsymbol{J}}$. In this case, L and S must be taken as separate quantum numbers, as J no longer can be called a good quantum number. This regime is entered when L, S interact more strongly with the external magnetic field than with each other.

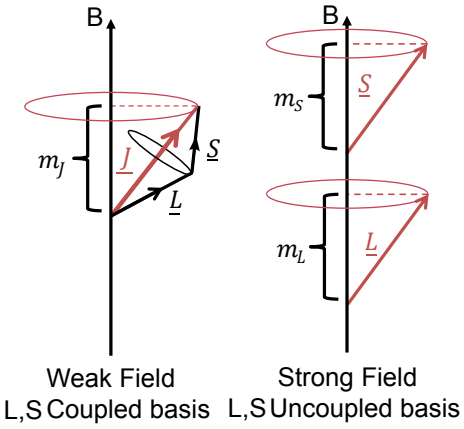

Figure 2.1: Left: Diagram vectorally showing the L, S coupled basis, for which $\underline{\boldsymbol{L}}$ and $\underline{\boldsymbol{S}}$ couple to one another and precess around J, while J precesses around the B axis, which refers to the external magnetic field. $\underline{\boldsymbol{J}}$ can be called a good quantum number as its projection does not evolve in time, unlike the projections of $\underline{\boldsymbol{L}}$ and $\underline{\boldsymbol{S}}$, and m_J is also a good quantum number.
Right: Diagram vectorally showing the L, S uncoupled basis, with $\underline{\boldsymbol{L}}$ and $\underline{\boldsymbol{S}}$ separately defined and each precessing individually about the $\boldsymbol{B}$ axis. $\underline{\boldsymbol{J}}$ is no longer a good quantum number, and instead m_L and m_S can be taken as good quantum numbers.

2.2.2 Hyperfine Structure

There also exists a much smaller effect which has been appropriately named 'hyperfine' structure, that arises from the multiple possible values of F. The effect includes the magnetic dipole interaction $\hat{H}_{\mathrm{d}}$, and the electric quadrupole interaction $\hat{H}_{\mathrm{q}}$ as

$$\hat{H}_{\mathrm{hfs}} = \hat{H}_{\mathrm{d}} + \hat{H}_{\mathrm{q}}. \tag{2.10}$$

The magnetic dipole term arises from the interaction of the nuclear dipole moment μ_I and the magnetic field produced from the orbit of the electrons B_e and is given by [49]

$$\hat{H}_{\mathrm{d}} = -\mu_I \cdot B_e = \frac{A_{\mathrm{hfs}}}{\hbar^2}\hat{I}\cdot\hat{J}, \tag{2.11}$$

where A_{hfs} is the magnetic dipole constant for each particular state. The electric quadrupole term is given by the equation [49]

$$\hat{H}_{\mathrm{q}} = \frac{B_{\mathrm{hfs}}}{2\hat{I}(2\hat{I}-1)\hat{J}(2\hat{J}-1)\hbar^2}\left[3\left(\hat{I}\cdot\hat{J}\right)^2 + \frac{3}{2}\left(\hat{I}\cdot\hat{J}\right) - \hat{I}\left(\hat{I}+1\right)\hat{J}\left(\hat{J}+1\right)\right], \tag{2.12}$$

where B_{hfs} is the electric quadrupole constant of the state. $\hat{H}_{\mathrm{q}}$ is zero for $I = 0$, or $\frac{1}{2}$ and for $J = 0$ or $\frac{1}{2}$.

The eigenenergies of the hyperfine interaction occur relative to the zero-detuning energy, ΔE_{hfs}, is given as the combination of the magnetic dipole interaction and the electric quadrupole interaction:

$$\Delta E_{\mathrm{hfs}} = \frac{A_{\mathrm{hfs}}}{2}K + \frac{B_{\mathrm{hfs}}}{4}\frac{\frac{3}{2}K(K+1) - 2I(I+1)J(J+1)}{I(2I-1)J(2J-1)}, \tag{2.13}$$

where K is given by (equation 9.60 in [50])

$$K = F(F+1) - I(I+1) - J(J+1), \tag{2.14}$$

hence multiple values of F or J, E_{hfs} lead to hyperfine multiple energy levels. These levels are split by the difference in their respective E_{hfs}, and each have a degeneracy of $2F+1$ in the absence of a magnetic field, defined by their respective m_F numbers, ranging from $-F$, $(-F+1)$, ..., $(F-1)$, F.

In figure 2.2, a similar diagram to figure 2.1 is shown, except for the I, J coupled basis. Here, it is $\boldsymbol{F}$ that precesses around the magnetic field axis,

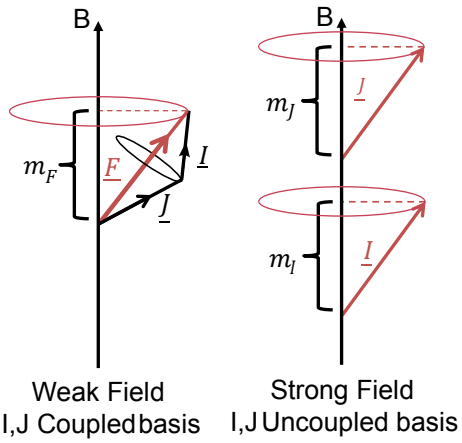

Figure 2.2: Left: Diagram vectorally showing the I, J coupled basis, for which $\underline{\boldsymbol{I}}$ and $\underline{\boldsymbol{J}}$ couple to one another and precess around F, while F precesses around the B axis, which refers to the external magnetic field. $\underline{\boldsymbol{F}}$ can be called a good quantum number as it encompasses the directions and magnitudes of both $\underline{\boldsymbol{L}}$ and $\underline{\boldsymbol{I}}$, and m_F is also a good quantum number.
Right: Diagram vectorally showing the I, J uncoupled basis, with $\underline{\boldsymbol{I}}$ and $\underline{\boldsymbol{J}}$ separately defined and each precessing individually about the $\boldsymbol{B}$ axis. $\underline{\boldsymbol{F}}$ is no longer a good quantum number, where m_J and m_I are good quantum numbers.

and while the magnitudes of $\boldsymbol{I}$ and $\boldsymbol{J}$ remain constant, it is their directions that change and precess about $\boldsymbol{F}$.

The nuclear spin for ^{87}Rb is $I = \frac{3}{2}$. Therefore, for the ground state in which $J = \frac{1}{2}$, the possible values of F are $|\frac{1}{2} - \frac{3}{2}| = 1$, to $|\frac{1}{2} + \frac{3}{2}| = 2$. This leads to a hyperfine structure of 2 separate energy levels within the ground state.

These states can be seen in the bottom half of figure 2.3, with a splitting of 6.83 GHz in the absence of an external magnetic field. The $F = 1$ level has 3 degenerate states: $m_F = -1, 0, +1$, and the $F = 2$ level has 5 degenerate states $m_F = -2, -1, 0, +1, +2$.

The excited state for the D2 transition has $J = \frac{3}{2}$, and so the F values range from $|\frac{3}{2} - \frac{3}{2}| = 0$, to $|\frac{3}{2} + \frac{3}{2}| = 3$, which can be seen at the top half of the figure 2.3. These states have a splitting from $F = 0$ to $F = 3$ of 495.81 MHz, which is an order of magnitude less than that of the ground state.

For $B = 0$, the degeneracy for each of these F states occurs as follows:

$$\begin{aligned} F &= 0, m_F = 0, \\ F &= 1, m_F = -1, 0, +1, \\ F &= 2, m_F = -2, -1, 0, +1, +2, \\ F &= 3, m_F = -3, -2, -1, 0, +1, +2, +3, \end{aligned} \tag{2.15}$$

and these states are all shown in figure 2.3.

2.2.3 The Zeeman Effect

The degeneracy of $2F + 1$ per F state breaks down when an external magnetic field is applied, as $\hat{H}_{\mathrm{Z}}$ is no longer zero. The expectation value of the Hamiltonian is changed depending on the F, m_F values of that state, and therefore the energy levels start to split apart.

For a particular energy state, the magnetic field has an interaction with the atom called the Zeeman effect, given by

$$\hat{H}_{\mathrm{Z}} = -\boldsymbol{\mu} \cdot \mathbf{B}, \tag{2.16}$$

where $\boldsymbol{\mu}$ is given by equation 2.5, and $\mathbf{B}$ refers to the external magnetic field applied to the atom.

2.3 Magnetic Field Regimes

Magnetic fields have the effect on the atomic Hamiltonian described by 2.6. However, the extent of this effect is dependent on the magnitude of $\underline{\boldsymbol{B}}$. In this section, the different regimes that the magnitude of magnetic field causes will be discussed.

2.3.1 Weak field

When the respective expectation values of $\hat{H}_{\mathrm{fs}} \gg \hat{H}_{\mathrm{hfs}} \gg \hat{H}_{\mathrm{Z}}$, $\hat{H}_{\mathrm{Z}}$ acts only as a perturbation to the rest of the Hamiltonian. The vectors $\underline{\boldsymbol{I}}$, $\underline{\boldsymbol{J}}$ couple to one another as in shown in figure 2.2 and so the quantum numbers F and

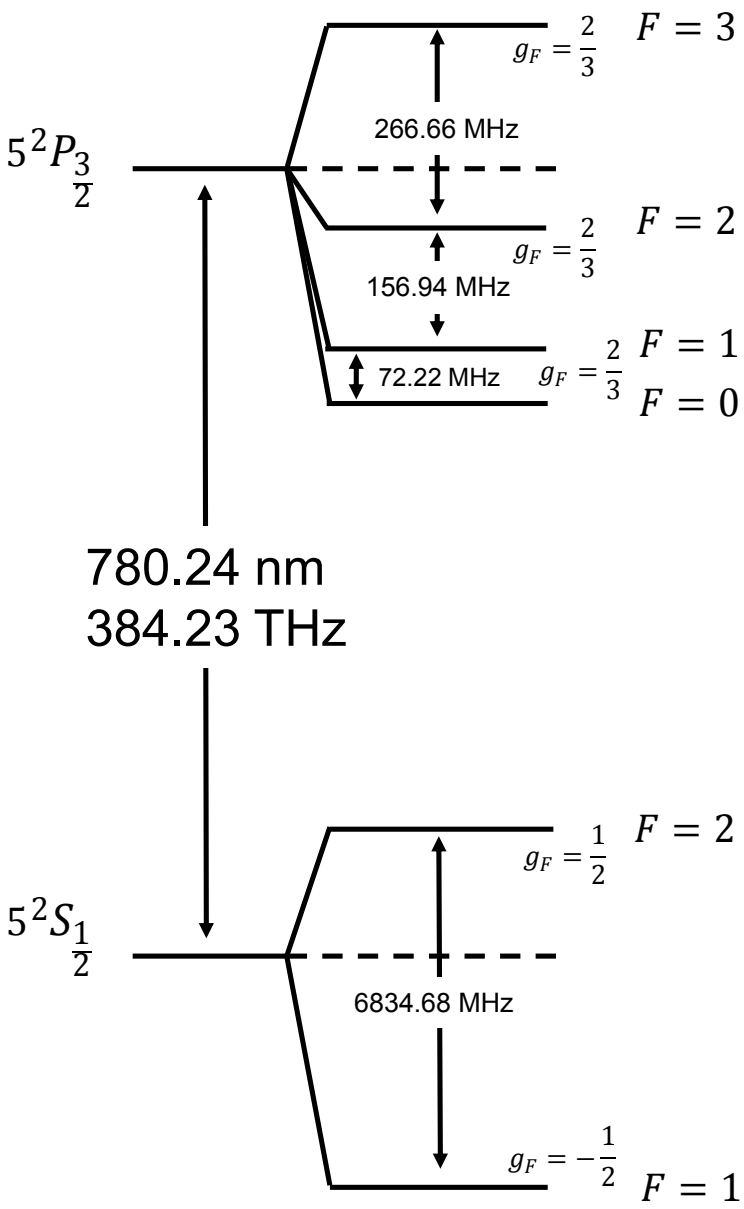

Figure 2.3: Diagram showing the fine and hyperfine structure of the D2 transition of the ^{87}Rubidium atom, at a magnetic field of $B = 0$ T. The degeneracy of each individual F state is discussed in section 2.2.2, and is equal to $2F + 1$. The m_F degenerate states are not shown. All energy splittings calculated by ElecSsus and taken from [46].

m_F are called 'good quantum numbers' in that they describe the grouping of the energy states. Furthermore, the magnetic field component of the Hamiltonian, $\hat{H}_Z$, given by 2.16, is dominated by the electron's magnetic moment and can therefore be reduced to

$$\hat{H}_Z = \frac{\mu_\mathrm{B}}{\hbar}(g_L \boldsymbol{L} + g_s \boldsymbol{S}) \cdot \boldsymbol{B}, \tag{2.17}$$

as the nuclear magnetic moment is much smaller than both the electron's magnetic moment and any other part of the Hamiltonian. The shift in energy level has a linear relationship to magnetic field in this region. This is known as the Hyperfine Linear Zeeman regime (HLZ) [23]. The inset graph shown in figure 2.4 shows the linear energy shifts of the $F = 2$ energy levels in the HLZ regime, given by

$$E = m_F g_F \mu_\mathrm{B} B \tag{2.18}$$

where the g_F values are also shown in figure 2.3, and are given by

$$\begin{aligned} g_F = g_J \frac{F(F+1) - I(I+1) + J(J+1)}{2F(F+1)} \\ + g_I \frac{F(F+1) + I(I+1) - J(J+1)}{2F(F+1)}, \end{aligned} \tag{2.19}$$

which because $g_J \gg g_I$, can be reduced to just the first term.

2.3.2 Intermediate and Strong Field

As the expectation value of $\hat{H}_Z$ starts to become closer in value to the expectation value of $\hat{H}_\mathrm{hfs}$, the relationship between the shift and the magnetic field is no longer linear, and the lines begin to curve. This regime is called 'intermediate', as neither the Zeeman effect nor the hyperfine part of the Hamiltonian dominates.

When the respective expectation values of $\hat{H}_\mathrm{Z} \gg \hat{H}_\mathrm{hfs}$, the nuclear portion of the magnet moment can no longer be ignored, and must be included in calculations of magnetic moment. In this regime, $\underline{\boldsymbol{I}}$, and $\underline{\boldsymbol{J}}$ are no longer coupled to one another, as shown in the right of diagram 2.2. This means that F and m_F are no longer 'good quantum numbers', and instead we use the total angular momentum J, m_J and nuclear spin I, m_I quantum numbers to

describe the grouping of energy states. This is called the hyperfine Paschen-Back regime (HPB).

In figure 2.4, a Breit-Rabi diagram of the $5^2S_{\frac{1}{2}}$ ground state of ^{87}Rb is shown up to a magnetic field of 1.54 T. The figure shows the weak (inset), intermediate (< 0.3 T) and hyperfine Paschen-Back (> 0.4 T) regimes. In the main graph, the intermediate regime can be seen in the curvature of the lines, where the respective expectation values of $\hat{H}_{\mathrm{Z}}$ and $\hat{H}_{\mathrm{hfs}}$ are similar in size and neither dominates. The weak field HLZ regime is shown in the inset, with an external magnetic field of < 1 mT.

When the lines become linear again, this can be called the hyperfine Paschen-Back regime, as at this point the respective expectation values of $\hat{H}_{\mathrm{Z}} \gg \hat{H}_{\mathrm{hfs}}$. It is clear that the states are now grouped by their J, m_J values. This is especially clear for the $F = 2$, $m_F = -2$ state, which starts degenerate with the other $F = 2$ energy states and, as magnetic field is increased, joins the $m_J = -\frac{1}{2}$ whereas the other $F = 2$ states keep in their $m_J = +\frac{1}{2}$ grouping and are ordered by their m_I values ranging between $m_I = +\frac{3}{2}$ and $m_I = -\frac{3}{2}$.

In figure 2.5, the energy level splittings of the $5^2P_{\frac{3}{2}}$ state is shown. The states cross each other as they rearrange into an order defined not by their F number, but by their m_J value. In each group of four, the states are ordered by their m_I which is between $+\frac{3}{2}$ and $-\frac{3}{2}$.

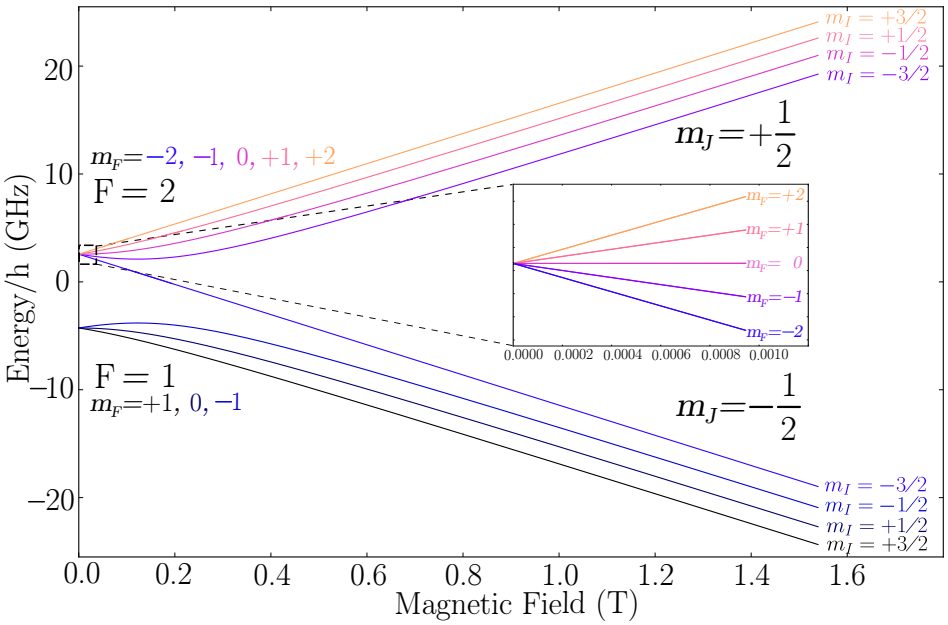

Figure 2.4: Breit Rabi Diagram showing 5 $^2S_{\frac{1}{2}}$ up to 1.54 T. The intermediate regime can be observed up to 0.3 T, and above 0.4 T the system is within the hyperfine Paschen-Back regime. The HLZ regime can be seen in the inset, at a much smaller magnetic field of < 0.01 T.

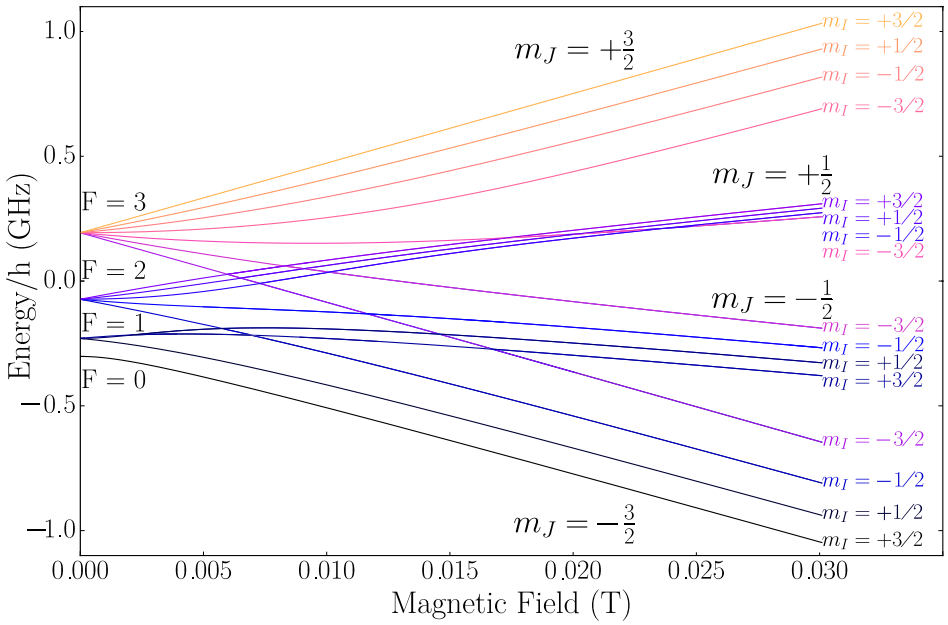

Figure 2.5: Diagram showing the energy level splitting up to $B = 0.03$ T of the 5 $^2P_{\frac{3}{2}}$ state in both the intermediate and the HPB regimes.

2.3.3 Strong field Limit

As the magnetic field increases even further (e.g.: > 200 T), the expectation value of $\hat{H}_{\mathrm{Z}}$ becomes not only much larger than the expectation value of $\hat{H}_{\mathrm{hfs}}$ but also comparable to that of $\hat{H}_{\mathrm{fs}}$, and the D2 energy level splittings cross the D1 energy levels. In figure 2.6 there are crossings from approximately $B = 200 - 400$ T. At this regime, the respective expectation values of neither $\hat{H}_{\mathrm{fs}}$ nor $\hat{H}_{\mathrm{Z}}$ dominates, and it can be called a secondary intermediate regime.

For the regime in which the respective expectation values of $\hat{H}_{\mathrm{Z}} \gg \hat{H}_{\mathrm{fs}}$, $\underline{\boldsymbol{L}}$ and $\underline{\boldsymbol{S}}$ uncouple from each other as shown in figure 2.1, and J can no longer be called a good quantum number. Therefore in this regime I, L and S all precess independently, and we define the state using the separate quantum numbers. This regime is known as the 'Paschen Back' regime.

For the atom of interest ^{87}Rb, the fields required for all the energy levels to have a linear relationship with the magnetic field again are approximately 600 T, as can be seen on figure 2.6. In this experiment it is very clear that while 1.54 T magnets are being used, the Paschen-Back regime is still far enough away that the D1 transition can confidently be ignored in our theory.

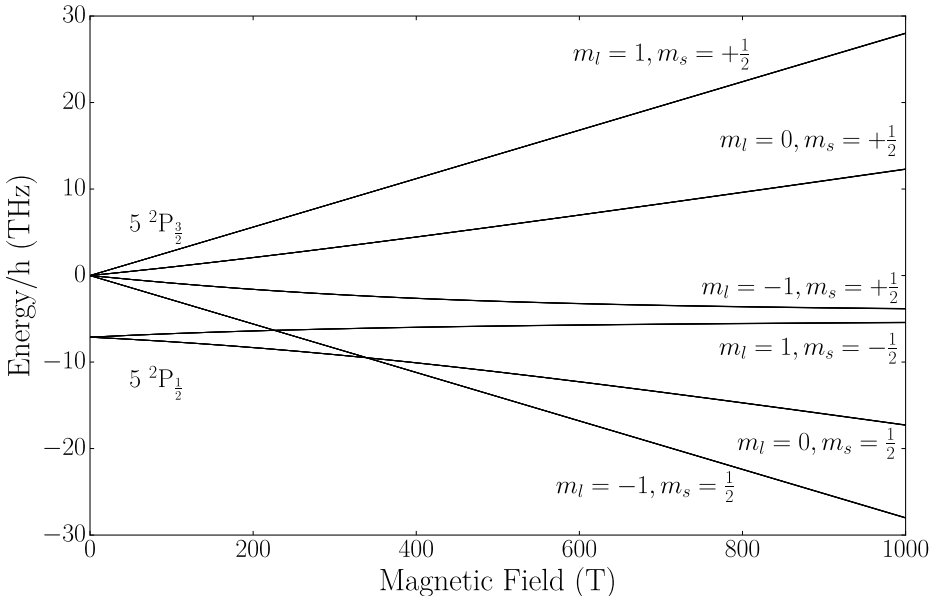

Figure 2.6: Energy levels where L=1, showing both the $5^2P_{\frac{1}{2}}$ and the $5^2P_{\frac{3}{2}}$ states in the Paschen-Back regime.

2.4 Driving Transitions

The polarisation of light is one factor that influences which transitions between different energy states are driven. In this section, two types of transition will be discussed: specifically π and σ.

2.4.1 Decomposition of Light

The classical light field $\hat{\mathcal{E}}$ of a plane wave can be written in terms of its spherical components, or Cartesian components [51]. For atom-light interactions, it is useful to use $\hat{z}$ and a combination of the $\hat{x}$ and $\hat{y}$ axes for the electric field of the light.

2.4.2 Transition Strength

For particular transition from an S to a P state, the orbital angular momentum quantum number must have $\Delta L = +1$, and therefore $\Delta m_L = 0,\pm 1$ depending on the polarisation of light. However, the projections of the nuclear and electronic spin remain unchanged. This leads to three different types of matrix elements:

1. $\langle m_L, m_S, m_I | \, C_L \, | m_{L'} = m_L + 1, m_s, m_I \rangle$ for LHCP light which drives a $\Delta m_L = +1$ transition,

2. $\langle m_L, m_S, m_I | \, C_R \, | m_{L'} = m_L - 1, m_s, m_I \rangle$ for RHCP light which drives a $\Delta m_L = -1$ transition,

3. $\langle m_L, m_S, m_I | \, C_0 \, | m_{L'} = m_L, m_s, m_I \rangle$ for linearly polarised light which drives a $\Delta m_L = 0$ transition,

where $C_{L,R,0}$ refers to the dipole operators of the LHCP, RHCP, and linearly polarised light respectively. Squaring each of these coefficients gives the transition strength of that transition, while for $F \rightarrow F'$ transitions which include degenerate states each possible $m_F \rightarrow m_{F'}$ transition must be summed to give the total transition strength.

2.4.3 π Transitions

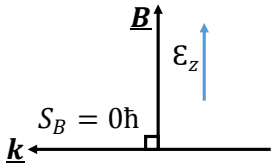

Figure 2.7: Vector diagram of the external magnetic field axis $\underline{\boldsymbol{B}}$ along z, showing a perpendicular axis for the propagation of light, $\underline{\boldsymbol{k}}$, along the x-axis, and the electric field parallel to $\underline{\boldsymbol{B}}$. Such a configuration would drive a π transition.

A π transition is defined as one in which the magnetic quantum number (m_I, m_J, m_L, m_S, m_F) is not changed. This can also be described by $\Delta m = 0$, as shown in the third point in the previous section.

As can be seen in figure 2.7, in order for π transitions to be driven, the light must be linearly polarised and $\hat{\mathcal{E}} \cdot \hat{B} \neq 0$. In this thesis, the magnetic field used is parallel rather than perpendicular to the beam, so π transitions should not be observed.

A small pertubation along $\underline{\boldsymbol{k}}$ can lead to a non-zero component in the perpendicular axis rather than parallel axis, which would drive π transitions. In order to not drive π transitions, it is therefore important to try to keep $\underline{\boldsymbol{k}}$ purely parallel to $\underline{\boldsymbol{B}}$, so that there are no perpendicular components present.

2.4.4 σ Transitions

Light where $\underline{\boldsymbol{k}}$ is parallel to $\underline{\boldsymbol{B}}$, rather than perpendicular, $\mathcal{E}$ is perpendicular to $\underline{\boldsymbol{B}}$ and is circularly polarised, drives a transition which follows the rule $\Delta m = |1|$. This transition is called a σ transition. For $\Delta m = +1$, this is called a σ^+ transition, and σ^- for $\Delta m = -1$. These matrix elements were defined by the first two points in section 2.4.2.

From a planar perspective of looking into the beam, if the polarisation is anticlockwise in time this is called 'left hand circularly polarised'. The polarisations of the light are defined in 2.4.1. The electric field has components in both the x and y axes and is given by

$$\underline{\boldsymbol{\mathcal{E}}} = \mathcal{E}_0(\underline{\hat{\boldsymbol{x}}} + i\underline{\hat{\boldsymbol{y}}})e^{i(kz-\omega t)}, \tag{2.20}$$

and the spin S_z has a angular momentum change of $+1\hbar$ relative to the

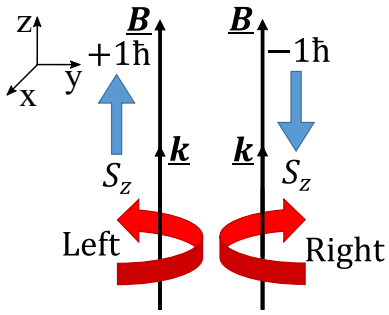

Figure 2.8: Left: Diagram showing left hand circularly polarised (LHCP) light driving σ^+ transitions.
Right: Diagram which shows right hand circularly polarised (RHCP) light driving σ^- transitions.

magnetic field axis, and therefore this type of light drives a σ^+ transition. This is shown on the left side of figure 2.8.

The right hand side of the diagram shows 'right hand circularly polarised' light where, from the perspective of looking into the beam, the polarisation is clockwise [51]. The electric field in this case is given by [52]

$$\underline{\boldsymbol{\mathcal{E}}} = \mathcal{E}_0(\hat{\underline{\boldsymbol{x}}} - i\hat{\underline{\boldsymbol{y}}})e^{i(kz-\omega t)}, \tag{2.21}$$

which leads to a angular momentum change of $-1\hbar$ relative to the magnetic field axis, which therefore drives a σ^- transition.

In the lab, linear light polarised along the $\hat{x}$ or $\hat{y}$ axes is often used. For example, light polarised along the $\hat{x}$-axis is given by $\hat{x} = \frac{1}{2}(RHCP + LHCP) = \frac{1}{2}(\hat{x} + i\hat{y}) + \frac{1}{2}(\hat{x} - i\hat{y})$. In this case, half of the light is LHCP and therefore driving σ^+ transitions, and half of the light is RHCP and therefore driving σ^- transitions.

If the magnetic field is large enough that the two types of σ transitions are far detuned from one another, then at maximum, 50 % of the total light could be absorbed by the atom at a given frequency, rather than 100 % normally seen at no magnetic field.

2.5 Effect of Temperature on Light-Matter Interactions

As previously stated, one of the focusses of this thesis is observing the behaviour of an atom in the hyperfine Paschen-Back regime under the influence of different temperatures. In this section, the theory behind the influence of temperature on light-matter interactions will be discussed.

2.5.1 The Electric Susceptibility

As discussed in section 1.1.4, changing the temperature of a medium can fine-tune the strength of the light-matter interaction. As temperature increases, the vapour pressure increases as seen in figure 1.1 and equation 1.1. The vapour pressure P_v in Pascals (Pa) relates to the number density $\mathcal{N}$ as

$$\mathcal{N} = \frac{P_v}{k_{\mathrm{B}} T}, \tag{2.22}$$

where T is the temperature in Kelvin K, k_{B} is the Boltzmann constant, and 1 atm of pressure is equal to 101325 Pa. For a transition with Rabi frequency

$$\Omega = -\frac{\mu \mathcal{E}_0}{\hbar}, \tag{2.23}$$

where μ is the electric dipole operator, the number density $\mathcal{N}$ has a linear relationship to the steady-state electric susceptibilty of stationary atoms, given by [53, 54]

$$\chi(\Delta) = \frac{\mathcal{N}\mu^2}{\hbar\epsilon_0} f_\Gamma(\Delta), \tag{2.24}$$

where $f_\Gamma(\Delta)$ is the complex lineshape factor described by

$$f_\Gamma(\Delta) = \frac{i}{\frac{\Gamma}{2} - i\Delta}. \tag{2.25}$$

The real and imaginary parts of the steady-state electric susceptibilty $\chi(\Delta)$ given by

$$\chi_{\mathrm{Re}}(\Delta) = -\frac{\mathcal{N}\mu^2}{\hbar\epsilon_0} \frac{\Delta}{\Delta^2 + \Gamma^2/4}, \tag{2.26}$$

$$\chi_{\mathrm{Im}}(\Delta) = \frac{\mathcal{N}\mu^2}{\hbar\epsilon_0} \frac{\Gamma/2}{\Delta^2 + \Gamma^2/4}, \tag{2.27}$$

where Γ is the decay rate of the atom, and Δ is the frequency detuning between the driving light field and the particular atomic transition.

2.5.2 Lorentzian Lineshape

In equation 2.25, the complex function lineshape of $f_\Gamma(\Delta)$ was described. The Fourier transform of an exponential decay is described by the Lorentzian [55]. As the excited state has a finite lifetime τ, the spontaneous emission from this state leads to the imaginary part of the lineshape being a homogeneous Lorentzian.

The natural linewidth (full width at half maximum) for the Lorentzian is known as Γ_0, which is related to the radiative lifetime of the excited state τ_R as $\Gamma_0 = 1/\tau_\mathrm{R}$ and is given by [54]

$$\Gamma_0 = \frac{{\omega_0}^3}{3\pi\hbar\epsilon_0 c^3}\frac{g_g}{g_e}\mu^2, \tag{2.28}$$

where g_g, g_e are the degeneracies of the ground and excited state respectively. The value of the natural linewidth for the D2 transition of Rubidium is given by $\Gamma_0 = 2\pi \times 6.065$ MHz [56], and is therefore not dependent on the temperature of the system.

Including the effects of temperature on number density leads to a collisional interaction between identical atoms: this is called self- broadening. To account for self- broadening an additional term in the Lorentzian linewidth Γ is required:

$$\Gamma = \Gamma_0 + \Gamma_\mathrm{self} = \Gamma_0 + \beta\mathcal{N}, \tag{2.29}$$

where β is known as the self-broadening coefficient, and for the D2 transition can be calculated by [57]

$$\beta = \sqrt{2}\frac{2}{9\hbar\epsilon_0}d_2^2 = 2\pi \times \sqrt{2}\ \Gamma\left(\frac{\lambda}{2\pi}\right)^3, \tag{2.30}$$

where d_2 is the reduced dipole matrix element. This additional linewidth is known as collisional, pressure or self-broadening [58], and is plotted in figure 2.9, in comparison to the other types of broadening including Γ_0.

Γ_self is also defined as the inverse of a collisional time τ_0. For room temperature ($T = 300$ K), τ_0 for ^{87}Rb, which has $\beta = 2\pi \times 1.03 \times\ 10^{-7}$ Hz cm^3, is approximately 0.1 ms. Changing only the temperature to $T = 473.15$ K, the lifetime is then approximately $\tau_0 = 1.7$ ns.

2.5.3 Power Broadening

For a two-level atom, the intensity at which the stimulated emission is equal to the spontaneous emission of the atoms is called the saturation intensity, I_{sat}, and is given by

$$I_{\text{sat}} = \frac{\hbar\omega_0\pi}{3\lambda^2\tau}, \tag{2.31}$$

where λ is the wavelength of the transition. Using $\omega_0 = kc$, $\lambda = \frac{2\pi}{k}$ and $\tau = \frac{1}{\Gamma}$, equation 2.31 can also be written as [59]

$$I_{\text{sat}} = hc\frac{\Gamma k^3}{24\pi^2}, \tag{2.32}$$

where Γ is from equation 2.29, k is the wavenumber and c is the speed of light. For the D2 transition of ^{87}Rb, $I_{\text{sat}} = 1.67$ mW cm^{-2}.

There also exists a power broadening part of the linewidth, which related to the saturation intensity of the two-level transition by

$$\frac{2\Omega^2}{\Gamma^2} = \frac{I}{I_{\text{sat}}}, \tag{2.33}$$

where Γ is sum of the natural linewidth and the self-broadened linewidth from equation 2.29. Including the power and natural broadening, the linewidth can now be given by

$$\Gamma = \Gamma_0\sqrt{1 + \frac{I}{I_{\text{sat}}}}, \tag{2.34}$$

and so in order to minimise the power broadening of the system, $\frac{I}{I_{\text{sat}}}$ must be minimised. However, the intensity of the beam must still be large enough to provide an output beam that a photodiode can detect. Too weak a beam will mean that the signal to noise ratio (SNR) will not be large enough to measure the absorption lineshapes precisely or accurately. Therefore a regime in which the power broadening is not significant is named, known as the Weak Probe Regime, defined as $I \ll I_{\text{sat}}$. The ElecSus program is written to calculate the value of the electric susceptibilty assuming this Weak Probe Regime.

2.5.4 Gaussian Lineshape

Due to atomic motion, there also exists a temperature dependent lineshape: the Gaussian. The Maxwell-Boltzmann distribution describes the probabilty distribution of an atom having a particular velocity v_z along the z-axis,

$$P(v_z)dv_z = \sqrt{\frac{1}{\pi u^2}}\exp\left[-\left(\frac{v_z}{u}\right)^2\right]dv_z, \tag{2.35}$$

where u is the $1/e$ width equal to $\sqrt{2k_{\mathrm{B}}T/m}$, where T is temperature in Kelvin and m is the mass of the atom. The broadening from the Doppler effect is given by the full width half maximum of the Gaussian distribution is

$$\Gamma_{\mathrm{D}} = \Delta\omega_{\mathrm{D}} = 2\sqrt{\ln 2}ku, \tag{2.36}$$

which is plotted in figure 2.9 against natural broadening Γ_0 and self-broadening Γ_{self}. For temperatures up to approximately 225 °C, Γ_{D} significantly larger than the other broadening parameters of the lineshape.

For an atom with zero velocity, the resonant frequency is given by ω_0. If that atom moved along the z-axis with velocity v_z the resonant frequency would be seen from the lab frame as

$$\omega_0' = \omega_0(1 - \frac{v_z}{c}), \tag{2.37}$$

which is known as the Doppler effect. Redefining equation 2.37, the detuning from resonance Δ can be altered to include the thermal motion of the atoms as

$$\Delta' = \Delta - kv_z. \tag{2.38}$$

Thus, the Doppler effect can be included in the electric susceptibilty of a particular atom moving at a velocity v_z by

$$\chi(\Delta - kv_z) = -\frac{\mathcal{N}\mu^2}{\hbar\epsilon_0}f_\Gamma(\Delta - kv_z) = -\frac{\mathcal{N}\mu^2}{\hbar\epsilon_0}\frac{1}{(\Delta - kv_z) + i\Gamma/2}. \tag{2.39}$$

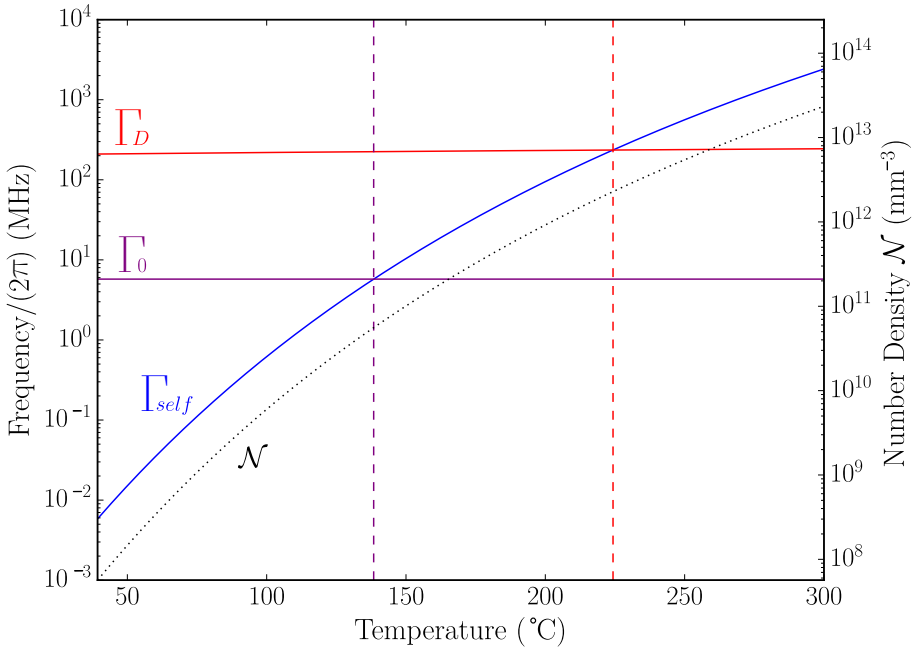

Figure 2.9: Evolution of the Self-Broadening linewidth as a function of temperature in blue, and the number density $\mathcal{N}$ shown as the black dotted line. Also shown is the linewidth from the Doppler broadening as a function of temperature in red, and the natural linewidth. The vertical dashed lines show the temperatures that the self-broadening linewidth cross the natural linewidth in purple and the Doppler linewidth.

2.5.5 Voigt Lineshape

Including both the Gaussian and Lorentzian lineshapes culminates in the Voigt lineshape, $s(\Delta)$, which is given by the convolution of $f_\Gamma(\Delta - kv_z)$ from equation 2.25 with equations 2.34 and 2.35, defined as

$$s(\Delta) = \int_{-\infty}^{+\infty} f_\Gamma(\Delta - kv_z) \times P(v_z) dv_z. \tag{2.40}$$

This can be thought of microscopically as each possible velocity following an individual Lorentzian linewidth, and macroscopically as the set of atoms distributed normally around the natural frequency. In order to obtain the absorption profile of the atomic ensemble, a sum of each of the individual velocities is taken. Averaging the possible velocities leads to I_{sat} increasing, as the probe beam interacts with fewer atoms.

For the amplitude of a Voigt lineshape, the strength of the transition (C^2) is

important. The electric susceptibilty can then be given by

$$\chi = C^2 \frac{\mathcal{N}\mu^2}{\hbar\epsilon_0} s(\Delta). \tag{2.41}$$

2.5.6 The Weak Probe Regime

The weak probe regime is defined as when the laser light's incident intensity is weak enough that the absorption coefficient along with other properties of the medium are not significantly perturbed. As the power of the incident beam is increased, the power broadening of the system increases according to equation 2.34, and therefore less light is absorbed by the atom.

In systems with multiple, non-degenerate ground states, a population transfer from the resonant ground state may occur via spontaneous decay from the excited state. When the selection rules of the transition mean that there is no allowed decay from the off-resonant ground state back to the original ground state, the off-resonant ground state is known as 'dark' (i.e.: transparent to the laser beam). This is called optical pumping [60]. While the population of the excited state remains small, the population of the resonant ground state is reduced. A diagram of this process is shown in figure 2.10. As discussed in [39], when a dark state is included, the population dynamics change as the optical pumping process time scale is lengthened.

As this population shift takes place, fewer atoms are available to be pumped to the excited state by the laser. This leads to a reduction in possible absorption of light on resonance. Collisional redistribution can return the atoms to the original state, but the timescale for this is usually longer than the time-of-flight of the atoms in the beam [39]. Therefore, in order to compare measurement to the theory from ElecSus, the intensity of the laser should be reduced such that the weak probe regime can be ensured.

However, reducing the beam's intensity means that the signal-to-noise ratio is decreased. It is therefore important to know the limits of the regime, so the SNR can be maximised while still remaining in the weak probe regime.

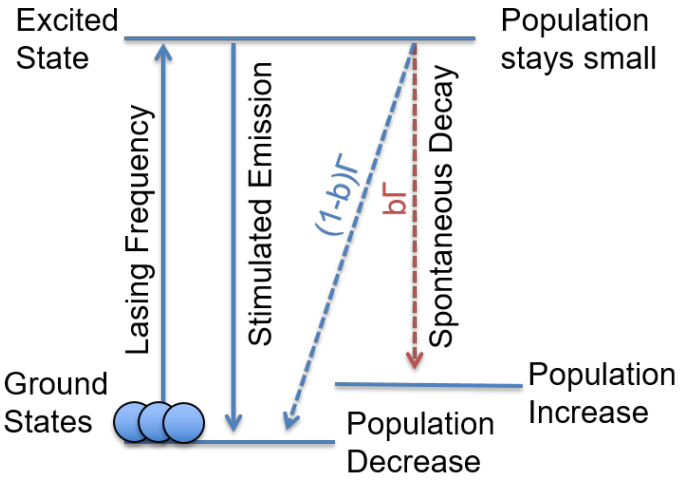

Figure 2.10: Diagram showing the ground state population shift due to optical or hyperfine pumping, with more than one non-degenerate ground state. Spontaneous decay is shown as dashed lines, with the decay to the dark state shown in red and the branching ratios given for each decay. Stimulated emission to the resonant ground state is shown as a solid line.

The convention for discussing the weak probe regime uses the ratio of intensity and the saturation intensity of the transition. Using equation 2.31, for a two-level atom, a saturation intensity I_{sat} can be defined as

$$I_{\text{sat}} = \frac{\hbar\omega_0}{2\sigma_0\tau}, \tag{2.42}$$

where $\hbar\omega_0$ is the energy separation between the ground and excited state, τ is the lifetime of the excited state, and σ_0 is the resonant excitation cross-section given by

$$\sigma_0 = \frac{3\lambda^2}{2\pi}, \tag{2.43}$$

where λ is the wavelength of the transition. Note this is identical to the relation given in equation 2.31.

The relationship between the relative line centre absorption $\frac{\alpha(\mathrm{I})}{\alpha(0)}$ of a transition and the $\mathrm{I}/\mathrm{I}_{\text{sat}}$ ratio can be defined in two different ways [39, 49]. The homogeneous, Lorentzian line-centre absorption is defined as

$$\frac{\alpha(\mathrm{I})}{\alpha(0)} = \frac{1}{1+\mathrm{I}/\mathrm{I}_{\text{sat}}}, \tag{2.44}$$

for power-broadened, stationary atoms, shown in figure 2.11 as the black dashed line.

Meanwhile, for power-broadened, inhomogeneous moving atoms the relationship is defined as

$$\frac{\alpha(\mathrm{I})}{\alpha(0)} = \frac{1}{\sqrt{1+\mathrm{I}/I_{\mathrm{sat}}}}, \tag{2.45}$$

shown in figure 2.11 as the solid red line.

As shown in figure 2.9 for temperatures below approximately 225 °C, the Doppler-broadening Γ_{D} is dominant over the Γ_0 and Γ_{self} broadening parameters at the line-center. Therefore, using equation 2.34, the intensity dependence of the light center absorption is dominated by the Doppler-broadening, and so the line-center of the Voigt profile follows the inhomogeneous relationship given by equation 2.45.

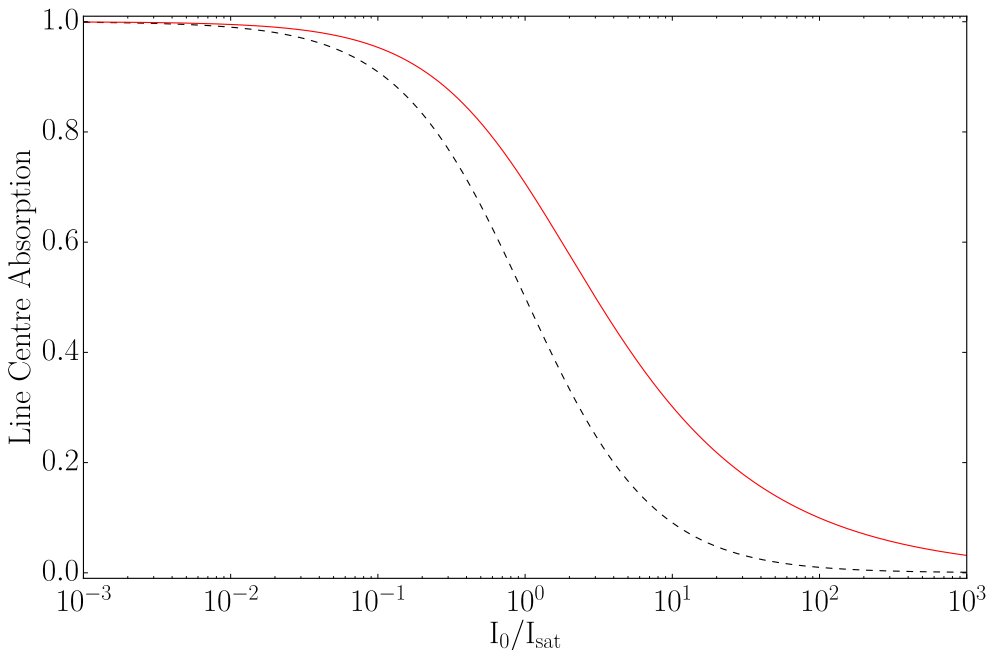

Figure 2.11: Characteristics of a inhomogeneous 2.45 (solid red line) and homogeneous 2.44 (black dashed) absorption line.

2.5.7 Absorption Coefficient

Each transition has a corresponding absorption coefficient α, which can be given in terms of the imaginary part of the electric susceptibility $\chi_{\text{Im}}(s)$ from equation 2.41 as [46, 61]

$$\alpha = k\chi_{\text{Im}}(s), \tag{2.46}$$

where $k = \frac{2\pi}{\lambda}$ is the wavevector of the light. For each $\sigma^{\pm}$ transition type, there is a corresponding absorption coefficient $\alpha_{\pm}$. It is important to note here that $\chi_{\text{Im}}(s)$ is temperature dependent, as shown in figure 2.9, the number density $\mathcal{N}$ rises very quickly as a function of temperature. The Doppler width is also temperature dependent, but as also shown by 2.9, this is to a much lesser extent as it is proportional to $\sqrt{T}$.

The transmission caused by these absorption coefficients depends on the polarisation of the light. If the light is polarised so that 100% drives σ^- transitions, the transmission parameter S_0 can be calculated by

$$S_0 = \exp\left(-\alpha_- \ell\right), \tag{2.47}$$

but for a laser beam that has a percentage p of light polarised so that it drives σ^- transitions, S_0 relates to both absorption coefficients by

$$S_0 = p \times \exp\left(-\alpha_- \ell\right) + (1-p) \times \exp\left(-\alpha_+ \ell\right), \tag{2.48}$$

where p is the percentage of light that is polarised so that it drives σ^- transitions. This equation shows that the transmission of light through the medium is also temperature dependent.

In figure 2.12, the evolution of the optical depth for the D2 line of the ^{87}Rb atom at a temperature of $T = 80$ °C over different magnetic field regimes is shown. Optical depth is the absorption coefficient α multiplied by the length of the cell $\ell = 1$ mm. Only $\sigma^{\pm}$ transitions are excited in this experiment. From these graphs, it is possible to observe the energy level splittings, and the change of regime from the weak field to the hyperfine Paschen-Back regime.

At $B = 0$ T, the $\sigma^{\pm}$ transitions are degenerate, as the states they are driving transitions from and to are degenerate with each other.

As the magnetic field is increased to $B = 0.05$ T, figure 2.5 shows that the excited state is in the HFPB regime, while figure 2.4 shows that for the ground state, the HLZ regime applies. σ^+ and σ^- are no longer degenerate, as the energy levels for which they drive transitions have split apart. However, the Doppler broadening of the states is still larger than the splittings. This means that it is not possible to observe each transition as an individual peak on the spectrum.

For $B = 0.10$ T, the splitting of the energy states has begun to be comparable to the Doppler broadening discussed in section 2.5.4, as the previously smooth peaks now have many individual peaks within them. The excited states are still in the HFPB regime, and at this magnetic field figure 2.4 shows the energy levels begin to curve and stop being linear functions of B, so enter the intermediate regime between the HLZ and HFPB regimes.

At $B = 0.60$ T, this becomes even clearer and the state splittings now dominate the Doppler broadening. The ground state begins to enter the HFPB regime at this magnetic field. Each transition can be observed individually, although there is still some overlap.

At this magnetic field, the larger peaks are the 16 transitions we expect to see following the σ^+, σ^- selection rules. The absorption coefficients of the largest 8 peaks are $3\times$ higher than the smaller 8 peaks, as we would expect from the transition strengths of these individual peaks, calculated from the equations in section 2.4.2. However, more transitions than the 16 expected can be observed. Although much smaller than the larger 16 'strong' transitions, 12 'weak' transitions in sets of 3 also occur. The origin of these 'weak' transitions will be explained later in this thesis.

At $B = 1.54$ T, the magnetic field used in this thesis, both the ground and excited states are within the HFPB regime. The symmetry of the $\sigma^\pm$ transitions can be observed, and the splitting of the energy levels now dominates the Doppler-broadening. The 'weak' transitions observed at 0.6 T have also become much weaker. In comparison to the absorption coefficients of the 16 expected transitions, the smaller peaks can barely be observed.

Such a high magnetic field is useful, as due to the large energy level splittings, the overlapping of the Voigt profiles of each transition (discussed in

section 2.5.5) is negligible. Each peak can be observed without significantly overlapping onto each other. Furthermore, the ratio in peak absorption coefficient between the larger and smaller 'strong' transitions is still 3, as expected from the Clebsch Gordon coefficients [62].

Transmission S_0 can also be defined as

$$S_0 = \frac{I(\ell)}{I_0}, \tag{2.49}$$

where $I(\ell)$ is the intensity of light after a medium of length ℓ and I_0 is the initial intensity before the medium.

A theoretical transmission spectrum over a scan of over 140 GHz from the 'ElecSus' program is shown in figure 2.13, where the magnetic field is 1.54 T, the temperature is $T = 130$ °C, the cell length is 1 mm, the atomic vapour within the cell is 100% ^{87}Rb, the polarisation of the light is linear and additional broadening from other gases in the cell is equal to approximately 80 MHz.

From this spectrum, the symmetrical energy level splitting can be observed. The high temperature means that the highest possible absorption has been reached at 50 %.

Also shown in this figure is an energy level diagram over magnetic field, and the relevant ground and excited energy levels for each $\sigma^{\pm}$ transition. The peaks from the 'weak' transitions are much larger here, as the temperature is higher. The states shown next to each energy level of the ground state show the admixtures of that state, including both the strong and weak components. The origin of these admixtures will be discussed in the next section.

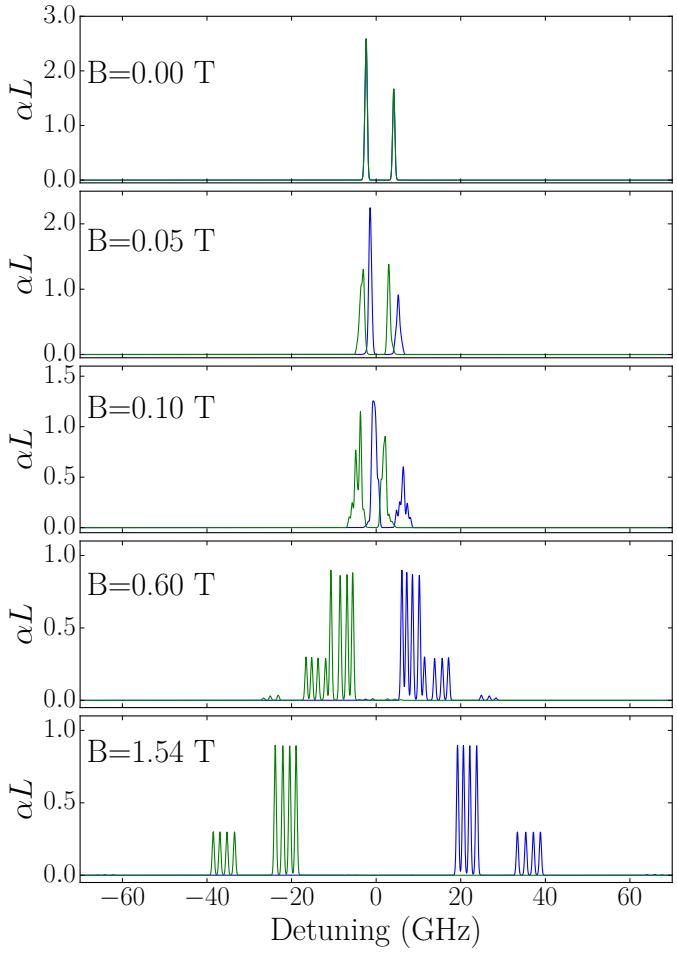

Figure 2.12: Theoretical evolution of the optical depth against linear detuning for different magnetic fields for the D2 transition of 100 % ^{87}Rb, $T = 80$ °C. In blue, the absorption coefficient for the σ^+ transitions (α^+) are shown, and in green the absorption coefficient for the σ^- transitions (α^-) is shown. The cell length ℓ is 1 mm.

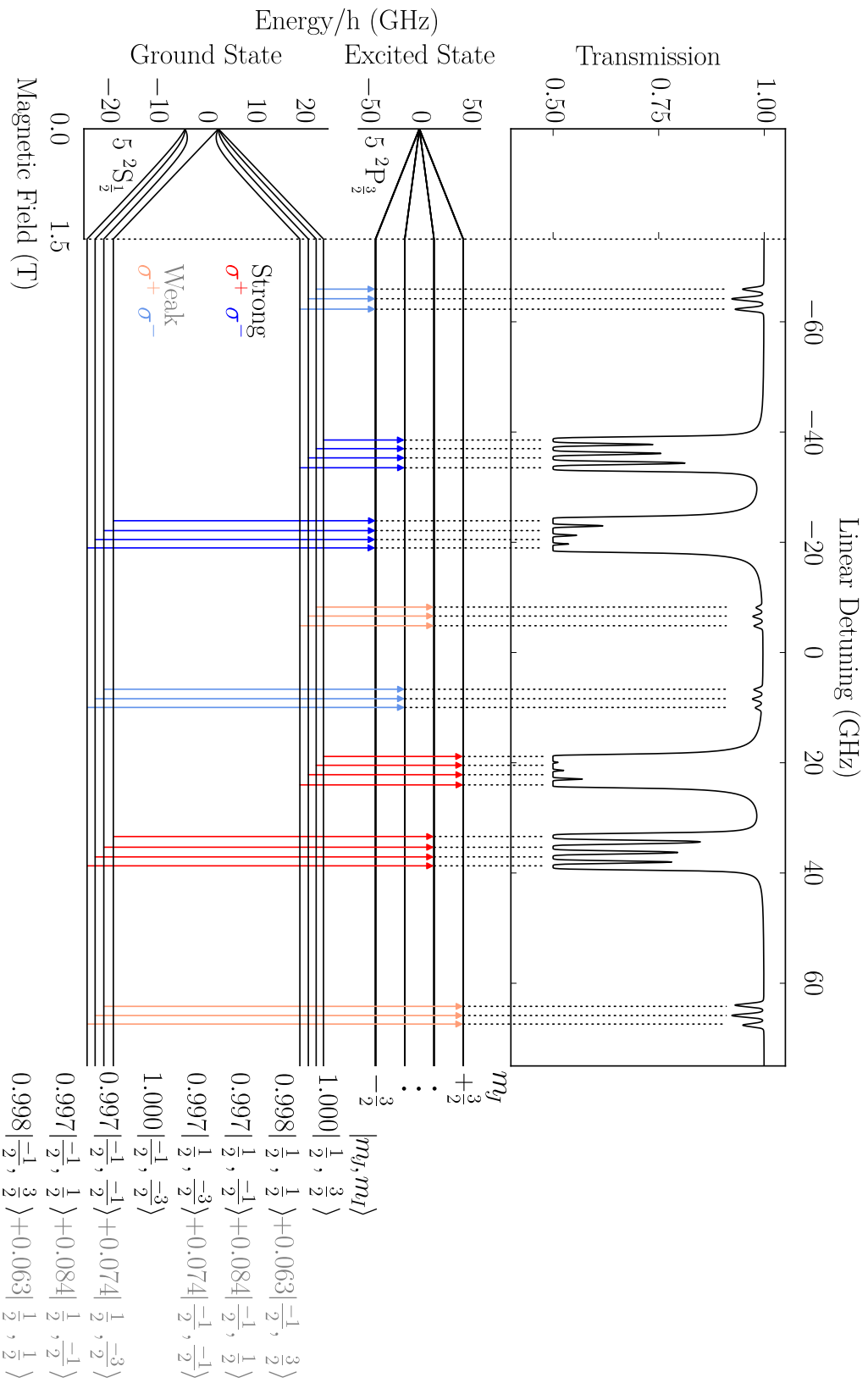

Figure 2.13: Diagram showing energy levels of both the 5 $^2S_{\frac{1}{2}}$ and 5 $^2P_{\frac{3}{2}}$, with the allowed σ^+ transitions in red, and σ^- transitions in blue. Weak transitions in paler corresponding colours are also shown, with the 'admixtures' of both the strong and weak components shown. Also plotted is a theoretical S_0 spectrum for ^{87}Rb at 130 °C, $B = 1.54$ T, with linear polarisation.

2.5.8 Weak Transitions

From figures 2.12 and 2.13, it would appear that there are additional transitions that do not come from the 16 $\sigma^{\pm}$ transitions expected, even at high magnetic fields [63]. This arises in the weak field, as the I, J quantum numbers are coupled to each other [46], and also in the hyperfine Paschen-Back regime because although I and J are mostly uncoupled, but not completely.

On the far right of figure 2.13, the 'admixtures' of each level are shown. Despite being in the HFPB regime, the numbers from the strong component of the energy level are not exactly 1, but are instead 0.997 or 0.998.

In the ground state shown in figure 2.4 and the bottom of figure 2.13, all the energy states have additional admixtures, except for the $\left|m_J = +\frac{1}{2}, m_I = +\frac{3}{2}\right\rangle$ state and the $\left|m_J = -\frac{1}{2}, m_I = +\frac{3}{2}\right\rangle$ state. This is because these two states have m_F values of ± 2 respectively in the weak field. However, the other 6 energy states all have one other weak coupled state, and m_F values of ± 1,0 in weak field. This is why we observe 16 $\sigma^{\pm}$ strong transitions, but only 12 $\sigma^{\pm}$ weak transitions.

For an electric dipole operator given by

$$-\hat{\boldsymbol{\mu}} \cdot \hat{\boldsymbol{\mathcal{E}}} = e\hat{\boldsymbol{r}} \cdot \hat{\boldsymbol{\mathcal{E}}}, \tag{2.50}$$

where e is the charge of the electron, and $\hat{r}$ is the unit vector of its position, the strength of the resulting transition can be described by

$$|\langle \Psi_a | \hat{\boldsymbol{\mu}} | \Psi_b \rangle|^2 = |\langle \Psi_a | - e\hat{\boldsymbol{r}} | \Psi_b \rangle|^2. \tag{2.51}$$

In the hyperfine Paschen-Back regime for an energy level with one strong component and one weak component, the wavefunction $|\Psi_A\rangle$ is given by

$$|\Psi\rangle = a_s \left|m_{J_s}, m_{I_s}\right\rangle + a_w \left|m_{J_w}, m_{I_w}\right\rangle, \tag{2.52}$$

where for the strong component s, m_{J_s} and m_{I_s} describe the m_J and m_I values, and a_s is the admixture, and vice-versa for the weak component w. This is normalised by

$${a_s}^2 + {a_w}^2 = 1, \tag{2.53}$$

and so the proportion of the strong component of the energy level is given by ${a_s}^2$, while for the weak component the proportion is given by ${a_w}^2$.

The furthest positively detuned 'weak' transition from figure 2.4 (at approx. +30 GHz at 0.60 T, and at approx. +70 GHz at 1.54 T), is a σ^+ transition so $\Delta m_J = +1$, and the wavefunction of the ground state Ψ_g can be given by

$$|\Psi_g\rangle = a_{g,s}\left|-\frac{1}{2},\frac{3}{2}\right\rangle + a_{g,w}\left|\frac{1}{2},\frac{1}{2}\right\rangle. \tag{2.54}$$

The relevant excited state for the σ^+ transition is the strong part of the second highest energy level from figure 2.5, with $|m_J, m_I\rangle = \left|\frac{3}{2},\frac{1}{2}\right\rangle$. Therefore the only non-zero part of the transition strength is given by

$$\begin{aligned} |\langle\Psi_e| - er|\Psi_g\rangle|^2 &= a_{g,w}a_{e,s}\left\langle\frac{1}{2}\middle|\frac{1}{2}\right\rangle\left|\left\langle+\frac{3}{2}\middle|-e\hat{\boldsymbol{r}}\middle|+\frac{1}{2}\right\rangle\right|^2 \\ &= a_{g,w}a_{e,s}\left|\left\langle+\frac{3}{2}\middle|-e\hat{\boldsymbol{r}}\middle|+\frac{1}{2}\right\rangle\right|^2, \end{aligned} \tag{2.55}$$

where $(a_{g,w})^2$ is the proportion of the weak component of the ground state, and $(a_{e,s})^2$ is the proportion of the strong component for the excited state.

Figure 2.14 shows that the coefficient $a_{e,s}$ (blue line, horizontal dashes) of the strong component of the excited state begins at 0 in the absence of an external magnetic field, and rapidly increases with magnetic field, and making up almost 100% of the energy level in the HPB regime.

Also shown the decline of the coefficient $a_{g,w}$ (blue, vertical dashes) of the ground state's weak component of the transition. This also shows how the excited state enters the HFPB regime at a much lower magnetic field than the ground state, as shown in figures 2.4 and 2.5.

In red is shown the strength of the transition, $a_{e,s}^2 \times a_{g,w}^2$, which peaks during the intermediate regime, and then asymptotically approaches 0 as the magnetic field increases. This explains why in figure 2.12, the weak transitions are much stronger at $B = 0.60$ T than at $B = 1.54$ T in comparison to the strong transitions.

For the magnetic field at which the peak in transition strength occurs (approx. 0.05 T), the energy levels have not yet split enough to be discernible from one another, as shown in figure 2.12. The Doppler broadening of the thermal atoms is still too large to view the weak transitions separately from the strong transitions.

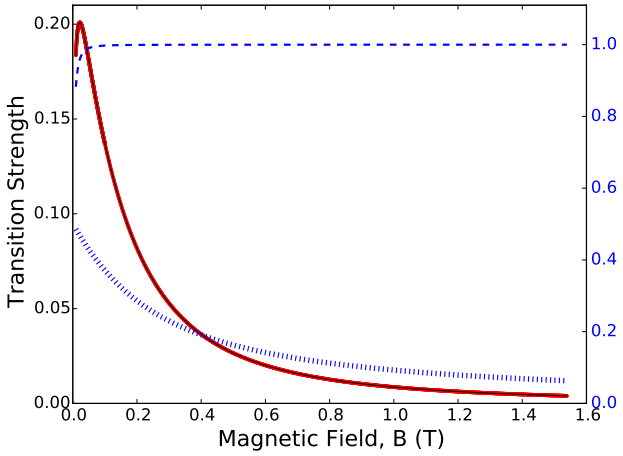

Figure 2.14: Graph showing the evolution of transition strength $a_{e,s}^2 \times a_{g,w}^2$ as a function of B, for the $\left|m_J = \frac{1}{2}, m_I = \frac{1}{2}\right\rangle \rightarrow \left|m'_J = \frac{3}{2}, m'_I = \frac{1}{2}\right\rangle$ transition (red line). The values of $a_{e,s}$ and $a_{g,w}$ are plotted in blue with vertical and horiztonal dashed lines respectively.

2.6 Stokes Parameters

Since 1852 [64], the polarisation state of light has been characterised by four parameters called 'Stokes Parameters'. Conveniently measurable [65] with linear optics and photodetectors, they are still used to measure the polarisation of light.

2.6.1 S_0 - Transmission

The transmission of light through a medium is equivalent to the S_0 parameter, given by

$$S_0 \equiv \frac{I_- + I_+}{I_0} = \frac{I_x + I_y}{I_0} = \frac{I_\nearrow + I_\searrow}{I_0} \tag{2.56}$$

where the x, y axes are defined respectively by the transmission and reflection of light at a polarising beam-splitter after the medium. Useful applications of the S_0 parameter include primary thermometry [66]. All three of these definitions are normalised by dividing by I_0, which is defined as the off-resonance transmission intensity. This means that the transmission can be given as a unitless number, between 0 and 1.

In this case, I_x refers to the intensity of the light that transmits through

such a beam-splitter, while I_y refers to the intensity of the light reflected. Similarly, $I_{\nearrow}$ and $I_{\searrow}$ refer to the intensity of light polarised at an angle $+45\,^{\circ}$ or $-45\,^{\circ}$ from the x-axis respectively. Additionally, I_- and I_+ denote the intensities of light that drive the $\sigma^{\pm}$ transitions.

A setup that can be used to measure an S0 spectrum is shown in figure 2.15.

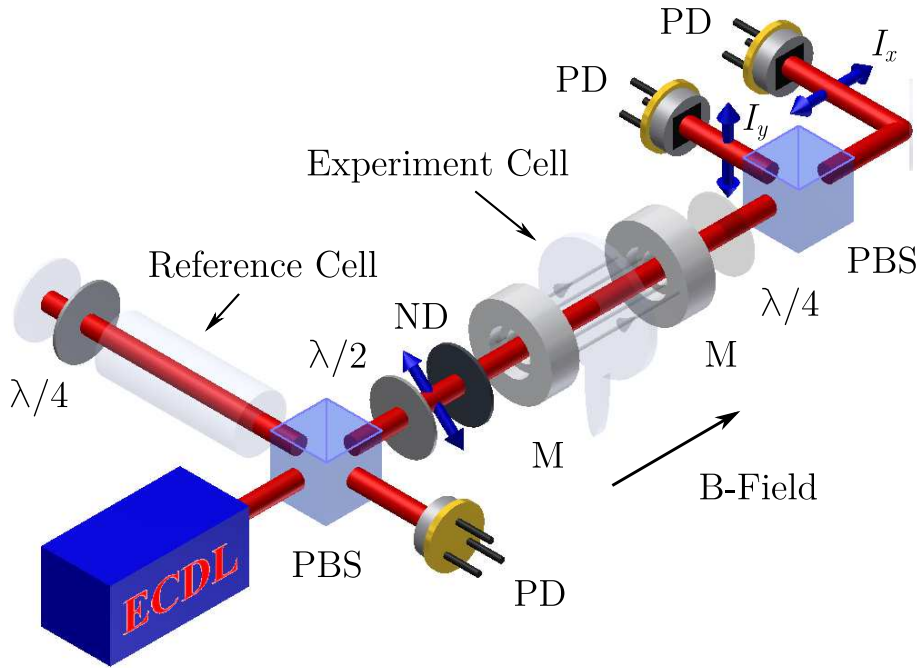

Figure 2.15: Diagram showing an example of a schematic laboratory setup for the measurement of an S0 or S1 signal. ECDL refers to an external cavity diode laser, PBS refers to polarisation beam splitter, PD refers to a photodiode, $\lambda/2$ and $\lambda/4$ refers to half-wave plates and quarter-wave plates respectively. The linear polarisation is shown by the blue arrows, ND refers to a neutral density filter and M refers to the magnet. This figure is taken from [46].

Light is emitted from a laser, and either reflects or transmits through a polarisation beam splitter, which makes it linearly polarised.

The light reflected from the PBS passes through the reference cell, and passes through a $\lambda/4$ or quarter-wave plate twice, which reverses the direction of its polarisation. The light is reflected back through the reference cell, and due to the polarisation change it is now transmitted through the PBS and arrives at the Photodiode (marked as 'PD') at the bottom of the diagram.

This first section of the schematic is used for Sub-Doppler spectroscopy.

The light that transmits through the first PBS in the schematic then passes through a $\lambda/2$, or half-wave plate and the polarisation after this waveplate is shown and is linear and rotated 45° from the horizontal. The neutral density filter is used to reduce the power broadening discussed in section 2.5.3.

The experimental cell is heated, and is shown between two magnets denoted by 'M', with the direction of the magnetic field shown by the arrow and denoted by 'B-field'. After this, an optional $\lambda/4$ waveplate is shown, which can be used for measuring different Stokes parameters.

There is a second PBS, where the y-axis is defined by the polarisation of the light reflected from the PBS, shown by the vertical arrow and intensity of which is denoted by I_y, which transmits into a PD. The x-axis is defined by the polarisation of the light that is transmitted through the PBS, shown by the horizontal arrow and the intensity of which is denoted by I_x, which transmits into a different PD.

At the top of figure 2.16, an S_0 spectrum is shown. The weak transitions are shown at around $\pm$10 GHz and at $\pm$70 GHz.

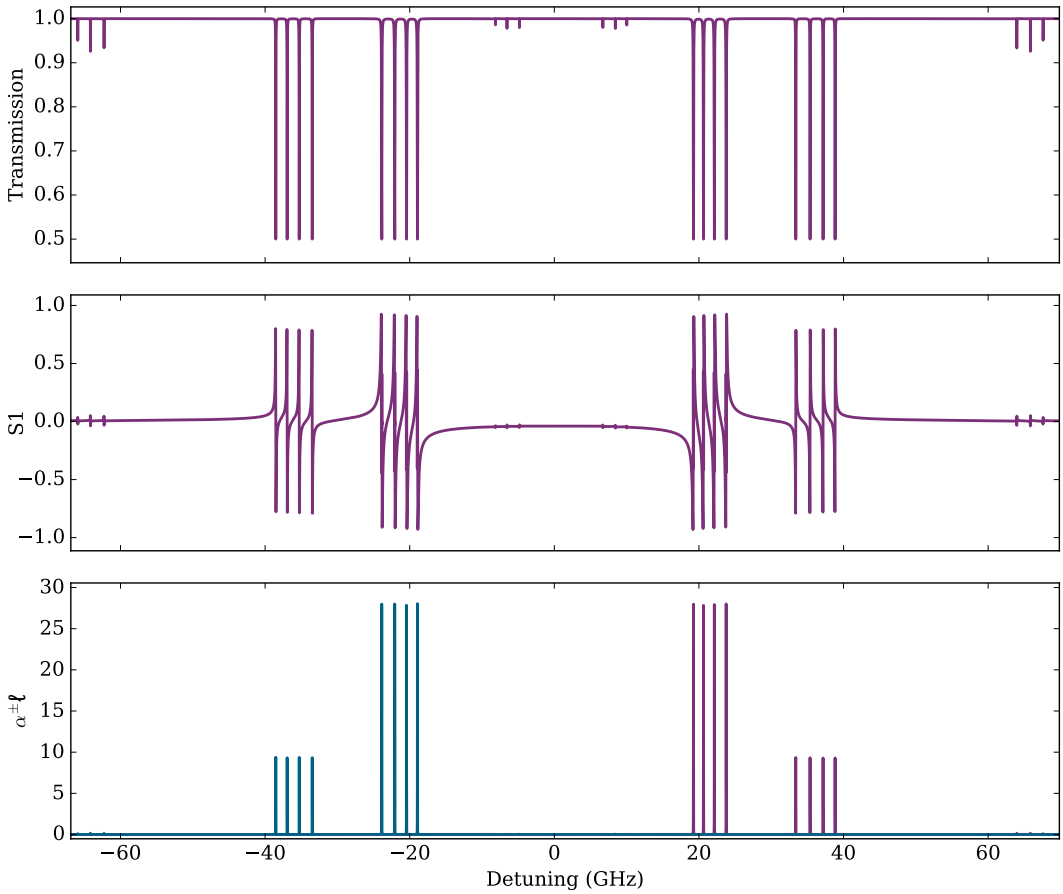

Figure 2.16: Theory plots of the D2 line for a 1 mm, 99% ^{87}Rb, 1% ^{85}Rb vapour cell of length $\ell = 1$ mm in a 1.54 T magnetic field, assuming no Doppler broadening, a linear polarisation, θ_0 of 45 ° and a temperature of 80 °C. TOP: A transmission (S_0) spectrum. MIDDLE: The S_1 spectrum, discussed later in section 2.6.2. BOTTOM: The optical depth ($\alpha \times \ell$) spectrum for both the α^+ (in purple) and α^- (in blue) coefficients, as discussed in section 2.5.7

Both the strong and weak transitions can be seen in the S_0 and S_1 spectra, but the absorption coefficients for the weak transitions are so much smaller than for the strong transitions that they cannot be observed at this scale.

2.6.2 S_1 and the Faraday Effect

The second Stokes parameter is called S_1 and is defined as

$$S_1 \equiv \frac{I_x - I_y}{I_0} \tag{2.57}$$

where I_x and I_y are again the intensities of light that are transmitted and reflected at a polarising beam-splitter, respectively, and I_0 is the transmission far-detuned from resonance. Normalising it in this way means that S_1 is a unitless parameter, between $-1 \leqslant S_1 \leqslant +1$.

In the HPB regime, the energy level splitting is high enough that the σ^+ and σ^- transitions are far detuned from one another, and so can be independently measured. This means that the refractive indices $n^\pm$ of the polarisations that drive the corresponding transitions will also be independent of one another, known as circular birefringence.

For an initial polarisation angle of σ_0 from the x-axis of 45 °, the S_1 spectra is sensitive to the rotation of polarisation from the Faraday effect. If the optical depth of the medium is small, these combined conditions mean that the equations [27]

$$S_1 \approx (n^- - 1)k_0\ell, \tag{2.58}$$

$$S_1 \approx (1 - n^+)k_0\ell, \tag{2.59}$$

become valid, where k_0 is the wavenumber of light in a vaccuum, which has the relation $k = nk_0$, where n is the refractive index of the medium. This S_1 parameter is shown in the middle of figure 2.16. Particularly noticeable is that the 'tails' of each of the peaks do not reduce to 0 as quickly as they do for the S0 spectra (top graph). The off-resonance wings of the resonance peak follow a lorentzian lineshape [67], and continue to decrease infinitely. This is particularly useful for applications such as off-resonance laser locking [68–70].

The temperature dependence of the S_1 parameter at a magnetic field of 1.54 T for a 99% ^{87}Rb, 1% ^{85}Rb cell of length 1 mm is shown in figure 2.17. At room temperature $T = 300$ K, the S_1 signal is small. As the temperature increases, both I_x and I_y change due to the Faraday effect [71], where the polarisation of the light is rotated by the axial magnetic field.

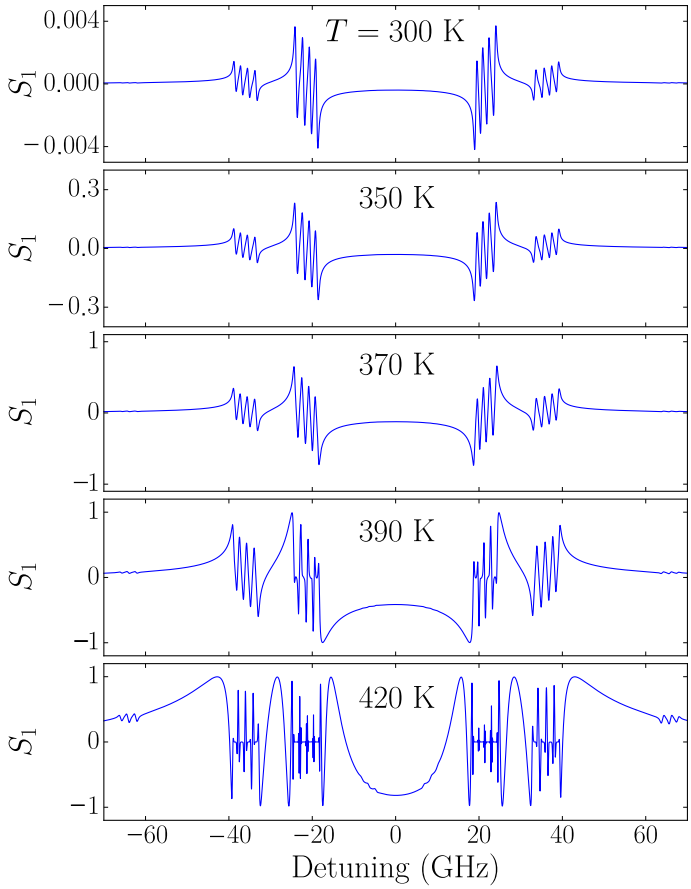

Figure 2.17: Array of graphs showing the S_1 spectra at different temperatures, with a magnetic field of 1.54 T, $\sigma_0 = 45$ °, for a 99% ^{87}Rb, 1% ^{85}Rb cell 1 mm in length, with linear polarisation (equal parts RHCP, LHCP light).

So as the S_1 parameter depends on $n^{\pm}$, (which is temperature dependent), S_1 is also temperature dependent. A graph showing a theoretical S_1 spectra for a specific temperature is shown in figure 2.18, and similarly to figure 2.13, the figure also shows the ground and excited state, the relevent transitions for each S_1 peak, and the admixtures of each energy level.

The S_1 spectrum can be measured using the same setup as displayed in figure 2.15, but instead of summing the I_x and I_y inputs, one is taken away from the other.

2.6.3 S_2 and S_3

The final two Stokes parameters are given by S_2 and S_3, which are described here for completeness and are not the focus of this thesis. The parameter S_2 is given by the equation

$$S_2 \equiv \frac{I_{\nearrow} - I_{\searrow}}{I_0}, \tag{2.60}$$

and along with the S_1 parameter is useful for far off-resonance laser frequency stabilising references [72].

The parameter S_3 is given by the equation

$$S_3 \equiv \frac{I_- - I_+}{I_0}, \tag{2.61}$$

which is the dichroic atomic vapour laser lock error signal [69, 73]. These parameters can be measured using the optional quarter-wave plate before the second PBS shown in figure 2.15

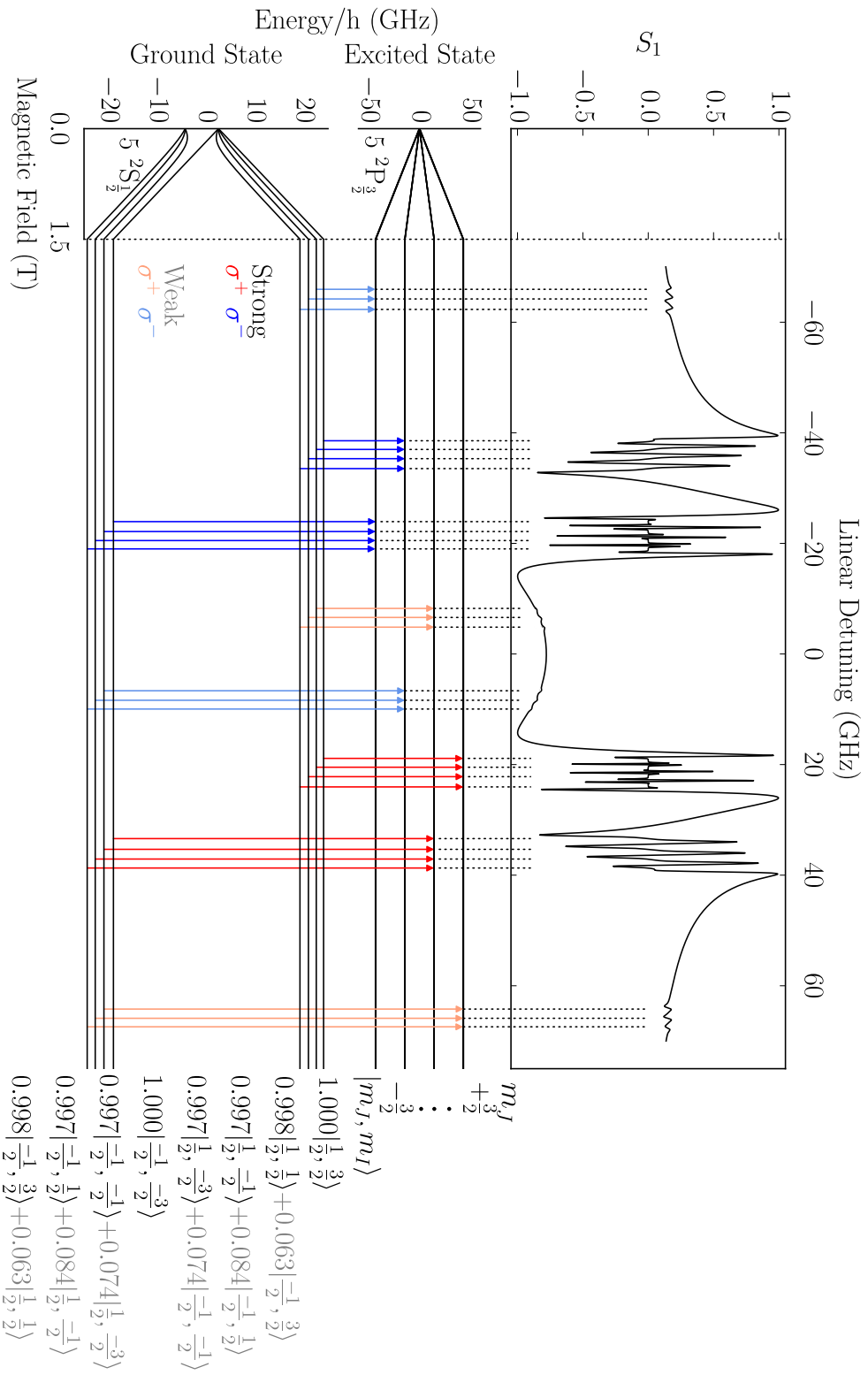

Figure 2.18: Diagram showing energy levels of both the $5\ ^2S_{\frac{1}{2}}$ and $5\ ^2P_{\frac{3}{2}}$, with the allowed σ^+ transitions in red, and σ^- transitions in blue. Weak transitions in paler corresponding colours are also shown, with the 'admixtures' of both the strong and weak components shown. Also plotted is a theoretical S_1 spectrum for ^{87}Rb at 130 °C, $B = 1.54$ T, with linear polarisation.

Chapter 3

Temperature Evolution of Stokes Parameters

As dicussed in section 2.5, the temperature of the vapour sets the atomic number density and this has a large effect on both the S_0 and S_1 Stokes Parameters. By using the 'ElecSus' program, theoretical spectra can be produced. In this chapter, this the temperature evolution of these parameters is experimentally investigated and compared to the theoretical spectra.

3.1 Experimental Methods

3.1.1 Experimental Setup

Figure 3.1 shows a schematic of the experimental setup used. In this diagram, the direction of the laser beam is shown by the red arrows, while the different components are shown in grey boxes. The aim of this section is to discuss the setup of the experiment itself.

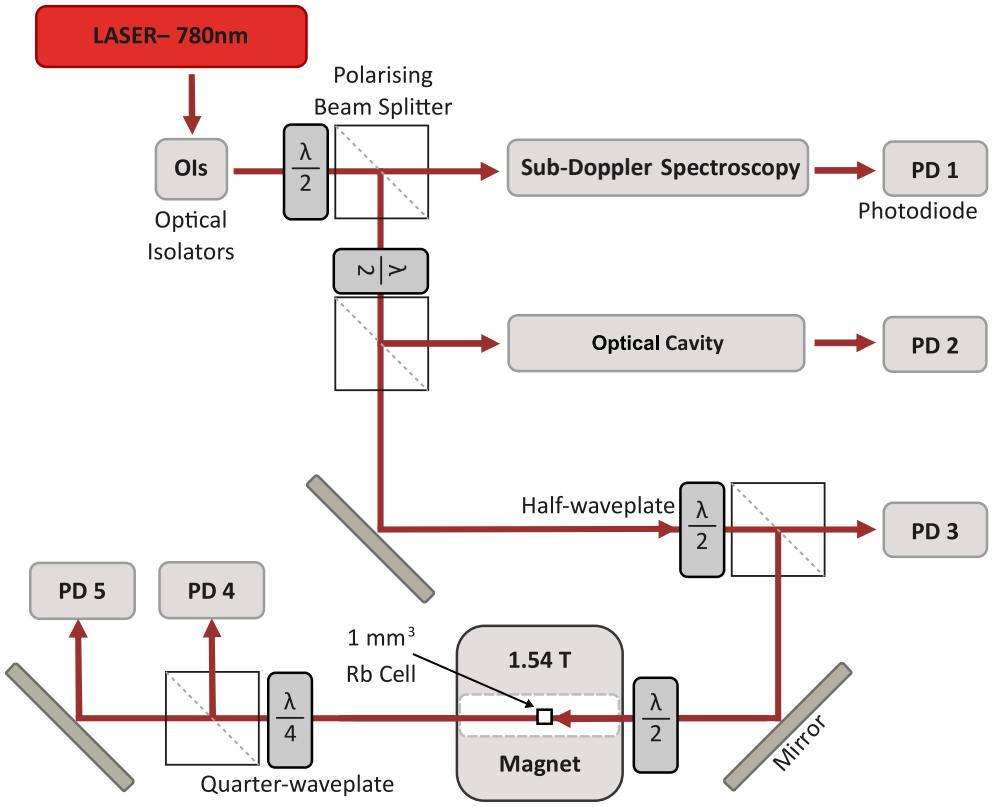

Figure 3.1: Diagram showing the layout of the experiment setup, the components of which are shown in labelled grey boxes. The photodiodes (PD) are numbered between 1 and 5 and were all connected to an oscilloscope which measured the voltage from each photodiode over time.

3.1.2 Laser

A laser scanning over the D2 line frequency of 780 nm was used. At a magnetic field of 1.54 T, the energy level splitting means that the furthest weak transitions are approximately 140 GHz detuned from one another, as shown in figure 2.13. The optical isolators shown in figure 3.1 directly after the laser were used to ensure no back-reflections would distort the laser signal.

In order to take a continuous measurement with a wide frequency scan that ranged over the entire 140 GHz detuning, a Distributed Feedback (DFB) laser at the relevant D2 transition wavelength of 780 nm was used. Such a wide scan is useful to have, as it means comparisons between different atomic transitions can be made more accurately than having two separate

scans, where the temperature of the medium or the power of the beam could have changed between measurements.

The frequency of the laser was controlled by changing its temperature. This meant that a continuous, unbroken scan over hundreds of GHz was possible, without the mode-hopping often seen in diode and other semiconductor lasers [74–76]. However, changing the temperature is a slow process, and in order to get a high SNR, each acquisition time was often over 2 minutes long. For narrow scans of specific peaks rather than the entire spectrum, a different laser was used in order to attain a more linear scan. A Toptica DL Pro laser at 780 nm was used for this purpose, which could scan frequency mode-hop free for a maximum of approximately 20 GHz. As the time for each scan was in the order of milliseconds rather than minutes, certain sources of uncertainty, such as temperature fluctuations, had a smaller effect.

3.1.3 Experimental Cell

As shown in figure 3.1, a Rubidium cell, referred to as the 'experimental cell' is placed in the centre of a cylindrical permanent magnet of maximum magnetic field $B = 1.54$ T. This cell was a cube with an optical path length 1 mm, and was made up of approximately 99% ^{87}Rb with 1% ^{85}Rb and a small amount of additional buffer gas.

3.1.4 Polarisation and Stokes Parameter

Directly before the magnet, a half-waveplate was placed. This made it possible to control the input polarisation of the laser beam. For example, when the experiment required linear polarisation, the half-waveplate could be used to ensure the light was polarised such that σ^+ and σ^- transitions would be driven equally. After the magnet, an optional quarter-waveplate is shown before a final PBS. This made it possible to also measure an S_3 signal by changing the output polarisations from I_x, I_y to I_-, I_+.

Finally, two photodiodes are placed after the PBS, with the reflected and transmitted light going to '**PD 4**' and '**PD 5**' respectively. The temperature of the experimental cell was measured using an external thermocouple

connected to a multimeter. Once the temperature stabilised and did not change more than 0.5°C over a few minutes, the laser was scanned.

In order to measure an S_0 spectrum, the final PBS could be removed so that all of the light is detected by one photodiode. This is equal to a sum of the polarisation components. Normalisation of the y-axis using the intensity signal therefore leads to a transmission y-axis between 0 and 1.

In order to measure an S_1 spectrum, the input polarisation would need to be set as $\theta_0 = 45° = \frac{\pi}{4}$ so that with no atom-light interaction, $I_x = I_y$. Rather than summing the two components, the I_y signal from '**PD 4**' is subtracted from the I_x '**PD 5**' signal. Normalising the y-axis leads to a maximum signal of $+1$ and a minimum signal of -1.

3.1.5 Normalisation of the detuning and transmission axes

In order to compare the experiment with the theoretical data from the 'ElecSus' program, the y-axis of the data would have to be normalised to between 0 and $+1$ for the S_0 plots, and to between -1 and $+1$ for the S_1 plots. However, the photodiodes measure the light intensity, outputting Voltage in units of V.

Additionally, as the laser scanned in frequency, the intensity of the beam changed. An intensity increase meant the voltage the photodiode recorded also increased, and vice versa. In order to correct for this effect, an additional photodiode labelled '**PD 3**' which was placed after an unobstructed beam so that the intensity change of the laser as it scanned could be measured. The experimental signal measured by '**PD 4**' in figure 3.1 was divided by the intensity signal measured by '**PD 3**'. The scale of the y-axis could then be obtained by setting the off-resonance value to 1.

Converting the x-axis from time into frequency was also necessary to compare with the theory given by the 'ElecSus' program. This was achieved using the well-known methods of using an optical cavity and Sub-Doppler spectroscopy in conjunction with one another. More information on this can be found in the Appendix B, as well as in [53].

3.1.6 Fitting the Data with 'ElecSus'

The 'ElecSus' program was used to fit the signal from the final, normalised data to the theoretical models by floating various fitting parameters. This enabled a theoretical signal to be produced and compared to the experimental data.

The temperature of the cell was difficult to measure accurately. While a temperature probe was used, early tests showed that there existed a systematic error on the measurements by up to 10 °C, as it was not possible to have the temperature probe directly next to the experimental cell itself. Therefore the temperature of the cell was used as a floating parameter in the 'ElecSus' program, using the temperature probe measurement as an initial value.

Other variables that were floated by the 'ElecSus' program while creating the theoretical signals included the polarisation of the light and the additional broadening caused by the existence of buffer gases in the cell. The initial value for the polarisation was measured by taking a very high temperature measurement, where the absorption has reached its maximum. By measuring the maximum absorption for both the σ^+ and σ^- transitions, the polarisation of the light could be found.

3.2 Wide Scan Results and Discussion

As the wide scan of the DFB laser took up to several minutes to complete, air currents or other external temperature fluctuations could change the temperature during the scan. By normalising the y-axis, turning off air conditioning, shielding the optical bench and limiting unnecessary movement or sound during data acquisition, fluctuations could be minimised.

3.2.1 The S_0 Parameter

The top section of figure 3.2 shows the raw signal measured from the photodiodes for the experimental and laser intensity measurements for a laser scan lasting 60 seconds, at a temperature of 56 °C. The bottom section of figure 3.2 shows the experimental signal divided by the intensity signal. The x-axis shows acquisition time in seconds.

Dividing the two photodiode signals does not normalise the data, however. The signal appears to have both an unexpected trend in the transmission, and also an oscillation that can clearly be seen off-resonance.

The trend in the transmission shows a minimum occurs at $t = 0$, while a maximum is reached at approximately 13 seconds, rather than the far off-resonance transmission all reaching the same value of 1 as expected, and has a magnitude that is not negligible in comparison to the absorption.

If temperature fluctuations on the laser itself were solely responsible for this trend in transmission, we could expect them to be present in the intensity signal from '**PD 3**' as well as the experiment signal from '**PD 4**', and the normalisation process would correct for these errors. While observation of the two signals makes them seem similar in form, the divided signal shows that the division does not compensate for everything. In order to adjust for extra trends seen, a 5th order polynomial was applied to the data to set the off-resonance sections to have a transmission = 1.

The oscillation of the two raw signals shown in the top section of figure 3.2 has a frequency of approximately 0.5 Hz in time, for the 60 second scan. After the x-axis was converted to frequency, this oscillation is seen to have a frequency

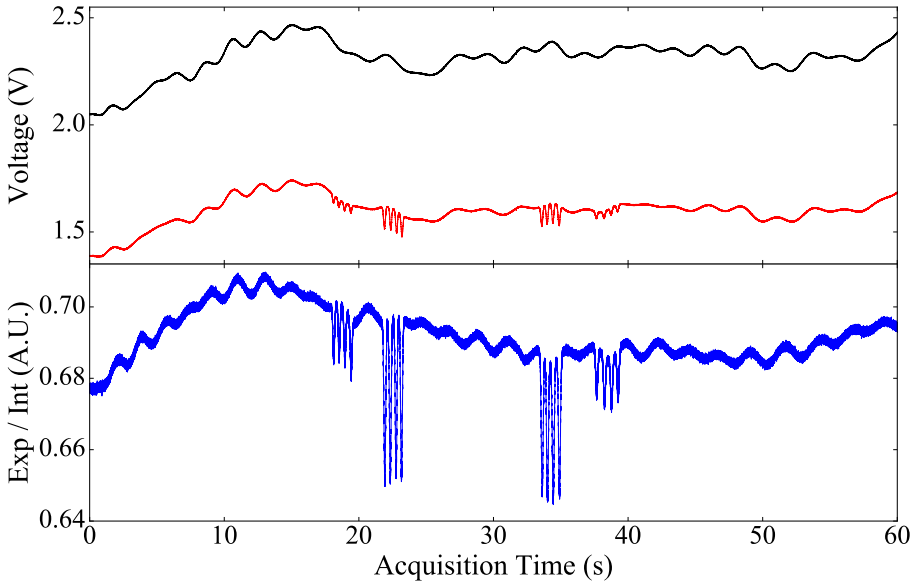

Figure 3.2: TOP: Raw data measured by the photodiodes '**PD 3**' (black) and '**PD 4**' (red) showing the intensity and experimental signals respectively, for one frequency scan of length 60 seconds, corresponding to part (a) from figure 3.5. BOTTOM: The experimental signal divided by the intensity signal in an attempt to normalise the data.

of 15 GHz as can be seen in figure 3.3. This oscillation was not due to the photodiodes, as no such oscillation was present in the background data, when the laser light was blocked.

The amplitude of the oscillation is difficult to measure precisely due to the underlying trend in the data, but for the intensity it ranges from approximately 4 to 50 mV. Using the simple error analysis method where the uncertainty is equal to half the data's range, the amplitude of the oscillation in the intensity measurement can be written as 1.0 $\pm$0.9 % of the raw intensity signal. This is imprecise as the uncertainty is equal to 90 % of the value itself.

Similarly, the oscillation for the experiment signal has an amplitude which ranges from 0.0025 V to 0.035 V, corresponding to 1.2 $\pm$1.0 % of the signal. Again, the amplitude varies so much over the scan that the uncertainty is equal to 83 % of the value. The variation of the amplitude reduces significantly by the division of the two signals, shown in the bottom section of figure 3.2 where it has a mean value, which is equal to 0.29 $\pm$ 0.07 % of

the divided value. This process reduces the range in the amplitude measurement to just 24 % of the value. Finally, a sinusoidal wave was fitted to the off-resonance parts of the scan in order to compensate for the oscillation, which reduced the oscillation's amplitude to 2.7 $\pm$ 0.6 % of the maximum absorption.

The x-axis of this data set is then converted from time to frequency (as discussed in Appendix B). For this particular data set, the final x-axis gave a mean difference between the 8 measured Sub-Doppler peaks and their corresponding accepted values of 0.0 ± 1.2 MHz, where the uncertainty is the standard error of the differences. The FWHM of each Sub-Doppler peak was ≈ 20 MHz. All of these Sub-Doppler peaks occurred between ± 5 GHz, while the entire data-set ranged from ± 70 GHz. This means that the scaling of the x-axis had to be applied to a region $> 28\times$ larger than the range of values used.

The final, normalised data-set can be seen plotted in the top section of figure 3.3, where the normalised experiment data and the corresponding theoretical fit from the 'ElecSus' program are shown on one figure. Also shown in these plots are the normalised residuals (defined as the difference between theory and experiment, divided by the error bar and given by equation A.1 in Appendix A) for an uncertainty equal to the off-resonance amplitude of the oscillation in the S_0 parameter observed.

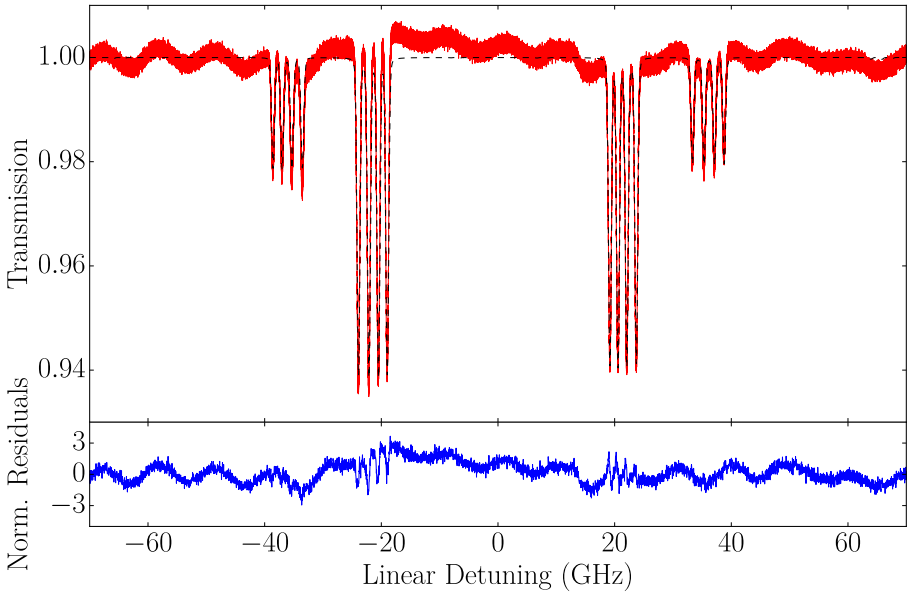

Figure 3.3: TOP: Data (red, solid line) and theoretical fit (black, dashed line) from (a) in figure 3.5. The theoretical parameters were: $T = 56.03$ °C and σ^- polarisation = 50.84%, to 2 d.p., assuming an additional broadening of 65 MHz. BOTTOM: Normalised residuals (blue), for an uncertainty equal to the off-resonance oscillation amplitude (= 0.002) giving $\chi^2_{\text{red}} = 0.96$.

The absorption of the light by the atoms is small enough that the largest absorption peak only reduces the transmission to approximately $S_0 = 0.94$. At this temperature, the absorption from the weak transitions (±10 GHz, ±70 GHz) is much smaller than the oscillation. It is therefore not possible to measure the absorption from the weak transitions accurately or precisely.

The normalisation of the y-axis was not perfect. Although drift in the laser's intensity was mostly corrected, not all effects could be removed. This is especially obvious between ±20 GHz, where a negative trend as frequency increases can be seen. There is also clearly still some oscillation. The amplitude of this oscillation off-resonance was measured to be = 0.002, and using this as the uncertainty, a χ^2 analysis of the fit gave a reduced value of $\chi^2_{\text{red}} = 0.96$. This oscillation is clearly the dominant source of uncertainty, as when included the χ^2_{red} is very close to 1 [77].

Other spectra were obtained at various different temperatures, and processed as discussed above. Figure 3.4 shows the results at 117 °C with residuals.

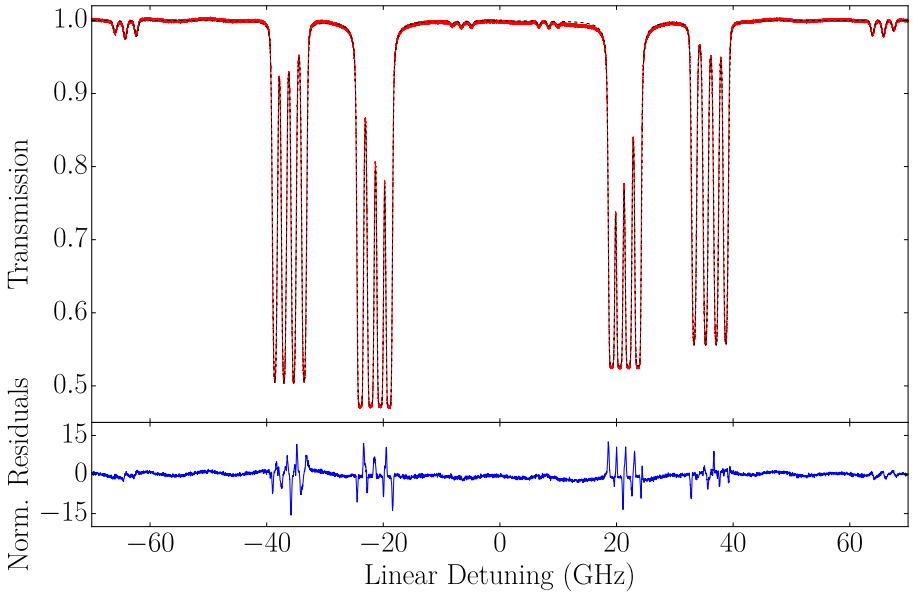

Figure 3.4: TOP: Data (red, solid line) and theoretical fit (black, dashed line) from (c) in figure 3.5. The theory parameters were: $T = 116.69$ °C and σ^- polarisation = 52.72% to 2 d.p., assuming a 65 MHz additional broadening. BOTTOM: Normalised residuals (blue), for an uncertainty equal to the oscillation's amplitude off-resonance (= 0.002) giving $\chi^2_{\text{red}} = 4.0$.

At this higher temperature, the strong transitions have begun to reach the maximum possible absorption at close to 0.5. The strong, negatively detuned transitions are reaching the maximum absorption at approximately 53%, while the strong positively detuned transitions have a maximum possible absorption of approximately 47%, as the polarisation is not exactly 50% pumping σ^- transitions.

The oscillation of the y-axis clearly seen in figure 3.3 can barely be observed. While the oscillation's amplitude is unchanged at = 0.002, this is now much less than the maximum absorption of light. Using this oscillation as the uncertainty for a χ^2 analysis of the fit found by the 'ElecSus' program, $\chi^2_{\text{red}} = 4.0$. Where in figure 3.3 all of the residuals are between ± 4, in figure 3.4 they are instead between ± 15. We can therefore conclude that at this higher temperature, the oscillation of the y-axis is no longer the dominant source of error. The process of normalisation of the x-axis must therefore be considered as a candidate for dominant source of error while scanning over such a large

frequency. In the vicinity of the sharp resonances, small errors in the detuning cause a large change in transmission as is evident from the residuals plot.

Finally, the evolution of the S_0 parameter over a range of temperatures is shown in figure 3.5. The temperatures 56 °C, 87 °C, 117 °C and 150 °C shown in figure 3.5 are all given with 2 significant figures, calculated from a fit to the experiment data using the 'ElecSus' program.

The form of these graphs shows excellent agreement with theory. Even the weak transitions that occur at frequencies of approximately ±10 and ±70 GHz are also shown in the theory. The 'ElecSus' program has successfully predicted the form of the temperature evolution of the S_0 parameter over a frequency range of ±70 GHz, and a temperature range of almost 100 °C, between a very small absorption to maximum absorption for a near-linear polarisation well into the hyperfine Paschen-Back regime at a magnetic field of 1.54 T, and therefore provides evidence of its reliability in these conditions.

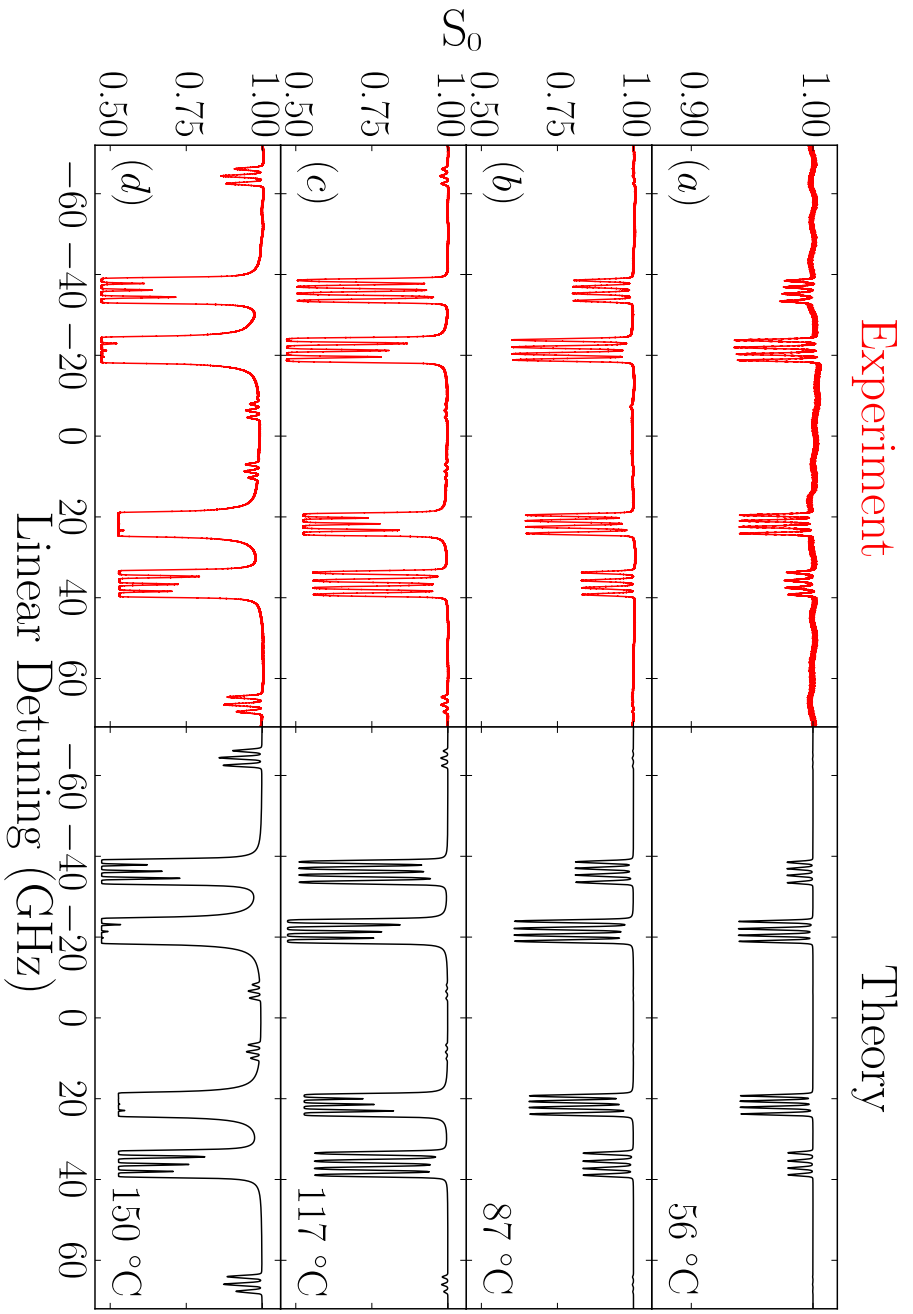

Figure 3.5: Experiment measurement (red) of the temperature evolution for the S_0 parameter for the experiment cell under an external magnetic field of $B = 1.54$ T ranging from 56 °C to 150 °C. The corresponding theoretical S_0 parameter fitted using the 'ElecSus' program is shown in black.

3.2.2 S_1 Parameter

The corresponding temperature evolution graph for the S_1 parameter is shown in figure 3.6. The same frequency detuning is used, but this time the temperature ranges between $75 - 160$ °C.

In these graphs, the oscillation in the y-axis is not observed. This is because measuring the S_1 parameter takes the difference between two photodiodes, and in the process the oscillation cancels itself out- known as common-mode rejection. We can therefore be sure that the oscillation is not a product of vibrations or other sources of error on the photodiodes themselves.

The S_1 parameter is useful to measure as it is directly proportional to the refractive index [78]. Furthermore, the zero crossings that occur at a high temperature can be used for frequency markers for locking lasers. This would be particularly useful at large detunings, as discussed in section 5 of [78]. In addition, the location of the zero crossings can be far less temperature sensitive than other parts of the S1 spectrum. Furthermore, the shape of these spectra is very sensitive to magnetic field. Currently, large magnetic fields tend to be measured using Hall probes. Figure 3.6 suggests atomic spectroscopy could be an alternative technique to measure large magnetic fields. Work is ongoing in this technique [79], and interest has been shown up to magnetic fields of 58 T [80].

As the temperature of the vapour increases and, as with the S_0 parameter, the number density increases, and therefore so does refractive index. The rotation angle of the polarisation of light is proportional to the refractive index difference between the σ^+ and σ^- transitions. As the temperature increases, the rotation angle Θ can exceed $\pi/2$ [72]. This is shown by parts (c) and (d) of figure 3.6, where the temperatures of ≥ 123 °C mean that the full range $-1 < S_1 < +1$ is observed, by the zero crossings that occur in those graphs.

The form of these graphs shows excellent agreement with theory at all temperatures. Even very sharp peaks in the experimental data are all matched by the theory. This provides evidence that the 'ElecSus' program can not only successfully predict the S_0 parameter, but also the S_1 parameter for an experiment far into the hyperfine Paschen-Back regime.

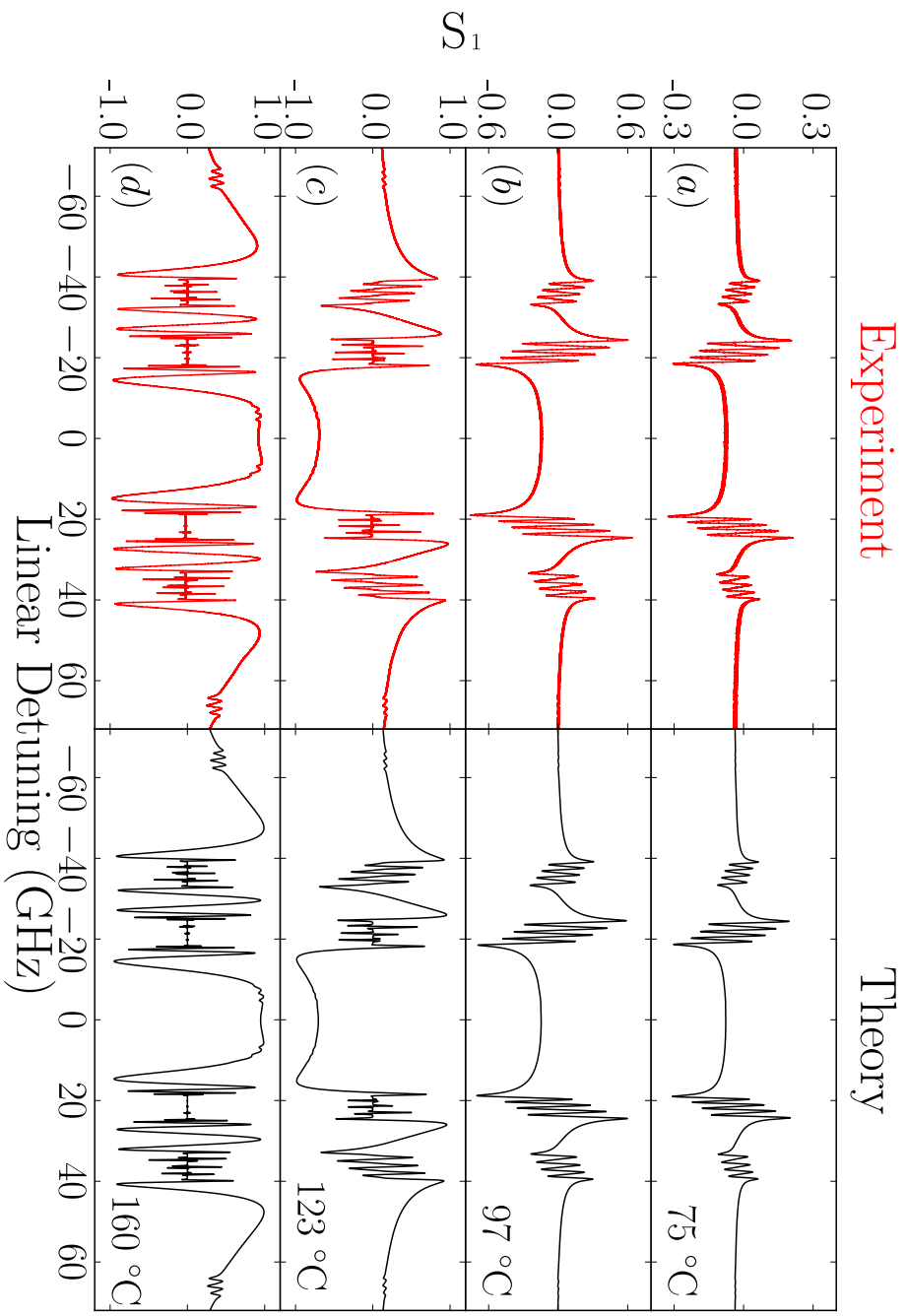

Figure 3.6: Experiment measurement (red) of the temperature evolution for the S_1 parameter of the experiment cell placed in an external magnetic field of $B = 1.54$ T ranging from 75 °C to 160 °C. The corresponding theoretical S_1 parameter fitted using the 'ElecSus' program is shown in black.

3.3 Narrow Scan Results and Discussion

3.3.1 Strong Transitions

In order to obtain a more accurate scan of the S_0 parameter, the wide-scanning DFB laser was replaced by a DL Pro laser. This laser could only scan over a frequency of approximately 15 GHz without mode-hopping, and so was not useful in making measurements of the S_1 Parameter. However, it was able to scan over these frequencies in a matter of milliseconds rather than minutes. This reduced the problems with temperature fluctuations during the scanning time faced when using the DFB laser.

With the shorter scan frequency range, the 'four sets' of S_0 peaks for each polarisation of light seen in figure 3.5 could not all be scanned simultaneously, but individually. From this point onwards, the sets of peaks will be labelled by their approximate linear detunings, ie: $\pm$10 GHz, $\pm$20 GHz, $\pm$40 GHz and $\pm$70 GHz. The peaks at $\pm$20 GHz and $\pm$40 GHz are the 'strong' transitions. The peaks that take place around $\pm$10 GHz and $\pm$70 GHz are referred to as the 'weak' transitions previously discussed in section 2.5.8. The atomic transitions that are the source of each peak are shown more extensively in figure 2.13.

For this thesis, the σ^+ transitions were measured. The linear detunings that these transitions took place at were: -10 GHz, $+40$ GHz, $+20$ GHz, and $+70$ GHz. Two different polarisations were used, one near 100 % light polarised to drive σ^+ transitions, and one near linear polarisation. Firstly, spectra of each set of peaks were measured at a high temperature of approximately $T = 145$ °C. This meant that the atoms had reached the maximum possible absorption of light at this frequency, as shown in part (d) of figure 3.5.

ElecSus was used to determine the two polarisations of these measurements by fitting the polarisation as a variable parameter, along with the temperature and additional broadening. 5 repetitions were taken at each polarisation of both the +20 GHz and +40 GHz transition groups. This left 10 measurements of each polarisation. From these measurements, the polarisations were calculated to be 35.61 ± 0.02 % and 4.49 ± 0.01 % light polarised to drive σ^-

transitions. These polarisations are given as a percentage of σ^- rather than σ^+ in order to match the ElecSus program.

In order to measure maximum absorption coefficients, a lower temperature was required. The temperature was set to be approximately $T = 85$ °C, so that the atoms would not be nearing the maximum possible absorption, but were still hot enough to maximise the SNR.

Figure 3.7 shows the spectrum corresponding to the +40 GHz peaks at the 2 different polarisations, where the top and bottom graphs respectively have 35.51 ± 0.02 % and 4.49 ± 0.01 % light polarised to drive σ^- transitions. From this measurement, the maximum absorption coefficient of each of the 4 peaks could be calculated. This was repeated 5 times for both polarisations, and the weighted mean values and the corresponding uncertainty of each peak are shown in table 3.1 as the top four rows. The weighted mean is discussed in Appendix A as equations A.5 and A.6.

Figure 3.8 shows the corresponding spectrum for the +20 GHz transitions, where the top and bottom graphs show the data with 35.51 ± 0.02 % and 4.49 ± 0.01 % light polarised to drive σ^- transitions respectively. These were measured twice, with the mean values of each maximum absorption at both polarisations shown in the bottom four rows of table 3.1.

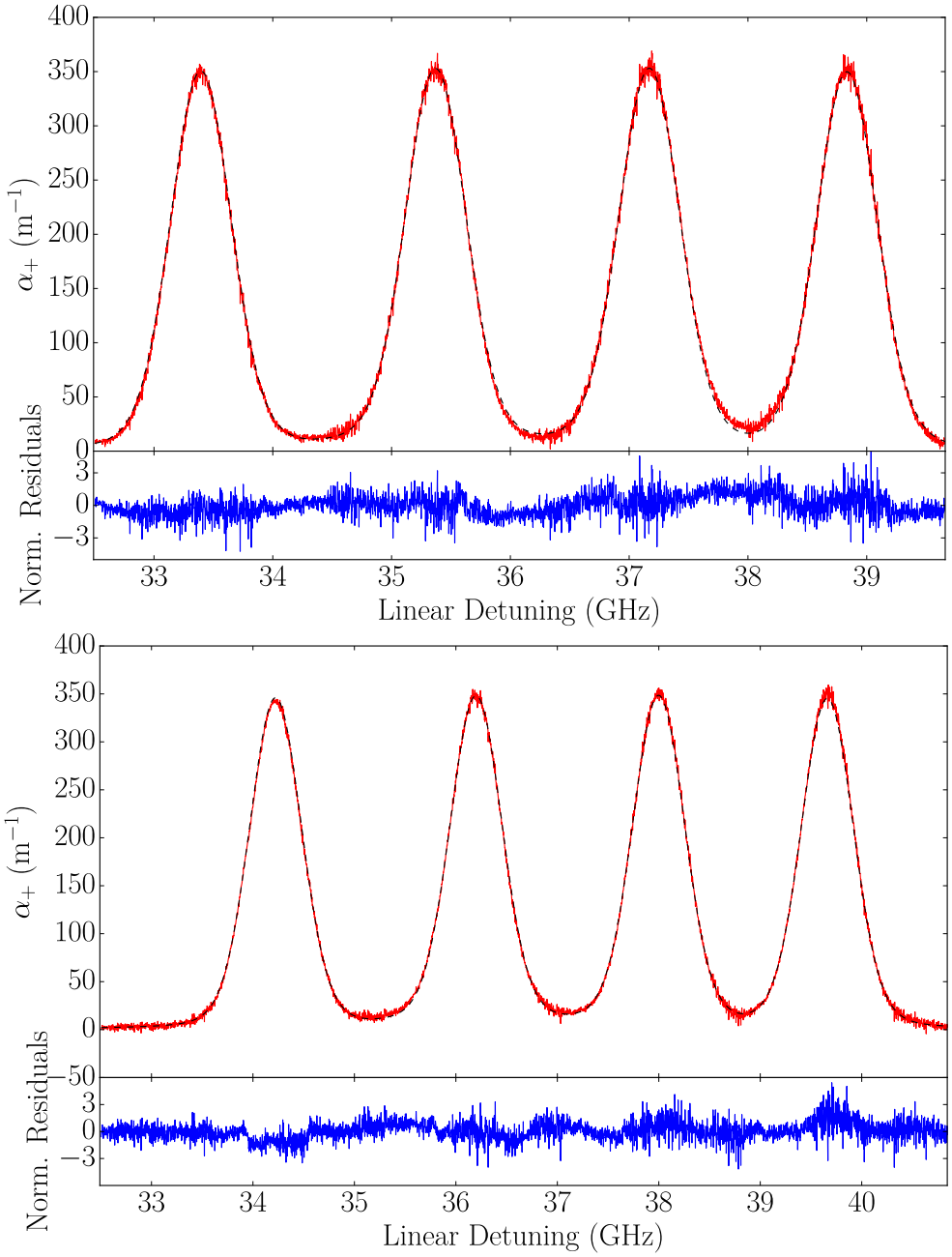

Figure 3.7: Experiment measurement (red) of the absorption coefficient α in units of m^{-1} for the +40 GHz transitions. The theoretical values of α are shown in black, with fitted variables of $T = 84.28 \pm 0.01$ °C (top) and 84.12 ± 0.01 °C (bottom), additional broadening of 83.17 ± 0.02 MHz (top) and 85.02 ± 0.09 MHz (bottom), with assumed polarisation 36.61 ± 0.02 % (top) and 4.49 ± 0.01 % (bottom) light polarised to drive σ^- transitions. Underneath each graph are the normalised residuals using the root mean square (RMS) error equation A.4 as the uncertainty.

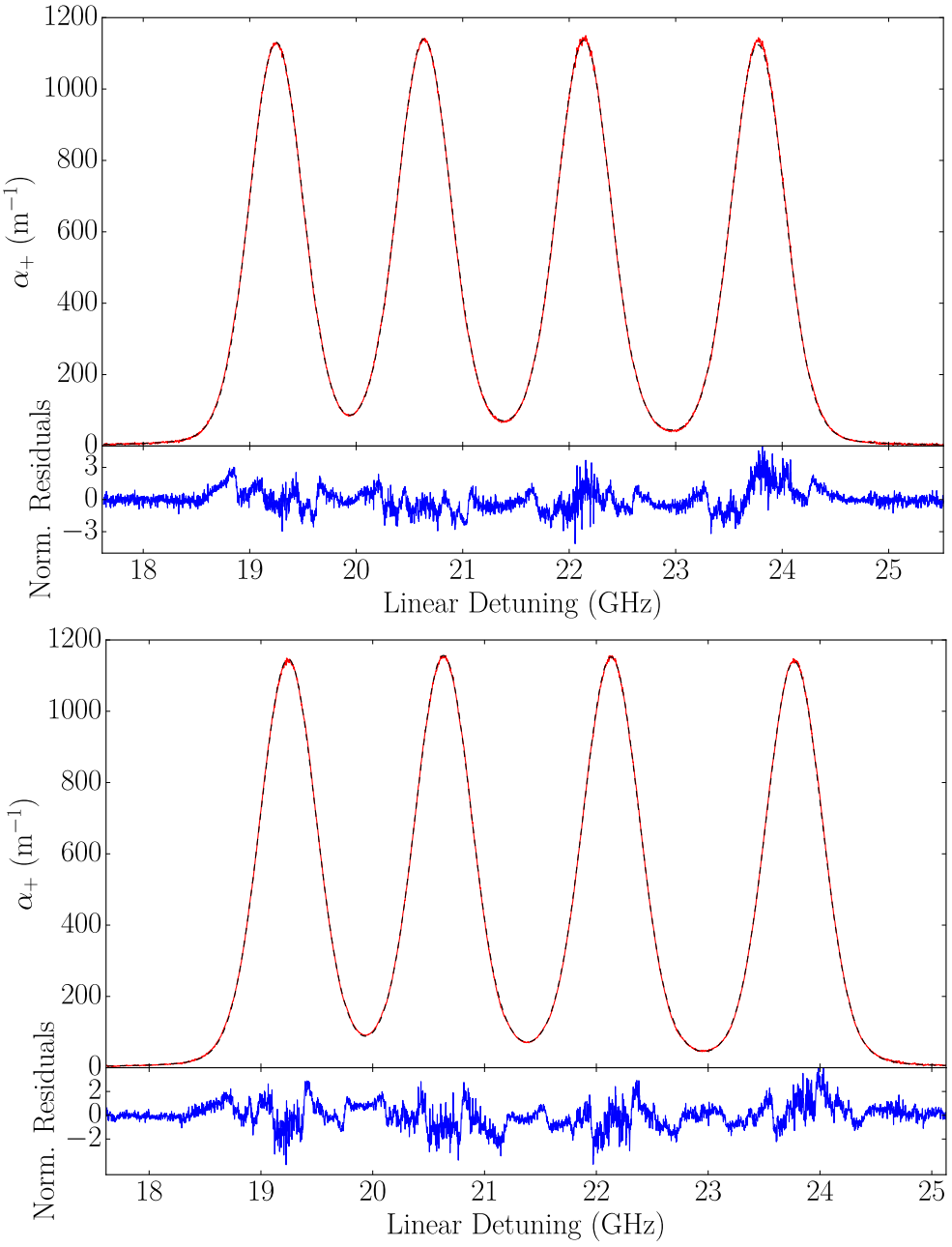

Figure 3.8: Experiment measurement (red) of the absorption coefficient α in units of m^{-1} for the +20 GHz transitions. The theoretical values of α are shown in black, with fitted variables of $T = 84.69 \pm 0.01$ °C (top) and 84.90 ± 0.01 °C (bottom), additional broadening of 57.30 ± 0.04 MHz (top) and 57.86 ± 0.03 MHz (bottom), with assumed polarisation 36.61 ± 0.02 % (top) and 4.49 ± 0.01 % (bottom) light polarised to drive σ^- transitions. Underneath each graph are the normalised residuals using the root mean square (RMS) error equation A.4 as the uncertainty.

Table 3.1: Weighted mean of maximum absorption coefficients of atomic σ^+ transitions at two different polarisations of light polarised to drive σ^- transitions.

	σ^- Polarisation (%)	
	4.49 ± 0.01	35.61 ± 0.02
σ^+ Transition	Absorption Coefficient α (m^{-1})	
$m_J = -\frac{1}{2} \rightarrow m'_J = +\frac{1}{2}$, $m_I = -\frac{3}{2}$	344 ± 5	349 ± 4
$m_J = -\frac{1}{2} \rightarrow m'_J = +\frac{1}{2}$, $m_I = -\frac{1}{2}$	346 ± 3	353 ± 1
$m_J = -\frac{1}{2} \rightarrow m'_J = +\frac{1}{2}$, $m_I = +\frac{1}{2}$	351 ± 2	357 ± 1
$m_J = -\frac{1}{2} \rightarrow m'_J = +\frac{1}{2}$, $m_I = +\frac{3}{2}$	347 ± 1	355 ± 8
$m_J = +\frac{1}{2} \rightarrow m'_J = +\frac{3}{2}$, $m_I = +\frac{3}{2}$	1145 ± 8	1126 ± 8
$m_J = +\frac{1}{2} \rightarrow m'_J = +\frac{3}{2}$, $m_I = +\frac{1}{2}$	1153 ± 6	1133 ± 5
$m_J = +\frac{1}{2} \rightarrow m'_J = +\frac{3}{2}$, $m_I = -\frac{1}{2}$	1158 ± 4	1138 ± 6
$m_J = +\frac{1}{2} \rightarrow m'_J = +\frac{3}{2}$, $m_I = -\frac{3}{2}$	1144 ± 3	1133 ± 4

The difference between the two sets of absorption coefficients at near 4.49 ± 0.01 % and 35.62 ± 0.02 % light polarised to drive σ^- transitions is not negligible. However, theoretically the transition strength has no dependency on the polarisation of the light. This is explained by the fact that the separate measurements did not take place at exactly the same temperature, as they took place within a few minutes of each other. Measurement showed that a temperature change of approximately 1 °C could change the maximum absorption coefficient of the $m_J = -\frac{1}{2} \rightarrow m'_J = +\frac{1}{2}$ transitions by approximately 80 m^{-1}, roughly equal to 7 % of 1150 m^{-1}. The maximum temperature differences of the different polarisation measurements shown in table 3.1 was calculated by the ElecSus fit to be up to 1 °C. This seems to account for the differences in the absorption coefficients observed between the different polarisations of light.

For the $m_J = -\frac{1}{2} \rightarrow m'_J = +\frac{1}{2}$ transitions, the Clebsch-Gordon coefficient can be calculated to be $\sqrt{\frac{1}{3}}$, while for the $m_J = +\frac{1}{2} \rightarrow m'_J = +\frac{3}{2}$ transitions the Clebsch-Gordon coefficient is 1. Their transition strengths are proportional to the Clebsch-Gordon coefficient squared. We would therefore expect the ratio between the maximum absorption coefficients with the same m_I values to be exactly 3. The ratios measured are shown in table 3.2.

For example, using table 3.1, the bottom row $m_J = +\frac{1}{2} \rightarrow m'_J = +\frac{3}{2}$, $m_I = -\frac{3}{2}$ transition's maximum absorption coefficient would be divided by the maximum absorption coefficient of the top row $m_J = -\frac{1}{2} \rightarrow m'_J = +\frac{1}{2}$, $m_I = -\frac{3}{2}$ transition. This particular ratio is shown in the top row of table 3.2.

Table 3.2: Ratios of the weighted mean of maximum absorption coefficients of atomic σ^+ transitions at two different polarisations of light polarised to drive σ^- transitions.

	σ^- Polarisation (%)	
	4.49 ± 0.01	35.61 ± 0.02
m_I	Absorption Coefficient Ratio	
$-\frac{3}{2}$	3.33 ± 0.04	3.25 ± 0.04
$-\frac{1}{2}$	3.35 ± 0.015	3.23 ± 0.02
$+\frac{1}{2}$	3.28 ± 0.02	3.17 ± 0.02
$+\frac{3}{2}$	3.29 ± 0.07	3.17 ± 0.07

Although the ratios were theoretically expected to be exactly 3, they are all at least 5% above this value, and are as much as almost 12% above their expected value. Furthermore, all of the ratios measured with 4.49 ± 0.01 % light polarised to drive σ^- transitions are further from the expected value of 3 than the ratios using the 35.61 ± 0.02 % polarised light. There also appears to be a trend where the ratios with negative m_I values are higher than the ratios with positive m_I values, although they are within $2\times$ their errors of each other so this may not be significant.

Temperature fluctuations between the two measurements was most likely the dominant source of the discrepancy between the theoretical prediction of exactly 3 and the values shown in table 3.2. A simple calculation shows that a temperature difference of only 1 ° C would lead to a ratio of approx-

imately $\frac{1150+80}{350} = 3.51$. As all the measurements were taken within 1 ° C, and the +20 GHz transitions were systematically larger than the +40 GHz transitions, this would account for the variation from theory.

If any future measurements of this ratio were to be taken, it would be important to ensure temperature stability as even a fluctuation of less than 0.3 % of the temperature in Kelvin can significantly affect the absorption coefficient and therefore the ratio of the two transitions by nearly 20 %.

3.3.2 Weak Transitions

The narrow-band laser was also used to measure the weak σ^+ transitions occurring at −10 GHz and +70 GHz. A much higher temperature was used for these measurements in order to maximise the SNR, as the transitions are significantly weaker than the strong transitions, absorbing much less light. The temperature was measured to be approximately 145 °C, although fitting with ElecSus showed that the temperature was actually approximately 156 °C.

As shown by figure 3.9, the +70 GHz group of transition again has an excellent fit. The residuals are normalised assuming an uncertainty of measurement equal to the standard deviation of the noise in the wings, and the reduced $\chi^2_{\text{red}} = 4.8,\ 4.5$ (found by using the techniques explained in [77]) for the near-linear and near-100% polarisations respectively. As this uncertainty does not include the uncertainty involved in the process of normalising the $x-$ and $y-$axes, the χ^2_{red} values are above 1. 5 repetitions of this fit were conducted, and the resulting average values of temperature and additional broadening were assumed for the final σ^+ group of transitions that occur at −10 GHz. The fit was found by letting only the Linear-Detuning variable float using the program.

This final fit for both polarisations of light is shown in figure 3.10. The fit is visibly much less accurate. Again, the uncertainty was assumed to be equal to the standard deviation of the noise in the wings. Although this again likely underestimates the uncertainty, this is not the dominant source of error in this fit. The $\chi^2_{\text{red}} = 1400,\ 260$ values for the near-linear and near-100 % polarisations are both much larger than 1 in comparison to the values of the

fit for figure 3.9. Furthermore, the near-linear fit has a significantly worse fit than the near-100 % light polarised to drive σ^+ transitions.

The presence of an extra, smaller peak at a linear detuning range of up to 1.5 GHz for both polarisations is not seen in the ElecSus program's model, and each of the 3 expected weak peaks have significantly higher absorption coefficients than expected. Although smaller than the expected weak transition's peaks, the 'extra peak' is large enough to be considered significant in comparison to the expected peaks.

The peak occurs at exactly the expected linear-detuning for a strong π transition. Such a π transition would only take place for a laser beam's electric field component that is parallel to the magnetic field. As this π transition has an absorption coefficient that is larger than that of the weak σ^+ transitions, only a small spatial component of the laser beam's electric field would need to be parallel to the magnetic field. Considering the orientation of the setup, it is possible that the laser beam was incident to the atoms at a slight angle from the perpendicular in relation to the magnetic field.

The π transition would also take place in a group of 4, with the other 3 peaks occurring at approximately the same frequency that the 3 weak σ^+ transitions occur at, which could explain the extra absorption seen in the 3 weak σ^- transitions. The weak π transitions do not make a significant contribution to the strong $\sigma^\pm$ transitions and can therefore be ignored. π transitions would also explain why the fit is much worse in the near-linear polarisation than in the near-100 % polarisation. While the absorption of the σ^+ transitions depends on the polarisation, the absorption of the π transition does not. When converting to absorption coefficient from transmission, the strong π transitions will be closer in size to the weak σ^+ transitions in the near-linear polarisation, and will therefore appear larger as absorption coefficient for the near-linear than the near-100% polarisation.

However, ElecSus does not currently have an option to change the possible input angle of the laser beam to account for π transitions. This would be a significant improvement to the model. Furthermore, the existence of these peaks could also be useful in order to check alignment as the peaks will not appear when the laser's $\underline{\mathbf{k}}$ is exactly parallel to the direction of $\underline{\mathbf{B}}$.

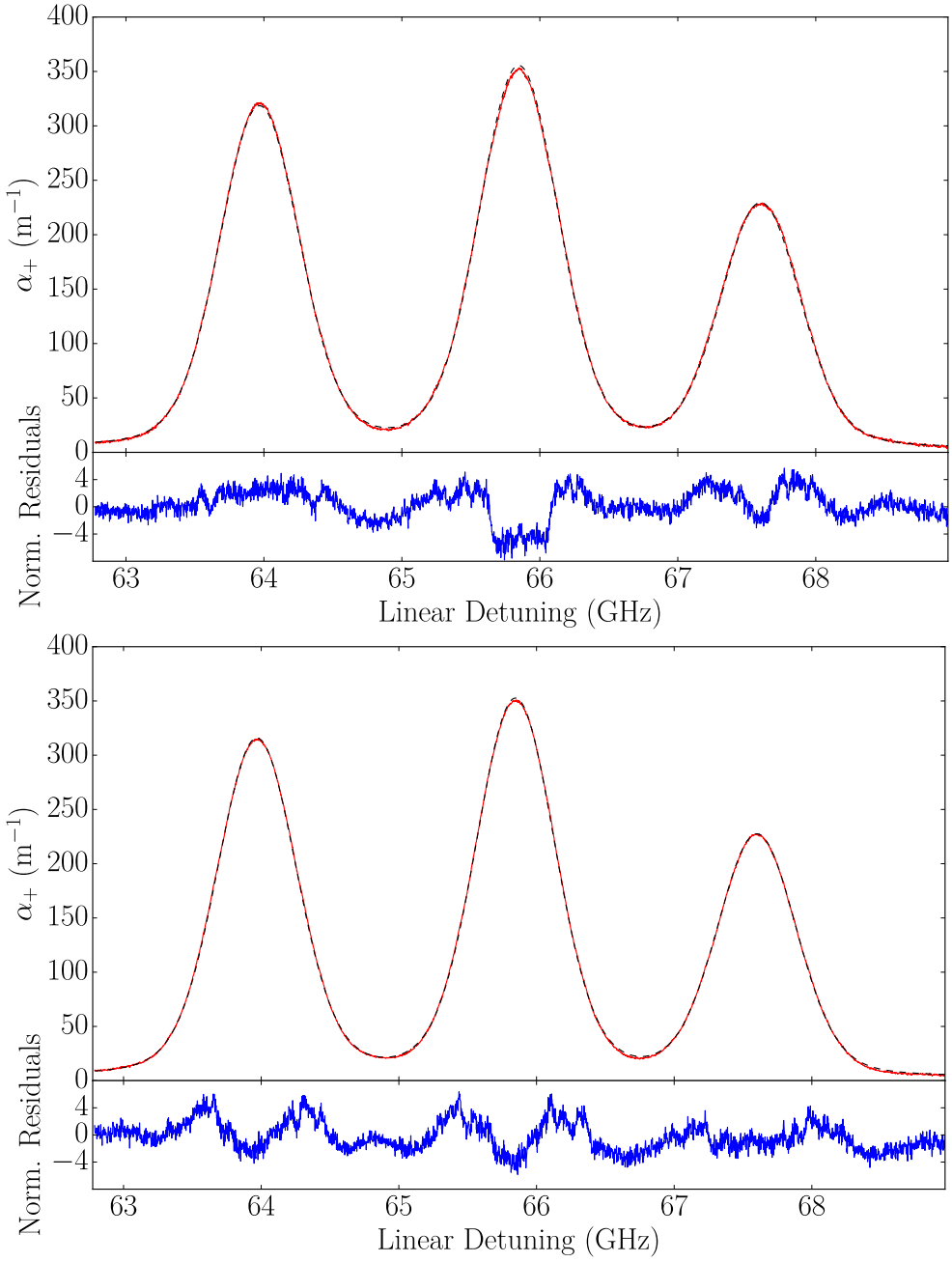

Figure 3.9: Experiment measurement (red) of the absorption coefficient α in units of m^{-1} for the +70 GHz transitions. The theoretical values of α are shown in black, with fitted variables of $T = 156.46 \pm 0.01$ °C (top) and 156.15 ± 0.01 °C (bottom), additional broadening of 109.30 ± 0.06 MHz (top) and 104.37 ± 0.04 MHz (bottom), with assumed polarisation 36.61 ± 0.02 % (top) and 4.49 ± 0.01 % (bottom) light polarised to drive σ^- transitions. Underneath each graph are the normalised residuals using the amplitude of the noise as the uncertainty, giving $\chi^2_{\text{red}} = 4.8$ and 4.5 for the top and bottom respectively.

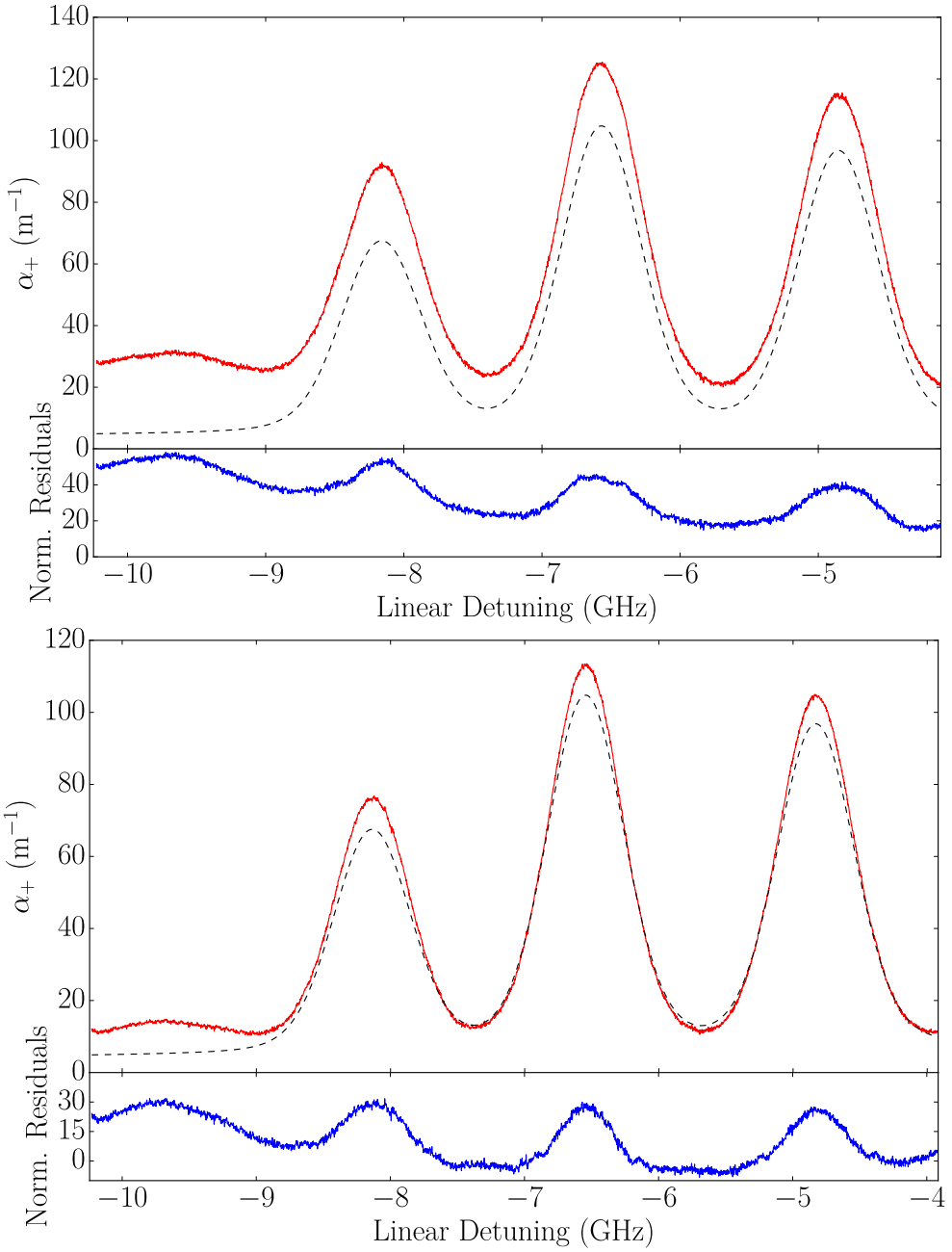

Figure 3.10: Experiment measurement (red) of the absorption coefficient α in units of m^{-1} for the -10 GHz transitions. The theoretical values of α are shown in black, with the same variables as in figure 3.9 with assumed polarisation 36.61 ± 0.02 % (top) and 4.49 ± 0.01 % (bottom) light polarised to drive σ^- transitions. Underneath each graph are the normalised residuals using the amplitude of the noise as the uncertainty, giving $\chi^2_{\mathrm{red}} = 1400$ and 260 for the top and bottom respectively. The discrepancy between theory and experiment is a manifestation of the π transitions, see text.

Chapter 4

Power Evolution of the Absorption Coefficient

The theory underpinning ElecSus assumes that the atom-light interactions take place in the 'weak-probe regime'. Previous investigations have experimentally found the bounds of intensity at which this regime takes place to be several orders of magnitude less than the saturation intensity for a particular transition [39, 67]. However, an investigation of the these bounds has never previously been undertaken for Rubidium atoms in the hyperfine Paschen-Back regime, or for beams with waists smaller than ≈ 0.5 mm. This chapter aims to experimentally evaluate whether the bounds of this regime change under these conditions.

In addition, the power evolution of absorption with a changing laser intensity has not been experimentally studied for laser intensities much larger than the saturation intensity of the transition. In this chapter this is undertaken, and the claim that the line-centre absorption of the Voigt profile follows the inhomogeneous relationship as the intensity of the laser beam is changed is experimentally investigated.

4.1 Limits of the weak-probe regime with no external magnetic field

4.1.1 Previous Work

The limits of the weak-probe regime for Rubidium has previously been investigated by researchers, including Sherlock and Hughes in 2009 [39]. The investigation took place without an external magnetic field being applied, and so the ground state of the Rubidium atoms have 2 hyperfine non-degenerate ground states, as well as the magnetic degenerate sub-levels, as shown by figure 2.4. Therefore optical pumping could take place from a resonant ground state to the dark, non-degenerate hyperfine state. This process is called hyperfine pumping.

The paper investigated the weak-probe regime for 3 different beam sizes, with widths given by their FWHMs as 0.3, 1.7 and 2.7 mm. The range of intensities spanned from $I_0/I_{sat} \approx 10^{-5}$ to just above 10^0. Three main conclusions were found. Firstly, the beam width had a significant effect on the line-centre absorption, due to the difference in time-of-flight, but the extent of which was beyond the scope of the investigation. Secondly, for the widest beam, ensuring the atom-light interaction was taking place in the weak-probe regime meant that the intensity necessary was $I_0/I_{sat} \leq 10^{-3}$. The final conclusion was that the extent of the hyperfine pumping is influenced by whether the individual degenerate transitions are open or closed. Therefore, in a composite transition of all open transitions, the effect of the hyperfine pumping would be more pronounced than in a composite transition of two open transitions, and one closed transition.

Another example of a weak-probe investigation of Rubidium is given as part of Siddons *et. al.*'s, 2008 paper titled 'Absolute absorption on rubidium D lines: comparison between theory and experiment' [53]. The investigation was conducted for a beam width of 2 mm, though it is not stated whether this is a FWHM value or another measurement of width, i.e.: $1/e^2$ width. Assuming it is a measure of FWHM, it is a similar size to the values used in Sherlock and Hughes (2009).

The Gaussian relationship described in equation 2.45 does not successfully fit the data, and was amended by the authors to include a fitting factor β as

$$\frac{1}{\sqrt{1+\beta(\mathrm{I}/\mathrm{I}_{\mathrm{sat}})}}, \tag{4.1}$$

to fit the data. However, this was done as a guide to the eye only.

The laser intensity was varied between $\mathrm{I}/\mathrm{I}_{\mathrm{sat}} \approx 0.001$ and 1. The weak-probe regime is concluded to be ensured for all four transitions at $\mathrm{I}/\mathrm{I}_{\mathrm{sat}} \approx 10^{-3}$.

4.1.2 Beam Width

The beam width w has previously been shown to be an important factor when considering the weak-probe regime's limits, not only for the line-centre absorption [39] but also for the line shape [81]. The previous investigations have mostly defined w as the FWHM, and typical values are in the order of a few millimeters.

The cell used in this investigation had a width of 1 mm, enclosed in a cell casing of 0.75 mm width. Therefore w could not be in the same range of values as previously investigated, as much of the beam would have been blocked by the cell's casing. A cross-sectional view is shown in figure 4.1, and the dotted circle inside the cell shows that radius of the beam $r < 0.5$ mm.

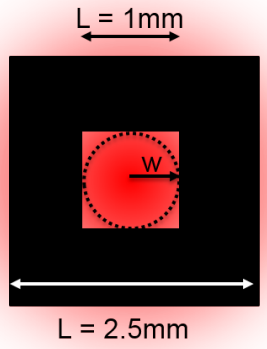

Figure 4.1: Cross-section of cell casing (black square) and laser beam (red). The dotted circle shows the laser beam's radius inside the casing.

In this investigation, the $1/e^2$ radius is defined as the beam width measurement w, rather than the FWHM as used in other literature. The difference between the $2w = 1/e^2$ diameter and the FWHM of a Gaussian distribution of laser intensity is given by the relationship

$$w^2 = \frac{\text{FWHM}^2}{2\ln 2}. \tag{4.2}$$

A CCD camera and beam profiling software was used to measure w at the focus of the beam. It was measured as approximately 50 μm. This value is approximately 10 times smaller than the smallest beam width used in Sherlock (2009).

The cell was displaced from the focus of the beam, so that w could be maximised. This was limited by the width of the cell itself as previously discussed. The CCD camera was placed behind the cell and used to image the cell at various distances from the focus, ensuring that a normal distribution occurred within the edges of the cell. This was observed by the lack of sharp, square edges in the image from the cell casing. Screenshots of the beam profiling software used, including images of the beam transmitted through the cell, are given in Appendix C in figures C.1 and C.2.

Imaging the beam also showed that the cell was partially blocked by the cell casing, such that the horizontal axis of the cell was much larger than the vertical. In order to keep the cell in place, it was not possible to reduce this block any more than is shown by the figures. This meant that the maximum radius of the beam would have to be even less than 0.5 mm, the lowest beam width used by Sherlock (2009).

The maximum beam width that could be used while still ensuring a nearly normal distribution within the blocked cell was found to be $w_x = 230 \pm 4$ μm, $w_y = 268 \pm 6$ μm, where w_x and w_y are the widths in the x and y axes respectively. The mean w value is approximately 250 μm.

The probability distribution of atomic time-of-flight $H(\text{t})$ of Rubidium atoms across the beam, where t is the time-of-flight, can be given as a closed form equation and has previously been derived [70]. In figure 4.2, $H(\text{t})$ is plotted for the 3 beam widths used in Sherlock (2009), given as $1/e^2$ radii, and for $w = 250$ μm. There is clearly a large dependence on beam width.

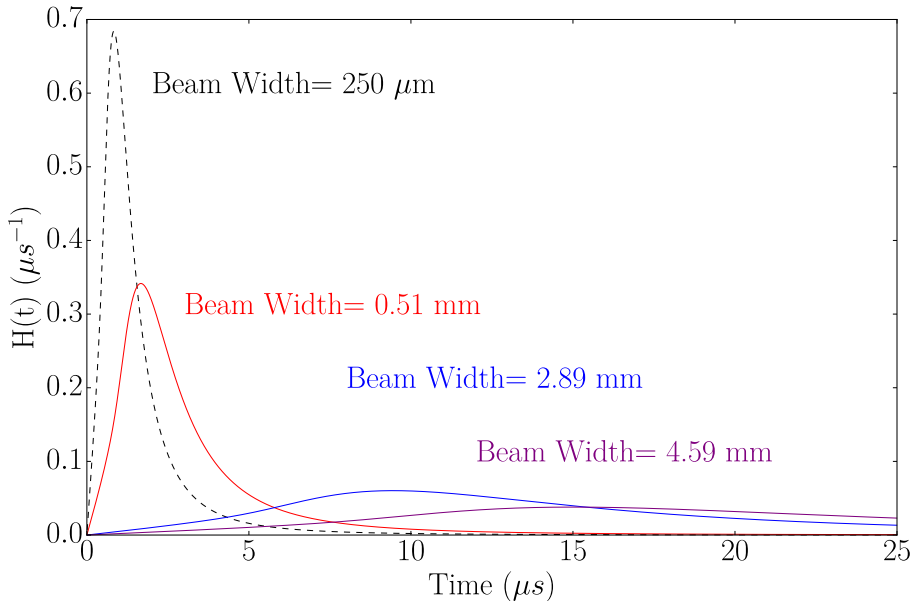

Figure 4.2: Probability distribution $H(t)$ of time-of-flight of ^{87}Rb atoms traversing a beam of various widths w. The distribution for the beam width used in this experiment $w \approx 250$ μm is shown as the black dashed line. Temperature assumed to be $T = 300$ K.

For the D2 line of ^{87}Rubidium, the lifetime of the transition is $\tau = 26.24(4)$ ns [56]. Previously, the time-of-flight of the atoms is assumed to be much larger than the average lifetime of the transition, such that the number atoms that decay before hyperfine pumping to the dark state can take place is negligible. By looking at the percentage of the area of $H(t)$ before $t = \tau$, it is possible to assess whether this assumption is correct.

The definite integral of $H(t)$ between 0 and τ, as a percentage of the total area under the curves, is equal to 6.4×10^{-5} %, 1.7×10^{-4} %, 5.4×10^{-3} % and 2.2×10^{-2} % for $w = 4.59$ mm, 2.89 mm, 0.51 mm, 250 μm respectively. This shows that reducing w by a factor of ≈ 20 increases the probability of an atom having a time-of-flight smaller than τ by a factor of ≈ 350.

This shows that, for the thin beams used in this work, there is a higher probability that hyperfine pumping will not occur for a given beam intensity, and conversely, for wide beams, there is more time for hyperfine pumping to occur during an atom's transit. It is therefore predicted that the weak-probe regime can be obtained with higher intensities than in previous work.

4.1.3 Results and Discussion

The intensity evolution for the experimental cell without an external magnetic field is shown in figure 4.3, for laser powers ranging from a few nW, to $\approx$ 155 μW. The power of the laser was measured using an 'Ophir Nova II' power meter, placed before the cell, and varied using 'Thorlabs' neutral density filters.

Efforts were made to reduce the background lighting as much as possible during measurement, including shielding the power meter and turning off room lights. In addition, the laser was turned off and the background light measured for each power measurement so that it could be subtracted from the power measurement.

In figure 4.3, the spectra are colour coded to show power evolution of the transmission. The lowest intensity spectrum is shown as a dark blue, which corresponds to the spectrum with the highest absorption peak. As the intensity is increased the spectra are shown as progressively more green until the highest intensity spectrum is shown as a bright green. This is the spectrum with the lowest amount of absorption.

The theoretical spectrum is shown as a black dashed line. This spectrum was calculated by ElecSus using the fitted parameters of the 3rd smallest intensity spectrum.

The lowest intensity spectrum has a low SNR in comparison to the higher intensity spectra. There are 15 transmission spectra plotted, but several spectra overlap with the lowest spectrum, so only $\approx$ 7 can be easily observed on the graph. The overlapping spectra have a much higher SNR than the spectra with the lowest intensity, as their intensities are up to 2 or 3 orders of magnitude larger than the lowest intensity.

In addition to the 2 large ^{87}Rb peaks, separated by 6.8 GHz as expected from figure 2.3, two smaller peaks are also seen from the 1 % of ^{85}Rb present in the experimental cell. The uncertainty of these measurements were considered too small to calculate their absorption coefficients accurately.

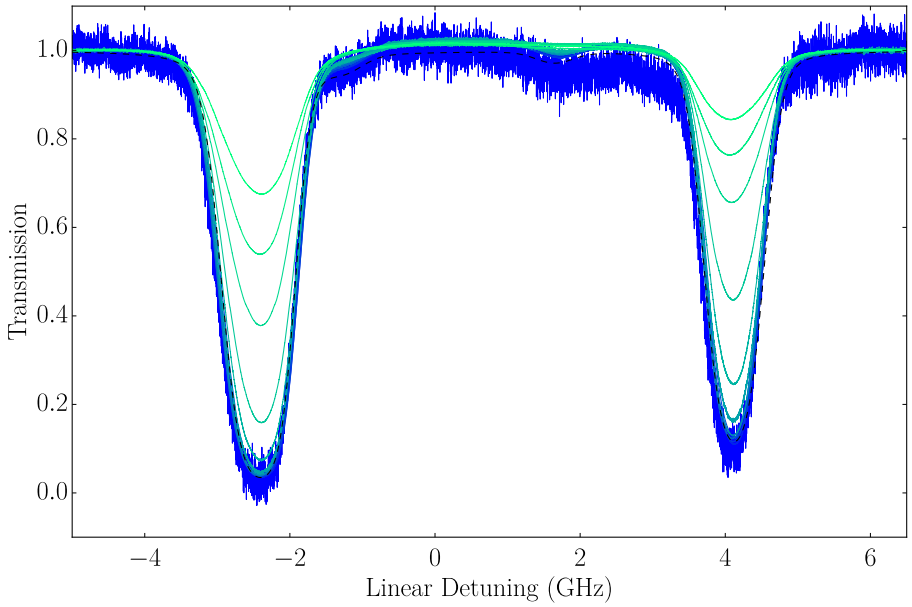

Figure 4.3: 15 experimental transmission spectra through the experimental cell with no external magnetic field applied, showing the evolution of changing laser beam intensity against linear detuning. As the beam becomes more intense, a higher SNR is achieved and less absorption takes place shown by the colour change from dark blue to light green. The theoretical spectrum is shown as the black dashed line, with fitted variables from ElecSus of T = 85.01 °C and additional broadening of 56.79 MHz.

Using the relationships $S_0 = e^{-\alpha_{\pm} L}$ or $I = I_0 e^{-\alpha_{\pm} L}$, the absorption coefficient can be calculated from the Transmission. The corresponding maximum absorption coefficients for the data shown in figure 4.3 is plotted against I/I_{sat} in figure 4.4. Note the logarithmic x-axis. It is evident that there is a dramatic reduction in the absorption coefficient for intensities $\geq I_{sat}$. Also plotted as a black dashed lined is the theoretical maximum absorption coefficient assuming the weak-probe regime. This theory was calculated by fitting to the 3rd smallest intensity spectrum using ElecSus.

Two curves have been fitted to the data. The solid curve follows the inhomogeneous relationship discussed previously, with a fitting factors a_i and b_i as included in [67], given by

$$\alpha = a_i \times \frac{1}{\sqrt{1 + b_i(I/I_{sat})}}. \tag{4.3}$$

The dashed curve follows the form of the homogeneous relationship given by

equation 2.44, including fitting factors a_h and b_h, as

$$\alpha = a_\mathrm{h} \times \frac{(\Gamma/2)}{(\Gamma/2)^2 + b_\mathrm{h}(\mathrm{I}/\mathrm{I}_\mathrm{sat})}, \tag{4.4}$$

where Γ is the natural linewidth (FWHM), and is equal to $2\pi \times 6.0666(18)$ MHz for the D2 line of ^{87}Rb.

The inhomogeneous relationship that has previously been used to describe the evolution of the absorption coefficient with changing intensity has χ^2_red values of 49 and 70 for the $F = 1 \rightarrow F'$ and $F = 2 \rightarrow F'$ transitions respectively, while the homogeneous relationship has χ^2_red values of 2.6 and 2.4 respectively (all to 2 s.f.). The error values for the χ^2_red calculations were found by measuring the difference between the average value in one of the wings (Linear Detuning < -4.4 GHz) of the theoretical spectrum from ElecSus and the measured spectrum. For the lowest intensity measurement, the standard deviation of the noise in the wings was instead used as the error value as it is much more dominant.

A visual inspection of the data, and the χ^2 analysis, both clearly indicate that the homogeneous relationship has a much better for to the data than the inhomogeneous fit. It is not currently understood why this is the case as the Doppler broadening is two orders to magnitude greater than the homogeneous width. However, a detailed explanation of this is well beyond the scope of this experimental thesis. Some research is known to be ongoing at Durham University into whether this can be explained with theory [82].

Very thin beams are useful in many experiments, such as quantum memories with atoms confined to fibres and atomic vapours in which narrow optical fibres confine the light [83–86]. In addition, the data shows that the weak-probe regime can be reached at $\mathrm{I}_0/\mathrm{I}_\mathrm{sat}$ values of up to 10^{-1} for beams of this size. This is contrast with Sherlock (2009) and Siddons (2008), which both showed that values of at maximum $\mathrm{I}_0/\mathrm{I}_\mathrm{sat} < 10^{-3}$ was required to be in the weak-probe regime for beam widths in the range of a few millimeters. Unlike in Siddons (2008), the two peaks do not seem to reach the weak-probe regime at a significantly different intensity.

Being able to ensure the weak-probe up to 2 orders of magnitude higher intensities than previously thought is extremely useful for future spectroscopy using Rubidium, and potentially other alkali-metal atoms. Being able to in-

crease the SNR while staying in the weak-probe regime means that the atoms' absorption coefficient along with other measurements can be calculated much more precisely than previously thought.

This is especially clear in figure 4.3, where the the low SNR of the lowest intensity spectrum overlaps with multiple other spectra. Measuring the value of the absorption coefficients from this spectrum will have a large uncertainty, as is seen by the error bar of the corresponding value in 4.4 in comparison to the error bars of all the other measurements. The uncertainty of measurement is therefore reduced by using a higher intensity measurement.

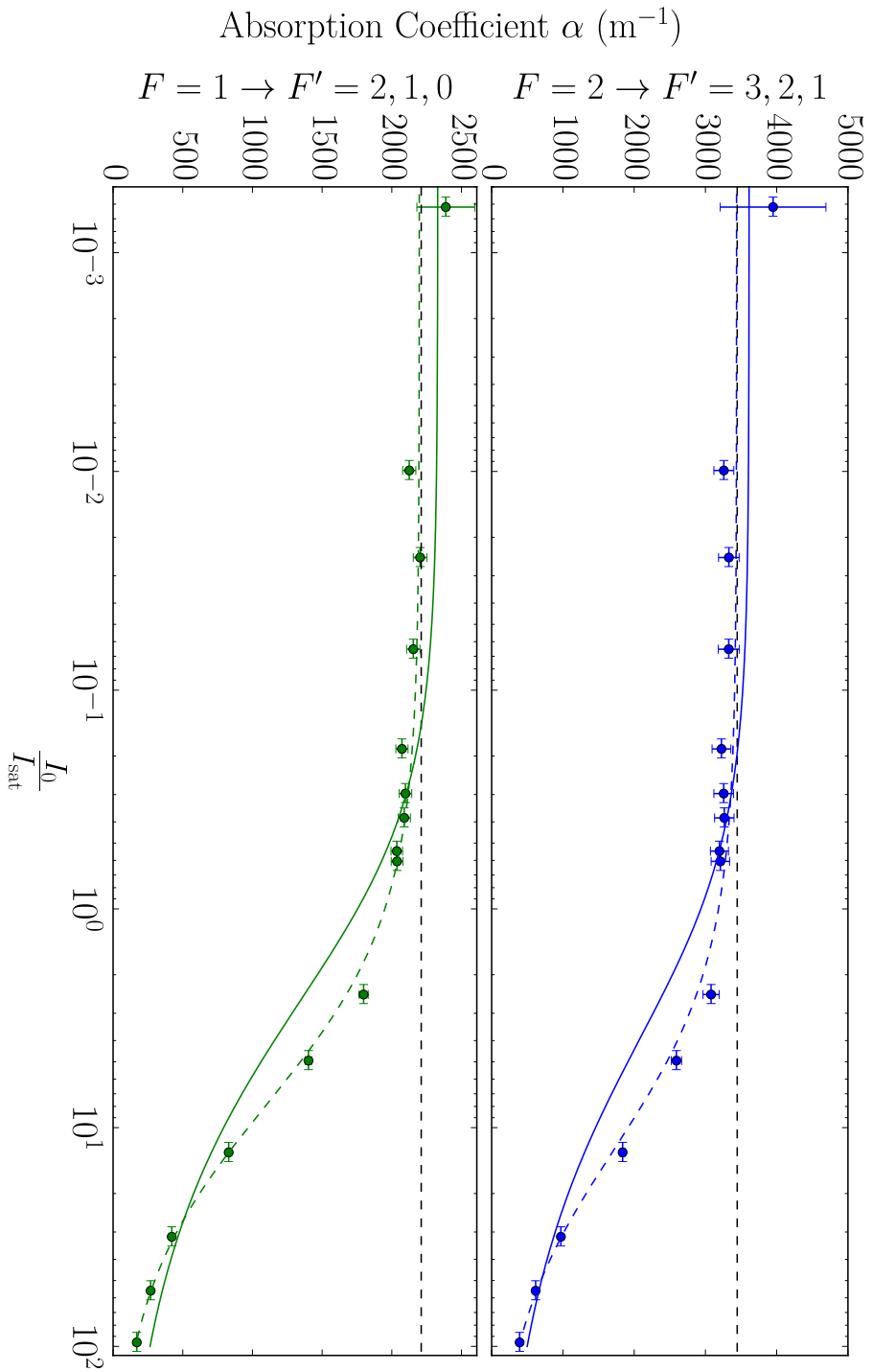

Figure 4.4: Absorption Coefficient α plotted against I_0/I_{sat} for the two ^{87}Rb transitions shown in figure 4.3, assuming $I_{sat} \approx 1.67$ mW/cm^2. The theoretical α value from ElecSus, fitted from the 3rd smallest intensity spectrum, is shown as a black dashed line. The inhomogeneous fit from equation 2.45 is shown as the solid curves, while the homogeneous fit from equation 2.44 is shown as the dashed curves.

4.2 Limits of the weak-probe regime in the hyperfine Paschen-Back regime

The limits of the weak-probe regime have not previously been investigated for Rubidium atoms when a large magnetic field has been applied. It is possible that in the hyperfine Paschen-Back regime, the hyperfine splitting is large enough that the power evolution of the absorption coefficient is significantly changed.

This section will investigate this possibility by comparing the power evolution and the limits of the weak-probe regime in a parallel magnetic field (Faraday Geometry) of 1.54 T with the evolution and weak-probe regime limits without an external magnetic field considered in section 4.1.

4.2.1 Effect of magnetic field on hyperfine pumping

Previously, the transitions measured were made up of 3 Doppler-broadened, non-degenerate transitions. Each of these transitions were made up of multiple degenerate sub-levels from their magnetic quantum numbers. Of all of these states, only 2 were closed transitions, which meant that hyperfine pumping to a dark state could take place for almost all the transitions. The application of the external magnetic field means that the hyperfine sub-levels of both the ground and excited state are no longer degenerate.

At a magnetic field of $B = 1.54$ T, the system is within the hyperfine Paschen-Back regime, and there are therefore 8 non-degenerate hyperfine ground levels (see figure 2.4), and 16 non-degenerate hyperfine excited levels (see figure 2.5). The separation of the transitions exceeds the Doppler width (see figures 2.12, lower and 2.13) so the absorption coefficients can be measured separately to each other, whereas previously the degenerate hyperfine states meant that only composite transitions could be measured.

Some of the transitions considered in this investigation were the 4 strong σ^- transitions that occur at approximately -20 GHz, which are defined as the $m_J = -1/2 \rightarrow m'_J = -3/2$, $\Delta m_I = 0$ transitions (shown in figures 2.12, lower and 2.13). Each of these transitions are closed which means that hyperfine

pumping to a dark state is forbidden by the selection rules. It would therefore be expected that the weak-probe regime can be reached at a higher intensity than previously shown by Sherlock (2009) or Siddons (2008).

The other group of transitions considered in this investigation was the 4 strong σ^- transitions that occur at approximately -40 GHz, defined as the $m_J = +1/2 \rightarrow m'_J = -1/2$, $\Delta m_I = 0$ transitions (again shown in figures 2.12, lower and 2.13). They are all open transitions as the selection rules mean that spontaneous decay could occur as a π transition to the non-resonant and therefore dark $m_J = -1/2$ state. As optical pumping is allowed, it would be expected that a lower intensity laser would be required to reach the weak-probe regime for these transitions.

However, as the small beam width used has already been shown to make a large difference to the limits of the weak-probe regime, it is possible that the limits will not be changed significantly by the addition of a magnetic field.

4.2.2 Results and Discussion

Power Evolution of the '−20 GHz' peaks

Transmission spectra were measured for the '−20 GHz' set of σ^- peaks. The experimental setup was the same as in the previous section, except the cell was placed inside the magnet as described in chapter 3. The beam size was kept the same as the cell was placed at the same distance from the focus of the beam as previously.

Again the power of the beam was measured, and the average background light levels were subtracted from the measurement. This was converted to intensity, and the saturation intensity $I_{sat} = 1.67$ mW/cm^2 for a two-level atom was again used. Using this value is actually more relevant for this part of the investigation, as the transitions are closed.

15 total laser intensities were used, and for each intensity 5 transmission spectra were measured. For each of the 5 transmission spectra, the resonant absorption coefficient was calculated independently such that uncertainty from the normalisation process of the x- and y- axes could be reduced.

In figure 4.5, one of the five transmission spectra for each laser intensity has been plotted. The spectrum with the lowest laser intensity of 25 ± 8 μW/cm^2 is shown in dark blue, and the colour of each spectrum gets progressively more green until the highest laser intensity (9.2 ± 0.3 W/cm^2) spectrum, which is shown in bright green.

As the laser beam's intensity is reduced, a greater percentage of the light is absorbed until the weak-probe regime is reached. Once the weak-probe regime has been attained, reducing the laser beam intensity no longer increases the absorption peak. Of the 15 spectra, only ≈ 8 are observable from the graph, because of the large amount of noise present in the lowest laser intensity measurement, but also as once in the weak-probe regime the spectra overlap.

The theoretical spectrum is plotted on figure 4.5 as a black dashed line, and was calculated using the 2nd lowest laser intensity transmission measurement, fitted using ElecSus. The fitted parameters of the theoretical spectrum are shown in the caption.

The average values for the 5 experimental measurements of each of the 4 lowest intensity spectra are as follows: the temperature was 93.3 ± 0.3 °C and the additional broadening was 100 $\pm$ 15 MHz. The mean value of the light's polarisation, calculated using the 5 measurements of the lowest intensity spectra, was 41.6 ± 0.4 % light polarised to pump σ^- transitions.

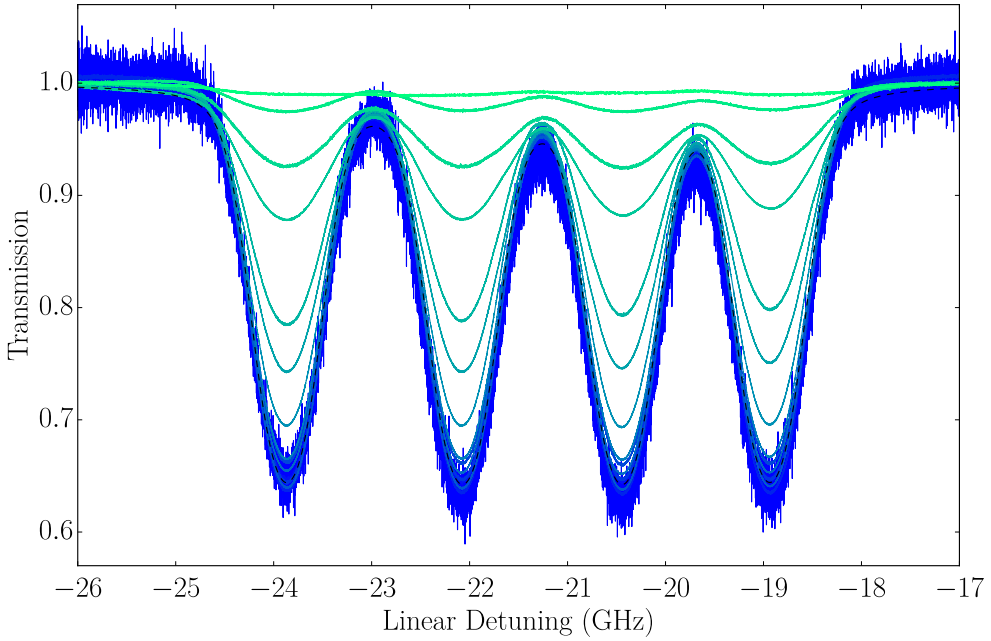

Figure 4.5: Experimental power evolution of transmission against linear detuning spectra with an external magnetic field $B = 1.54$ T applied, for the '−20 GHz' set of σ^- peaks. 1 of 5 measured spectra for each laser intensity is plotted. With increased beam intensity, the SNR increases shown by the colour change from dark blue to light green. The theoretical spectrum is the black dashed line, fitted to just the 2nd smallest intensity spectrum using ElecSus, with fitted variables of $T = 93.13$ °C, additional broadening of 98.4 MHz and 41.33 % light polarised to pump σ^- transitions.

The polarisation of the beam was also important, and therefore the relationship between α_- and transmission S_0 can be defined as

$$\alpha_- = -\frac{1}{L} \ln \left(1 - \frac{1 - S_0}{p} \right), \tag{4.5}$$

where p is the fraction of light polarised to pump σ^- transitions. A small change in polarisation can have a large effect on the absorption coefficient.

The absorption coefficients calculated from the transmission spectra are plotted in figure 4.6. An average value of the independently calculated absorption coefficients for each of the 5 measured transmission spectra is plotted along with each corresponding uncertainty. Error analysis shown in appendix A. In the figure, the theoretical absorption coefficient values are shown as the grey area, with its upper and lower bounds shown as the solid black lines. This was calculated from the mean and standard deviation of the 5 absorption coefficient values for each of the 4 transitions in the 2nd lowest laser intensity spectrum. In the previous data, only one transmission spectrum per intensity value was measured, so the theoretical weak probe value of the Absorption Coefficient was given as a single value, rather than as a range of values.

2 equations are again fit to the data, the inhomogeneous fit given by equation 4.3, and the homogeneous fit given by equation 4.4. In order to quantify how well the equations fit the data, a χ^2 analysis was performed, using the uncertainty in the absorption coefficient measurement as the error. The χ^2_{red} values from the fits shown in figure 4.6 are as follows: the inhomogeneous fit (solid curves) values are $(i) = 130$, $(ii) = 130$, $(iii) = 128$ and $(iv) = 129$; and the homogeneous fit (dashed curves) values are $(i) = 4.50$, $(ii) = 3.90$, $(iii) = 3.31$, $(iv) = 3.47$, all given to 3 significant figures. This shows that, as in section 4.1, the homogeneous fit is a much better fit than the expected inhomogeneous fit. This is therefore not changed by the inclusion of a large magnetic field.

Almost all the data points lie within their uncertainty on the homogeneous fit, except for the 5th and 6th lowest intensity measurements which are multiple standard deviations away from the fit. The 5th lowest intensity measurement is more than 2 error bars below each of the fitted values, while the 6th lowest intensity measurement is between more than 2 error bars above each fitted value. None of the individual measurements used to calculate the Absorption Coefficient values were outliers to the other measurements. These are the only data points which are significantly displaced from the homogeneous fit shown by the dashed lanes.

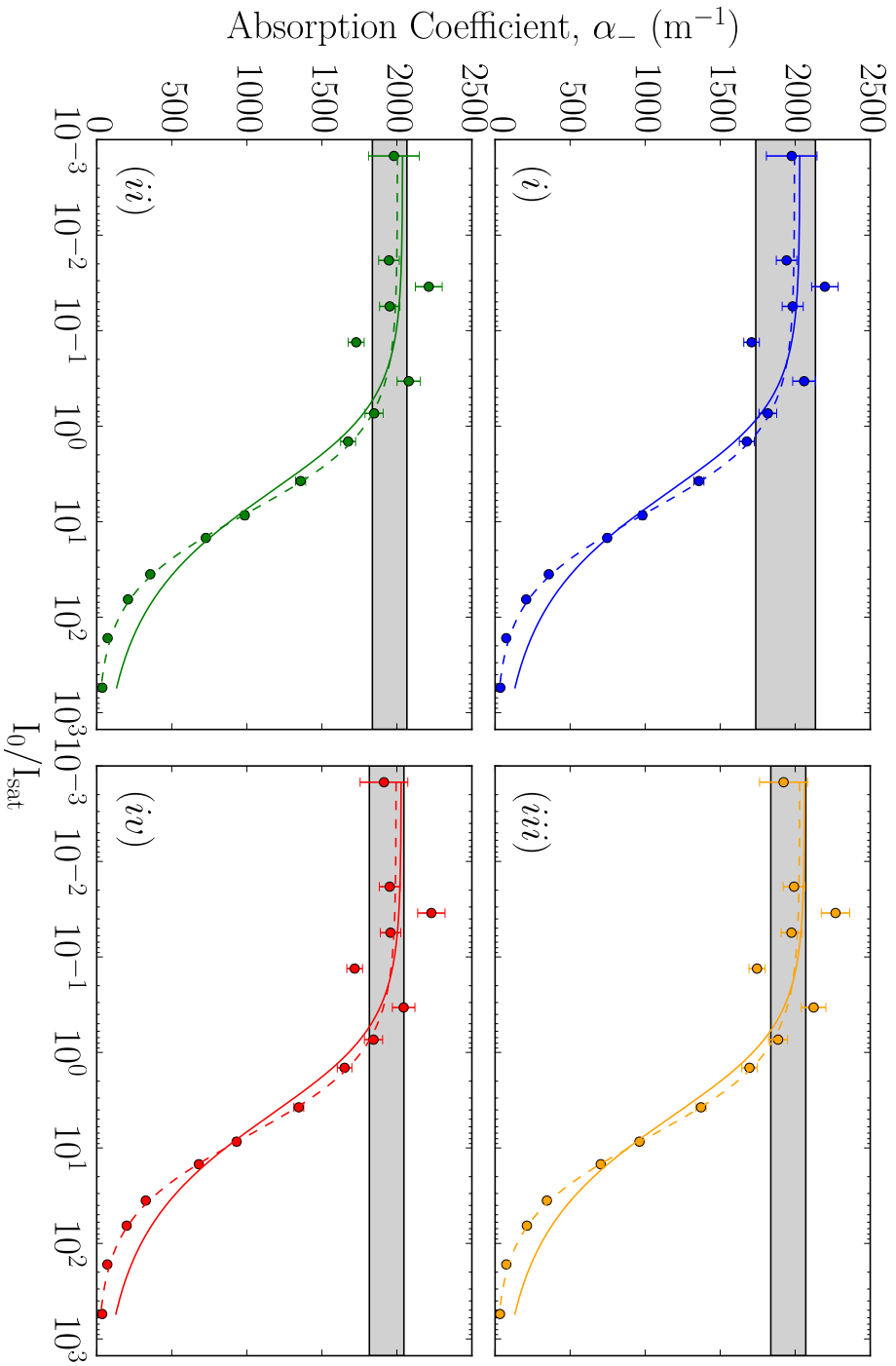

Figure 4.6: The absorption coefficients α corresponding to the peaks shown in figure 4.5. The inhomogeneous fit is shown for each as a solid curve, and the homogeneous as a dashed line. The upper and lower bounds of the theoretical α value is shown by the black solid lines, with the area between them shaded grey. This was calculated using the 5 measurements of the smallest intensity spectrum and fitting with ElecSus. T = 93.3 ±0.3 °C, additional broadening = 100 ±15 MHz and 41.6 ± 0.4 % of the light is polarised to pump σ^- transitions.

Power Evolution of the '-40 GHz' peaks

This experiment was repeated for the set of σ^- peaks that occur in the '-40 GHz' region. The peaks in this set refer to the $m_J = +1/2 \rightarrow m'_J = -1/2$, $\Delta m_I = 0$ strong σ^- transitions. The selection rules mean that the possible decays are via stimulated emission back to the original $m_J = +1/2$ state, or via spontaneous emission back to either the original $m_J = +1/2$ state, or the off resonant, and therefore dark, $m_J = -1/2$ state.

As these transitions are all open rather than closed like the '-20 GHz' set of peaks, they will be affected by optical pumping. This would be expected to decrease the power required to reach the weak-probe regime. Each peak represents only one $\sigma-$ transition for ^{87}Rb. There is also 1 % ^{85}Rb in the cell, the middle 2 peaks will include a very small additional absorption from those transitions, which occur within their Doppler broadening. This is why the middle two peaks are a very small amount larger than the outside two, but not enough to have a significant effect for this section. Although these transitions are open, their power evolution of these peaks may not necessarily be similar to that of the peaks with no external magnetic field applied. This is because the peaks investigated in this section are made up of only one ^{87}Rb transition each, separated in frequency by more than their Doppler broadening by the magnetic field, whereas at no magnetic field each peak was a composite of 3 transitions, of which far more than 1 dark state was possible due to the degeneracy of the energy sub-levels.

Figure 4.7 shows 1 transmission spectra for each laser beam intensities ranging from 35 ± 1 μW/cm^2 to 8.1 ± 0.2 W/cm^2. As previously, reducing the intensity of the laser beam increases the absorption of the laser beam by the Rubidium vapour. This is shown graphically by the change in line colour from a dark purple to green and then to a dark yellow colour. The theoretical spectrum, fitted with ElecSus using the lowest intensity spectrum, is shown as a dashed red line. 15 different intensities were used, and 5 transmission spectra were measured at each intensity. However, only ≈ 7 of the spectra are observable from the graph, due again to the fact that the lowest intensity spectra have such low SNR. The temperature of the atoms during this experiment was fitted using ElecSus to be 123.0 ± 0.5 °C, the additional

broadening to be 100 ± 10 MHz, and 44.5 ± 1.0 % light polarised to pump σ^- transitions. The temperature was increased from the ≈ 90 °C used for the '20 GHz' transitions in order to have as large an absorption as possible, without reaching the maximum possible absorption.

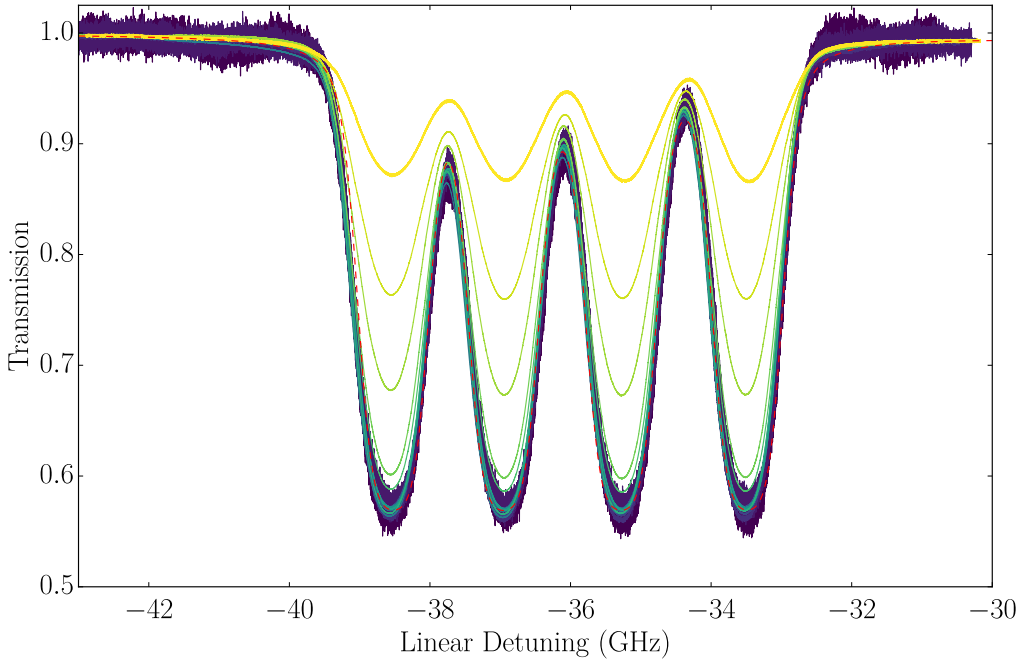

Figure 4.7: Experimental transmission spectra through the experimental cell with an external magnetic field $B = 1.54$ T applied, for the '−40 GHz' set of σ^- peaks, showing the transmission evolution of changing laser beam intensity against linear detuning. 1 of 5 measured spectra for each laser intensity is plotted. As the beam becomes more intense, less absorption takes place shown by the colour change from dark purple through green to a dark yellow. The theoretical spectrum is shown as the red dashed line, and has been fitted to the 4th smallest intensity spectrum using ElecSus, with variables of T = 123.5 °C, additional broadening of 90 MHz and a laser polarisation of 44 % pumping σ^- transitions.

Figure 4.8 shows the line-centre absorption coefficient of each peak against I_0/I_{sat}, where I_{sat} is again assumed to be equal to 1.67 mW/cm^2, the value for a two-level closed transition. It should be noted that the transitions considered here are in fact open and have 1 possible off-resonance dark state each. This means that the $x-$axis values are not necessarily correct. Therefore, although in these graphs the absorption coefficients appear to remain in the

weak-probe regime until approximately $I_0/I_{sat} = 10^0$, this is not necessarily accurate.

The labels on the graphs refer to the transitions as follows: (v) is the $m_I = +3/2$ transition and is the furthest negatively detuned peak shown in figure 4.7; (vi) is the $m_I = +1/2$ transition and is the 2nd peak most negatively detuned; (vii) is the $m_I = -1/2$ transition and is the 3rd most negatively detuned peak; and finally $(viii)$ is the $m_I = -3/2$ transition and is the 4th and least negatively detuned peak. The predicted values for the absorption coefficient of each peak is shown by the grey area, bounded by black lines. This was calculated using ElecSus for the 3rd lowest intensity spectrum.

The values of absorption coefficient were calculated in the same way as for the '−20 GHz' set of peaks, and the homogeneous and inhomogeneous equations, given by equations 4.4 and 4.3 respectively, were fitted to the data. In figure 4.8, the homogeneous fit is shown as the dashed curve, while the inhomogeneous fit is shown as the solid curve. As shown previously, the homogeneous curve is a better fit to the data. This is quantified by the χ^2_{red} values, which are as follows: (v) is 2.83 and 49.2, (vi) is 2.85 and 48.8, (vii) is 2.84 and 47.4, and finally $(viii)$ is 3.16 and 45.8, for the homogeneous and inhomogeneous fits respectively. This means that the fits are 17.4 ×, 17.1 ×, 16.7 × and 14.5 × better for each transition respectively from (v) to $(viii)$. While the inhomogeneous fit is still a much worse fit than the homogeneous fit for $(viii)$, the χ^2 analysis shows that the difference is reduced in comparison to the other 3 transitions.

While these values show that the homogeneous curve fits the data much better than the inhomogeneous curves, the difference in the values is considerably less than for the '−20 GHz' set of peaks. The values here show that the the homogeneous fits are approximately 16 × better than the inhomogeneous fits, whereas for the previous section they were between 29 and 39 × better. This could be because the '−40 GHz' transitions are open rather than closed and therefore hyperfine pumping can take place or, because of the temperature increase, atoms are more likely to be within the beam's width so hyperfine pumping is more likely to occur.

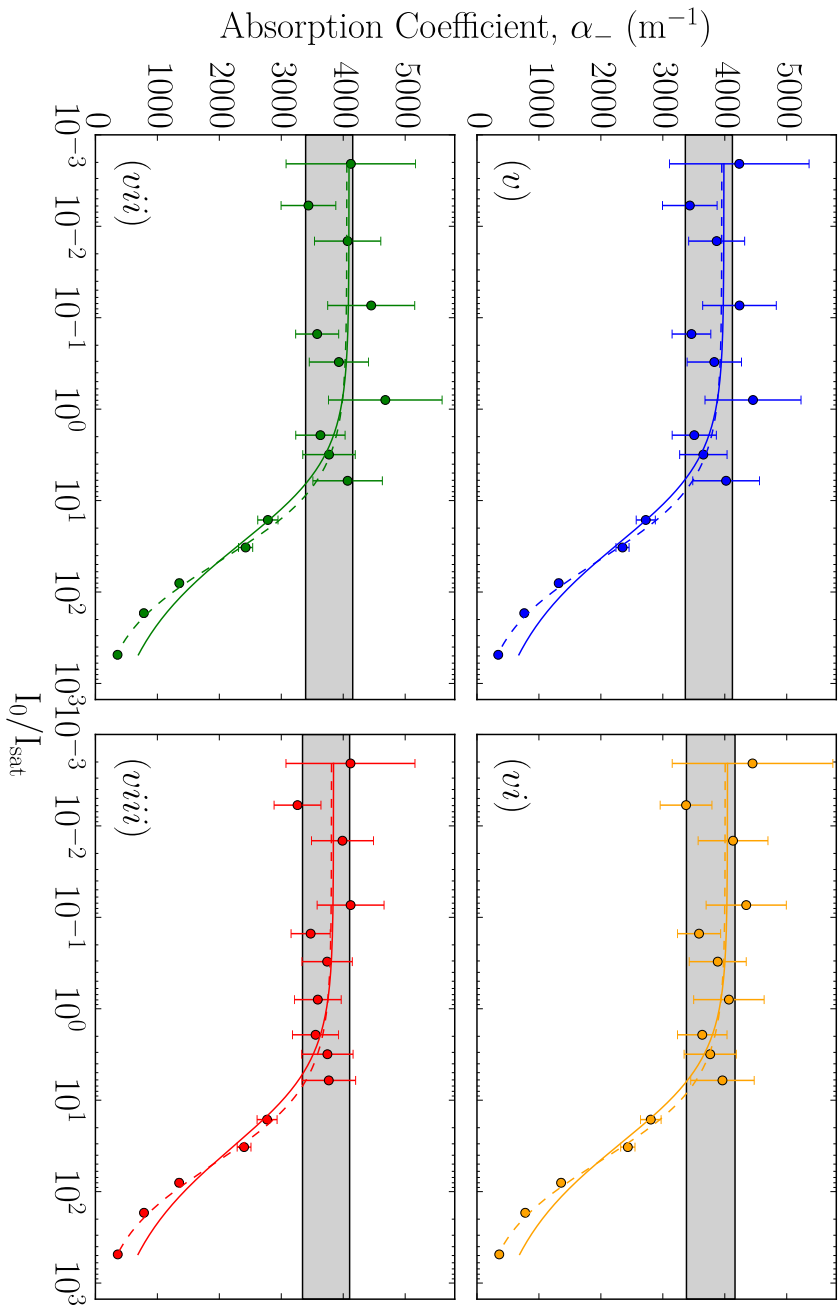

Figure 4.8: The absorption coefficients α corresponding to the peaks shown in figure 4.7. The inhomogeneous fit is shown for each as a solid curve, and the homogeneous as a dashed line. The upper and lower bounds of the theoretical α value is shown by the black solid lines, with the area between them shaded grey, calculated using the fitting function from ElecSus using the 5 measurements of the 3rd smallest intensity spectrum.

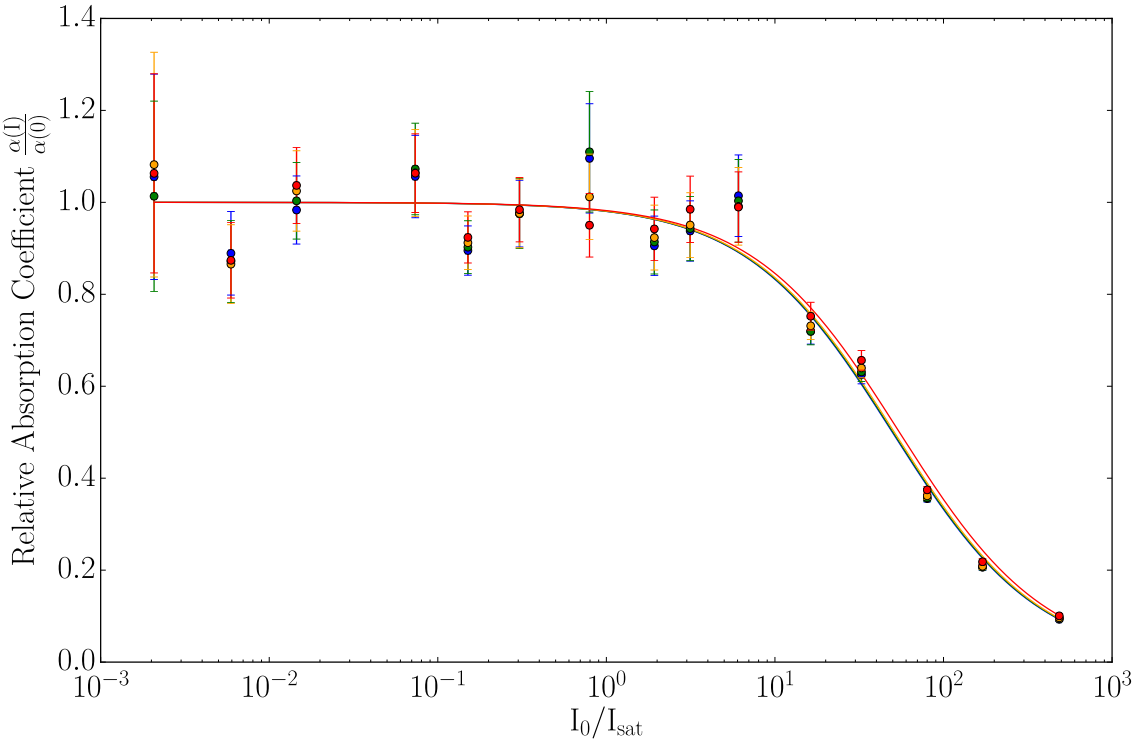

Figure 4.9: The normalised absorption coefficients $\alpha(I)/\alpha(0)$ corresponding to the peaks shown in figure 4.7. The homogeneous fits are shown as a solid line in the colours matching figure 4.8.

The differences between these power evolution of the 4 transitions can also be observed in the combined figure 4.9, where all four normalised absorption coefficients have been plotted on one graph. The homogeneous fit from figure 4.8 for each transition is plotted in the relevant colours. The gradient of (*viii*) (red), above values of $I_0/I_{sat} = 0$, is less steep than the 3 others. The 3 other gradients are indistinguishable from one another in this graph.

Power Evolution Comparison

In order to compare the power evolution of the absorption coefficients of these different transitions, the corresponding homogeneous fits for each transition have been plotted together on figure 4.10. They have been normalised by dividing each point by each corresponding absorption coefficient value at $I_0/I_{sat} = 0$. The data from figure 4.4 is shown as the dashed black line and

solid green line for the $F = 2 \rightarrow F' = 3, 2, 1$ and $F = 1 \rightarrow F' = 2, 1, 0$ transitions respectively. The four dotted red curves refer to the data in figure 4.6 at approximately '-20 GHz', while the four solid blue curves refer to the data shown in figure 4.6 which occurs at approximately '-40 GHz'.

It is important to note that the only peaks for which the used value of $I_{sat} = 1.67$ mW/cm^2 is actually accurate is the '-20 GHz' data, as these are the only closed transitions. The power evolution of the 4 '-20 GHz' peaks appear to be similar to one another, while the evolution of the 4 '-40 GHz' peaks have 3 similar curves and one with a less steep gradient, as is also shown in figure 4.9. In comparison, however, the sets of peaks appear to evolve with power at a very different rate. Too much should not be made of this difference, due to the assumption of the value of I_{sat}, and the different temperatures of the measurements .

However, some observations about the curves shown in figure 4.10 can still be made. The composite peaks of mostly open transitions at no magnetic field mean that more hyperfine pumping can take place than for a single closed transition. However, not all of the transitions that make up the composite peaks are closed. For the $F = 2 \rightarrow F' = 3, 2, 1$ composite peak, the $F = 2, m_F = +2 \rightarrow F' = 3, m'_F = +3$ σ^+ transition is closed, as well as the $F = 2, m_F = -2 \rightarrow F' = 3, m'_F = -3$ σ^- transition, while the other 34 possible $\sigma^{\pm}$, π transitions are open, and for the $F = 1 \rightarrow F' = 2, 1, 0$ composite peak all the 18 $\sigma^{\pm}$, π transitions are open.

The figure appears to show that the $F = 1 \rightarrow F' = 2, 1, 0$ peak requires a smaller I_0/I_{sat} value than the $F = 2 \rightarrow F' = 3, 2, 1$ peak to reach the weak-probe regime. Furthermore, the former peak follows a very similar curve to the 4 '-20 GHz' transitions, which are all closed. The reason for this is unclear. None of the transitions in the non-magnetic field peak are closed, but there are fewer transitions in this composite peak than for the $F = 2 \rightarrow F' = 3, 2, 1$ composite peak. This could help explain why the similarity to power evolution of the closed '-20 GHz', but a complete explanation is well beyond the scope of this experimental thesis.

In order to compare the effect of the magnetic field on the limits of the weak-probe regime, more work is clearly required to provide a theory for the value

of I_{sat} for the open transitions. There are two conclusions that can currently be made unambiguously: the narrow beam has a large influence on the limits of the weak-probe regime, such that it can be reached at higher intensities than previously thought; and that for this narrow beam, the homogeneous fit appears to be a much more accurate fit to the power evolution of the vapour than the previously used inhomogeneous fit, at both no magnetic field and in the hyperfine Paschen-Back regime. The relation between these two conclusions is at this point unclear, as in previous investigations the upper limits of the I_0/I_{sat} values did not surpass $\approx 10^1$, as the power evolution at high intensities was not of interest.

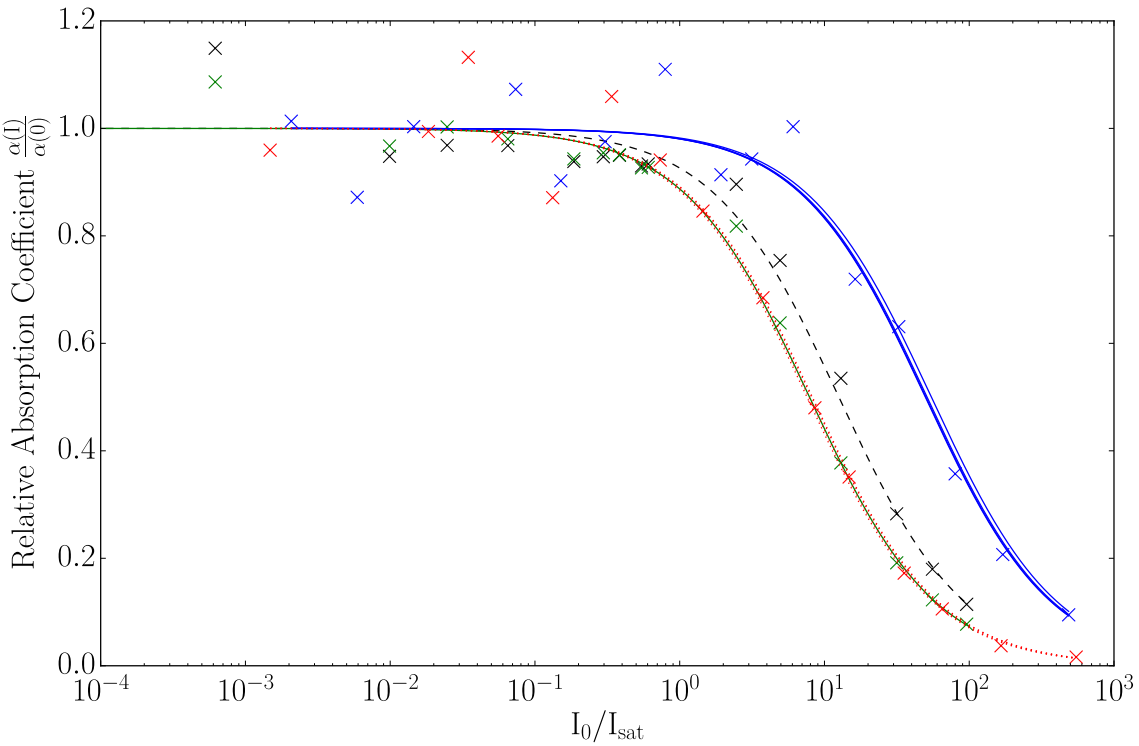

Figure 4.10: Homogeneous fits to the relative line-centre absorption coefficient $\alpha(I)/\alpha(0)$ plotted against I_0/I_{sat} for the two peaks in no magnetic field from figure 4.4 (dashed black line and solid green line for $F = 1 \rightarrow F'$, $F = 2 \rightarrow F'$ respectively), the 4 '−20 GHz' peaks from figure 4.6 (dotted red lines), and 4 '−40 GHz' peaks from figure 4.8 (solid blue lines).

Chapter 5

Conclusion

In this chapter, the overall conclusions that can be taken from the results of this investigation will be discussed. In section 5.2, possibilities of further work in this area is discussed.

5.1 Results

Temperature Evolution

An investigation into the temperature evolution of transmission and absorption coefficient spectra Rubidium atoms in the hyperfine Paschen-Back regime was successfully undertaken for a continuous laser detuning of approximately 150 GHz. The forms of both the S_0 and S_1 showed excellent agreement with the theory from ElecSus at temperatures ranging from 56 °C to 160 °C. Furthermore, the S_0 parameter was shown to have excellent agreement with ElecSus for narrow-band plots of up to 20 GHz.

The absorption coefficient ratio of two sets of strong transition peaks, expected to be equal to 3.00, was measured to be within their uncertainty of this value when a possible temperature fluctuation of < 1 K was taken into account.

Both the strong and weak transitions were measured and compared to the theory from ElecSus. It was found that ElecSus successfully predicts the behaviour of ^{87}Rb atoms in a magnetic field large enough that the atoms are

in the hyperfine Paschen-Back regime. Additionally, some areas of potential improvement or expansion of the ElecSus program were identified, so that a non-parallel angle between the laser beam's $\underline{\mathbf{k}}$ and the magnetic field $\underline{\mathbf{B}}$ could be considered. If the angle is small, then at lower temperatures the magnitude of the strong π transitions that coincide in frequency with the smaller detuned weak $\sigma^{\pm}$ transitions would not significantly perturb the transmission, in the same way that the weak $\sigma^{\pm}$ transitions do not absorb significant amounts of light at low temperatures. It is unclear the effect that a cell with a longer length would have. However, the existence of the strong π transitions can be exploited to ensure that the angle between $\underline{\mathbf{k}}$ and $\underline{\mathbf{B}}$ is perpendicular, as there are 4 strong π transitions and only 3 weak $\sigma^{\pm}$ transitions at those frequencies.

Power Evolution

The power evolution of the D2 line of Rubidium was investigated. The experimental cell, made up of 99% ^{87}Rb and 1% ^{85}Rb along with some buffer gases, had a length of 1 mm and due to the casing, a width of < 1 mm. This meant that a much narrower beam than previously investigated was required. While the atoms were not under the influence of an external magnetic field, the power evolution was found to not follow the inhomogeneous equation assumed in previous literature. This change is likely due to the beam width. Furthermore, the normalised power evolution of the two Doppler-Broadened ^{87}Rb transitions also followed different shapes: the $F = 2 \rightarrow F'$ transitions' power evolution was less steep than the $F = 1 \rightarrow F'$ transitions'. As these Doppler-Broadened peaks were each made up of 3 individual transitions, it follows that the normalised power evolution of the 2 combined peaks are not identical.

Once a magnetic field of 1.54 T was applied, the strong σ^{-} transitions that occurred at approximately -20 GHz and -40 GHz were investigated. The temperatures were chosen to maximise the transmission of each set of transitions. The normalised power evolution of the 4 peaks that occur at around -20 GHz were found to have a much shallower shape than that of the 4 peaks that occur at around -40 GHz. This could be due to whether the transitions

are open or closed. It is also possible that assuming $I_{sat} = 1.67$ mW/cm^2 for all the transitions is not correct as this assumes that all the transitions are closed, 2−level transitions with no optical pumping.

The Weak Probe regime was found to be reached at a much higher value of I/I_{sat} than previously understood: up to 2 orders of magnitude higher than the 10^{-3} previously considered to be the minimum required. This provides possibilities for applications such that the SNR can be increased when measuring transmission or absorption coefficients. This seemed to be mostly provided by the use of a narrow beam. It is unclear whether the use of a magnetic field significantly changes the intensity required to reach the Weak Probe regime. This should be investigated using a wider beam, with a different experimental cell.

5.2 Outlook

The Boltzmann factor defines the ratio [87] of a Boltzmann Distribution of two separate states, and therefore is given by:

$$p_i = e^{-\Delta E_{i,j}/k_B T}, \tag{5.1}$$

where $\Delta E_{i,j}$ refers to the difference between the states i and the j.

Using this equation, it may be possible to define the Boltzmann constant by using spectroscopy to measure p_i, and therefore k_B. If the temperature, the difference in energy level of two states and probability of being in that state are measured experimentally, the Boltzmann constant could be calculated. However, this relationship also means that $\Delta E_{i,j}$ needs to be sufficiently large that different p_i for energy states are detectable.

When taking into account the signal-to-noise ratio (SNR) that the value of k_B could be measured, it is clear that in order to measure the same or better precision as previous work has managed [88, 89], larger magnetic fields are required. The magnetic field applied in this work was $B = 1.54$ T, which corresponds to Boltzmann factors of 0.9942 and 1.0000, equal to a change of 0.0058, or 0.58%.

In order to measure k_B precisely, a much stronger magnetic field is required.

Eventually, this project hopes to use magnetic fields of up to $B = 8$ T, which would enable a Boltzmann factor difference between the highest and lowest ground states of 3.31%.

As Rubidium spectroscopy at such a high magnetic field has not previously been undertaken, it is important to understand the hyperfine Paschen-Back regime before increasing the magnetic field to such a high value. This work has made progress towards understanding the hyperfine Paschen-Back regime, as well as providing insight into the effectiveness and accuracy of ElecSus in the hyperfine Paschen-Back regime, identifying ways in which it could be improved before further experimentation is instigated.

Appendix A

Error Analysis

Normalised residuals $\mathrm{r_n}$ are found by [77]

$$\mathrm{r_{n,}}_i = \frac{y_{\mathrm{e},i} - y_{\mathrm{t},i}}{\alpha_i}, \tag{A.1}$$

where $y_{\mathrm{e,i}}$ is the individual experimental value, $y_{\mathrm{t,i}}$ is the individual theoretical value and α_i is the corresponding individual uncertainty of the experiment value. The reduced χ^2 value is given by

$$\chi^2_{\mathrm{red}} = \frac{\sum_i \mathrm{r}^2_{\mathrm{n},i}}{\nu}, \tag{A.2}$$

where ν is the number of degrees of freedom for a function that has $\mathcal{N}$ variable parameters using N independent data points where:

$$\nu = N - \mathcal{N}. \tag{A.3}$$

The Root Mean Square error (RMS) is given by [90]

$$\mathrm{RMS} = \sqrt{\frac{1}{N^2}\sum_{\mathrm{i}} (y_{\mathrm{e,i}} - y_{\mathrm{t,i}})^2}. \tag{A.4}$$

The weighted mean μ is calculated by [77]

$$\mu = \frac{\sum_i y_i w_i}{\sum_i w_i}, \tag{A.5}$$

where y_i is one measurement and $w_i = 1/\alpha_i^2$ is the corresponding weighting, and the error of the weighted mean is equal to

$$\alpha_\mu = \sqrt{\frac{1}{\sum_i w_i}} \tag{A.6}$$

Appendix B

Sub-Doppler Spectroscopy

The 'Sub-Doppler' technique was used to convert the data from an arbitrary linear axis into a frequency axis in Hz. Shown in figure 3.1 as a labelled grey box, it is a nonlinear Spectroscopy technique which is used to measure transitions usually hidden within the Doppler-broadening of the Voigt profile.

It is a well established technique and as such the theory behind it will not be discussed in this thesis. Thorough explanations of Sub-Doppler Spectroscopy for the D2 line of Rubidium can be found in [60], while a more general discussion is given in textbooks such as [91].

A 75 mm reference cell of both ^{85}Rb and ^{87}Rb in their natural abundances was used to perform Sub-Doppler spectroscopy, and room temperature was sufficient to measure a significant absorption with a good SNR. The position of the hyperfine peaks were fit to a linear equation that compared them to the theoretical peak frequencies. This equation was then used to convert the entire x-axis into a linear frequency axis with units of Hz.

This is a well documented technique for converting into a frequency axis. The hyperfine transitions of the D2 line for both ^{85}Rb and ^{87}Rb all take place within 7 GHz of each other in the absence of a magnetic field. Extrapolating the fit across frequencies ranges up the 160 GHz range required at a magnetic field of $B = 1.54$ T has not been well studied. Part of the aim of this thesis is to evaluate whether this technique is reliable enough to use for even higher magnetic fields.

An example of a spectrum measured using this technique is shown in blue in

figure B.1. The green lines show the position of the peaks that were used to compare to their theoretical counterparts.

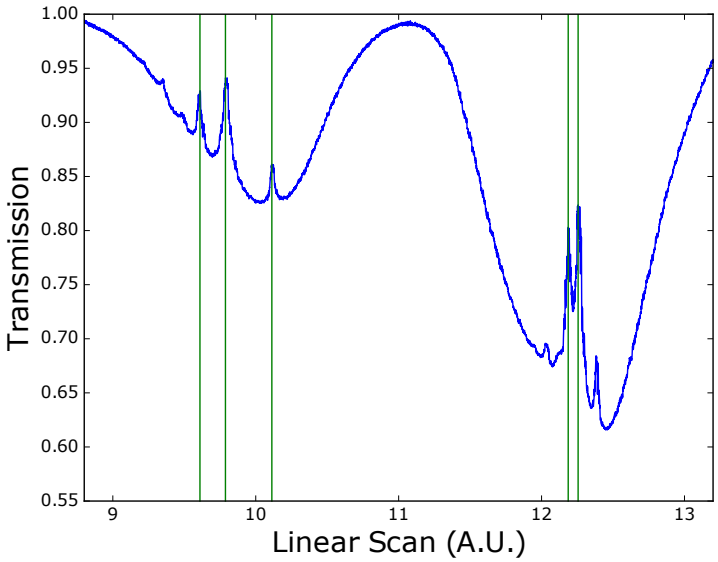

Figure B.1: An example spectrum using the Sub-Doppler technique in blue, showing the negatively detuned group of 3 hyperfine transitions and their crossover resonances from ^{87}Rb atoms on the left, and the corresponding group for ^{85}Rb atoms on the right, over the linear, arbitrary axis attained using the cavity. In green is shown the positions of the specific peaks used for x-axis calibration.

Appendix C

Cell Imaging

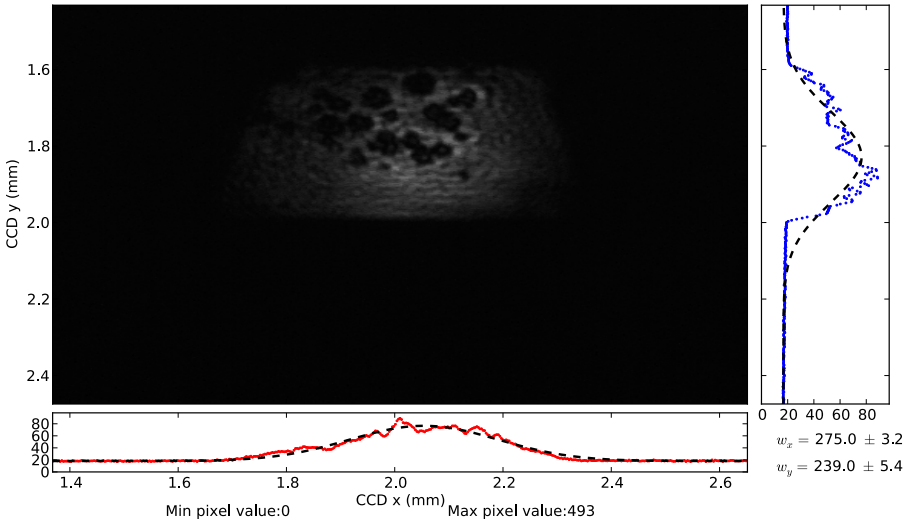

Figure C.1: Screenshot of beam profiler software including image and pixel values on x, y axes showing sharp edges of cell as the beam was too wide. Dark patches inside the cell show where rubidium has condensed on the glass surface of the cell. The y axis shows how the beam was cut off by the edges of the cell, with a sharp gradient at approximately 1.8 to 2.0 mm on the y axis. The dashed lines show a fitted normal distribution to the CCD data.

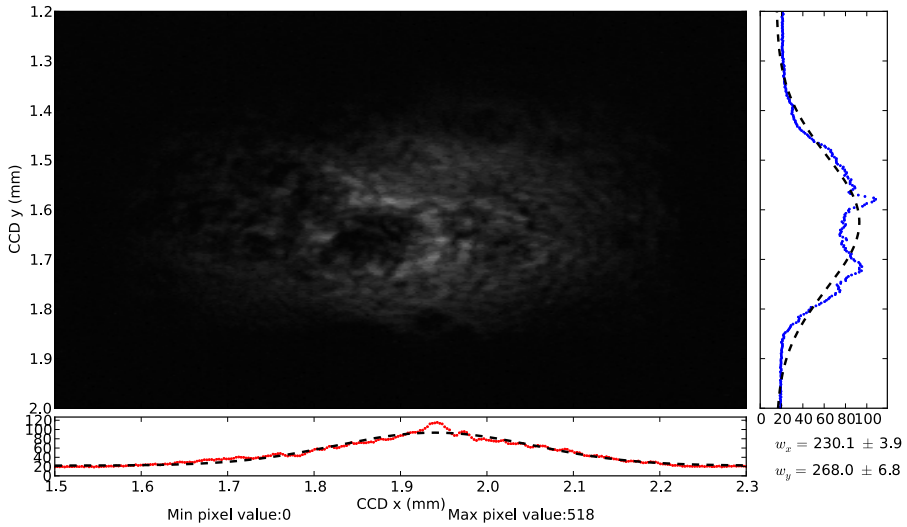

Figure C.2: Screenshot of beam profiler software including the image and pixel values on x, y axes showing the beam width measurements through the cell. The dark patches inside the cell show solid rubidium where it has condensed on the glass surface of the cell. The dashed lines show a fitted normal distribution to the data from the CCD.

Bibliography

[1] T. W. Odom, R. M. Dickson, M. A. Duncan, and W. Tan, *Shining a Light on the Molecular and Nanoscopic Worlds*, ACS Photonics **2**, 787 (2015), 10.1021/acsphotonics.5b00337. 1

[2] E. Bequerel, *Recherches sur les effets de la radiation chimique de la lumière solaire, au moyen des courants électriques.*, C.R. Acad. Sci. **9**, 145 (1839). 1

[3] Nobelprize.org, *The 2014 Nobel Prize in Physics - Press Release*, 2014. 1

[4] W. D. Phillips, *Nobel Lecture: Laser cooling and trapping of neutral atoms*, Rev. Mod. Phys. **70**, 721 (1998), 10.1103/RevModPhys.70.721. 1, 3

[5] Dietrich Marcuse, *Theory of Dielectric Optical Waveguides*, 2nd ed. (Academic Press, San Diego, 1991). 1

[6] A. D. Ludlow, M. M. Boyd, J. Ye, E. Peik, and P. O. Schmidt, *Optical atomic clocks*, Reviews of Modern Physics **87**, 637 (2015), 10.1103/RevModPhys.87.637. 1

[7] P. S. Jessen, I. H. Deutsch, and R. Stock, *Quantum Information Processing with Trapped Neutral Atoms*, Quantum Information Processing **3**, 91 (2004), 10.1007/s11128-004-9418-2. 1, 2, 3

[8] R. P. Feynman, *Simulating Physics with Computers*, International Journal of Theoretical Physics **217** (1982). 2

[9] M. Nakahara and T. Ohmi, *Quantum computing : from linear algebra to physical realizations* (CRC Press, 2008). 2

[10] G. K. Brennen, C. M. Caves, P. S. Jessen, and I. H. Deutsch, *Quantum Logic Gates in Optical Lattices*, **82**, 363 (1999). 2

[11] T. W. Haensch and A. L. Schawlow, *COOLING OF GASES BY LASER RADIATION*, Optics Communications **13** (1975). 3

[12] S. Chu, *Nobel Lecture: The manipulation of neutral particles*, Rev. Mod. Phys. **70**, 685 (1998), 10.1103/RevModPhys.70.685. 3

[13] C. N. Cohen-Tannoudji, *Nobel Lecture: Manipulating atoms with photons*, Reviews of Modern Physics **70**, 707 (1998), 10.1103/RevModPhys.70.707. 3

[14] S. Chu, L. Hollberg, J. E. Bjorkholm, A. Cable, and A. Ashkin, *Three-dimensional viscous confinement and cooling of atoms by resonance radiation pressure*, Physical Review Letters **55**, 48 (1985), 10.1103/PhysRevLett.55.48. 3

[15] E. A. Cornell and C. E. Wieman, *BOSE-EINSTEIN CONDENSATION IN A DILUTE GAS; THE FIRST 70 YEARS AND SOME RECENT EXPERIMENTS* (Nobel Foundation, Stockholm, 2002). 3

[16] W. Ketterle, *WHEN ATOMS BEHAVE AS WAVES: BOSE-EINSTEIN CONDENSATION AND THE ATOM LASER* (Nobel Foundation, Stockholm, 2002). 3

[17] E. L. Raab, M. Prentiss, A. Cable, S. Chu, and D. E. Pritchard, *Trapping of Neutral Sodium Atoms with Radiation Pressure*, Physical Review Letters **59**, 2631 (1987), 10.1103/PhysRevLett.59.2631. 3

[18] K. J. Weatherill, *A CO2 Laser Lattice Experiment for Cold Atoms*, PhD thesis, Durham University, 2007. 3

[19] P. F. Griffin, *Laser Cooling and Loading of Rb into A Large Period, Quasi-Electrostatic, Optical Lattice*, PhD thesis, Durham University, 2005. 3

[20] T. Baluktsian *et al.*, *Fabrication method for microscopic vapor cells for alkali atoms*, Optics Letters **35**, 1950 (2010), 10.1364/OL.35.001950. 3

[21] C. B. Alcock, V. P. Itkin, and M. K. Horrigan, *Vapor Pressure Equations for the Metallic Elements: 298-2500 K*, Can. Metall. Quart. **23**, 309 (1984). 4

[22] P. ZEEMAN, *The Effect of Magnetisation on the Nature of Light Emitted by a Substance*, Nature **55**, 347 (1897), 10.1038/055347a0. 4

[23] L. Weller *et al.*, *Absolute absorption and dispersion of a rubidium vapour in the hyperfine PaschenBack regime*, Journal of Physics B: Atomic, Molecular and Optical Physics **45**, 215005 (2012), 1208.1879, 10.1088/0953-4075/45/21/215005. 5, 17

[24] L. Weller *et al.*, *An optical isolator using an atomic vapor in the hyperfine Paschen-Back regime*, Optics letters **37**, 3405 (2012), arXiv:1206.0214v1. 5

[25] D. J. Whiting, J. Keaveney, C. S. Adams, and I. G. Hughes, *Direct measurement of excited-state dipole matrix elements using electromagnetically induced transparency in the hyperfine Paschen-Back regime*, Physical Review A **93**, 043854 (2016), 10.1103/PhysRevA.93.043854. 5

[26] M. A. Zentile *et al.*, *ElecSus: A program to calculate the electric susceptibility of an atomic ensemble*, Computer Physics Communications **189**, 162 (2015), 10.1016/j.cpc.2014.11.023. 5

[27] M. A. Zentile, *Applications of the Faraday Effect in Hot Atomic Vapours*, PhD thesis, Durham University, 2015. 5, 43

[28] M. A. Zentile, D. J. Whiting, J. Keaveney, C. S. Adams, and I. G. Hughes, *Atomic Faraday filter with equivalent noise bandwidth less than 1 GHz*, Optics Letters **40**, 2000 (2015), 1502.07187, 10.1364/OL.40.002000. 5

[29] J. Keaveney, W. J. Hamlyn, C. S. Adams, and I. G. Hughes, *A single-mode external cavity diode laser using an intra-cavity atomic Faraday filter with short-term linewidth* < 400 *kHz and long-term stability of* < 1 *MHz*, Review of Scientific Instruments **87** (2016). 5

[30] D. J. Whiting *et al.*, *Electromagnetically induced absorption in a non-degenerate three-level ladder system*, Optics Letters **40**, 4289 (2015), 10.1364/OL.40.004289. 5

[31] R. Mirzoyan *et al.*, *EIT resonance features in strong magnetic fields in rubidium atomic columns with length varying by 4 orders*, Optics and Spectroscopy **120**, 864 (2016), 10.1134/S0030400X16060151. 5

[32] M. Widmann *et al.*, *Faraday Filtering on the Cs-D$_1$-Line for Quantum Hybrid Systems*, (2015), 1505.01719. 5

[33] A. Sargsyan *et al.*, *Complete hyperfine Paschen-Back regime at relatively small magnetic fields realized in potassium nano-cell*, EPL (Europhysics Letters) **110**, 23001 (2015), 10.1209/0295-5075/110/23001.

[34] A. Sargsyan, Y. Pashayan-Leroy, C. Leroy, and D. Sarkisyan, *Collapse and revival of a Dicke-type coherent narrowing in potassium vapor confined in a nanometric thin cell*, Journal of Physics B: Atomic, Molecular and Optical Physics **49**, 075001 (2016), 10.1088/0953-4075/49/7/075001. 5

[35] K. A. Whittaker *et al.*, *Spectroscopic detection of atom-surface interactions in an atomic-vapor layer with nanoscale thickness*, Physical Review A **92**, 052706 (2015), 10.1103/PhysRevA.92.052706. 5

[36] J. H. D. Munns *et al.*, *In situ characterization of an optically thick atom-filled cavity*, Physical Review A **93**, 013858 (2016), 10.1103/PhysRevA.93.013858. 5

[37] L. Windholz and M. Musso, *Zeeman- and Paschen-Back-effect of the hyperfine structure of the sodiumD 2-line*, Zeitschrift fuer Physik D Atoms, Molecules and Clusters **8**, 239 (1988), 10.1007/BF01436947. 6

[38] C. Umfer, L. Windholz, and M. Musso, *Investigations of the sodium and lithium D-lines in strong magnetic fields*, Zeitschrift fuer Physik D Atoms, Molecules and Clusters **25**, 23 (1992), 10.1007/BF01437516. 6

[39] B. E. Sherlock and I. G. Hughes, *How weak is a weak probe in laser spectroscopy?*, Am. J. Phys. **77**, 111 (2009), 10.1119/1.3013197. 6, 29, 30, 71, 72, 73

[40] C. J. Foot, *Atomic Physics* (Oxford University Press, 2005). 8, 10, 11, 12

[41] N. Bohr, *I. On the constitution of atoms and molecules*, Philosophical Magazine Series 6 **26**, 1 (1913), 10.1080/14786441308634955. 8

[42] D. J. Griffiths, *Introduction to Quantum Mechanics* (Prentice Hall, Inc, 1994). 9

[43] S. Blundell, *Magnetism in Condensed Matter* (Oxford University Press, 2001). 9

[44] P. J. Mohr, B. N. Taylor, and D. B. Newell, *CODATA recommended values of the fundamental physical constants: 2010*, Rev. Mod. Phys. **84**, 1527 (2012). 10

[45] E. Arimondo, M. Inguscio, and P. Violino, *Experimental determinations of the hyperfine structure in the alkali atoms*, Rev. Mod. Phys. **49**, 31 (1977). 10

[46] L. Weller, *Absolute Absorption and Dispersion in a Thermal Rb Vapour at High Densities and High Magnetic Fields*, PhD thesis, Durham University, 2013. 10, 16, 32, 37, 40

[47] J. S. Rigden, *Hydrogen : the essential element* (Harvard University Press, 2002). 11

[48] B. H. Bransden and C. J. Joachain, *Quantum Mechanics*, Second edi ed. (Pearson Education Limited, 2000). 11

[49] A. Corney, *Atomic and Laser Spectroscopy* (Clardendon Press, 1978). 13, 30

[50] G. K. Woodgate, *Elementary Atomic Structure* (Oxford University Press, Oxford, 1983). 13

[51] D. J. Berkeland and M. G. Boshier, *Destabilization of dark states and optical spectroscopy in Zeeman-degenerate atomic systems*, Phys. Rev. A. **65** (2002). 21, 23

[52] E. Hecht, *Optics*, 4th ed. (Addison-Wesley, 2003). 23

[53] P. Siddons, C. S. Adams, C. Ge, and I. G. Hughes, *Absolute absorption on rubidium D lines: comparison between theory and experiment*, J. Phys. B: At. Mol. Opt. Phys. **41**, 155004 (2008), 10.1088/0953-4075/41/15/155004. 24, 50, 72

[54] R. Loudon, *The Quantum Theory of Light*, 3rd ed. (Oxford University Press, 2000). 24, 25

[55] A. Bohm, N. L. Harshman, and H. Walther, *Relating the Lorentzian and exponential: Fermi's approximation, the Fourier transform and causality*, Physical Review A **66** (2002), 10.1103/PhysRevA.66.012107. 25

[56] U. Volz and H. Schmoranzer, *Precision lifetime measurements on alkali atoms and on helium by beam-gas-laser spectroscopy*, Phys. Scr. **t65**, 48 (1996), 10.1088/0031-8949/1996/T65/007. 25, 75

[57] L. Weller, R. J. Bettles, P. Siddons, C. S. Adams, and I. G. Hughes, *Absolute absorption on the rubidium D1 line including resonant dipole-dipole interactions.*, Journal of Physics B: Atomic, Molecular and Optical Physics **44**, 195006 (2011), 1107.3092, 10.1088/0953-4075/44/19/195006. 25

[58] M. Bass and V. N. Mahajan, *Handbook of optics. Volume I, Geometrical and physical optics, polarized light, components and intruments*, 2nd ed. (McGraw-Hill, 1995). 25

[59] M. J. Pritchard, *Manipulation of ultracold atoms using magnetic and optical fields* , PhD thesis, Durham University, 2006. 26

[60] D. A. Smith and I. G. Hughes, *The role of hyperfine pumping in multilevel systems exhibiting saturated absorption*, Am. J. Phys. **72**, 631 (2004), 10.1119/1.1652039. 29, 99

[61] J. D. Jackson, *Classical Electrodynamics*, 3rd ed. (Wiley, 1999). 32

[62] D. Brink and G. Satchler, *Angular Momentum* (Oxford University Press, 1968). 34

[63] G. Hakhumyan, C. Leroy, R. Mirzoyan, Y. Pashayan-Leroy, and D. Sarkisyan, *Study of forbidden atomic transitions on D2 line using Rb nano-cell placed in external magnetic field*, The European Physical Journal D **66**, 119 (2012), 10.1140/epjd/e2012-20687-2. 37

[64] B. Schaefer, E. Collett, R. Smyth, D. Barrett, and B. Fraher, *Measuring the Stokes polarization parameters*, American Journal of Physics **75**, 163 (2007), 10.1119/1.2386162. 39

[65] W. Yuan, W. Shen, Y. Zhang, and X. Liu, *Dielectric multilayer beam splitter with differential phase shift on transmission and reflection for division-of-amplitude photopolarimeter*, Optics Express **22**, 11011 (2014), 10.1364/OE.22.011011. 39

[66] G. Casa *et al.*, *Primary Gas Thermometry by Means of Laser-Absorption Spectroscopy: Determination of the Boltzmann Constant*, Physical Review Letters **100**, 200801 (2008), 10.1103/PhysRevLett.100.200801. 39

[67] P. Siddons, C. S. Adams, and I. G. Hughes, *Off-resonance absorption and dispersion in vapours of hot alkali-metal atoms*, J. Phys. B: At. Mol. Opt. Phys. **42**, 175004 (2009), 10.1088/0953-4075/42/17/175004. 43, 71, 77

[68] S. L. Kemp, I. G. Hughes, and S. L. Cornish, *An analytical model of off-resonant Faraday rotation in hot alkali metal vapours*, Journal of Physics B: Atomic, Molecular and Optical Physics **44**, 235004 (2011), 10.1088/0953-4075/44/23/235004. 43

[69] A. Millett-Sikking, I. G. Hughes, P. Tierney, and S. L. Cornish, *DAVLL lineshapes in atomic rubidium*, Journal of Physics B: Atomic, Molecular and Optical Physics **40**, 187 (2007), 10.1088/0953-4075/40/1/017. 45

[70] M. L. Harris *et al.*, *Polarization spectroscopy in rubidium and cesium*, Phys. Rev. **73**, 062509 (2006), 10.1103/PhysRevA.73.062509. 43, 74

[71] M. Faraday, *Experimental Researches in Electricity. Nineteenth Series*, Philos. Trans. R. Soc. London **136**, 1 (1846), http://www.jstor.org/stable/108303. 43

[72] A. L. Marchant *et al.*, *Off-resonance laser frequency stabilization using the Faraday effect*, Optics Letters **36**, 64 (2011), 10.1364/OL.36.000064. 45, 59

[73] C. Lee *et al.*, *Small-sized dichroic atomic vapor laser lock*, Review of Scientific Instruments **82**, 043107 (2011), 10.1063/1.3568824. 45

[74] T. Acsente, *Laser Diode Intensity Noise Induced by Mode Hopping*, Romanian Reports in Physics **59**, 87 (2007). 49

[75] J. Biescheuvel *et al.*, *Widely tunable laser frequency offset lock with 30 GHz range and 5 THz offset*, OPTICS EXPRESS **21** (2013), 10.1364/OE.21.014008.

[76] T. A. Heumier, *Mode hopping in semiconductor lasers*, PhD thesis, Montana State University, 1992. 49

[77] Hughes, Ifan and Hase, Thomas, *Measurements and their Uncertainties: A Practical Guide to Modern Error Analysis*, 2nd ed. (Oxford University Press, Oxford, 2010). 55, 67, 98

[78] M. A. Zentile *et al.*, *The hyperfine PaschenBack Faraday effect*, Journal of Physics B: Atomic, Molecular and Optical Physics **47**, 075005 (2014). 59

[79] I. G. Hughes and D. P. Hampshire, Private Communication. 59

[80] D. Ciampini, R. Battesti, C. Rizzo, and E. Arimondo, *Optical spectroscopy of a microsized Rb vapor sample in magnetic fields up to 58 T*, Phys. Rev. A **96**, 052504 (2017). 59

[81] T. Lindvall and I. Tittonen, *Effect of optical pumping on alkali-atom Doppler-limited spectra*, J. Mod. Opt. **54**, 2779 (2007), 10.1080/09500340701243566. 73

[82] I. G. Hughes and R. M. Potvliege, Private Communication. 78

[83] M. R. Sprague *et al.*, *Efficient optical pumping and high optical depth in a hollow-core photonic-crystal fibre for a broadband quantum memory*, New Journal of Physics **15**, 055013 (2013). 78

[84] G. Epple *et al.*, *Rydberg atoms in hollow-core photonic crystal fibres*, Nature Communications **5** (2014).

[85] M. Sprague *et al.*, *Storage of Light in a Hollow-Core Photonic-Crystal Fibre*, in *CLEO: 2013*, p. QTu1C.4, Optical Society of America, 2013.

[86] T. Bradley, *Atomic vapours filled hollow core photonic crystal fibre for magneto-optical spectroscopy*, 2014. 78

[87] Tipler Paul A. and R. Llewellyn, *Modern Physics* (W. H. Freeman, 2003). 96

[88] M. de Podesta *et al.*, *Correction of NPL-2013 estimate of the Boltzmann constant for argon isotopic composition and thermal conductivity*, Metrologia **52**, S353 (2015), 10.1088/0026-1394/52/5/S353. 96

[89] G.-W. Truong, J. D. Anstie, E. F. May, T. M. Stace, and A. N. Luiten, *Accurate lineshape spectroscopy and the Boltzmann constant*, Nature Communications **6**, 8345 (2015), 10.1038/ncomms9345. 96

[90] T. Chai and R. R. Draxler, *Root mean square error (RMSE) or mean absolute error (MAE)? Arguments against avoiding RMSE in the literature*, Geoscientific Model Development **7**, 1247 (2014). 98

[91] M. D. Levenson and S. Kano, *Introduction to nonlinear laser spectroscopy* (Academic Press, 1988). 99